



저작자표시-비영리-변경금지 2.0 대한민국

이용자는 아래의 조건을 따르는 경우에 한하여 자유롭게

- 이 저작물을 복제, 배포, 전송, 전시, 공연 및 방송할 수 있습니다.

다음과 같은 조건을 따라야 합니다:



저작자표시. 귀하는 원저작자를 표시하여야 합니다.



비영리. 귀하는 이 저작물을 영리 목적으로 이용할 수 없습니다.



변경금지. 귀하는 이 저작물을 개작, 변형 또는 가공할 수 없습니다.

- 귀하는, 이 저작물의 재이용이나 배포의 경우, 이 저작물에 적용된 이용허락조건을 명확하게 나타내어야 합니다.
- 저작권자로부터 별도의 허가를 받으면 이러한 조건들은 적용되지 않습니다.

저작권법에 따른 이용자의 권리는 위의 내용에 의하여 영향을 받지 않습니다.

이것은 [이용허락규약\(Legal Code\)](#)을 이해하기 쉽게 요약한 것입니다.

[Disclaimer](#)

공학박사 학위논문

**Microstructure Modification and  
Mechanical Properties of Fe-based  
Alloys Prepared by Liquid Phase  
Sintering and Field Assisted Sintering**

액상 소결 및 통전 활성 소결 방법으로 제작한 철 계  
합금의 미세 구조 개선과 기계적 특성 평가

2021 년 8 월

서울대학교 대학원  
재료공학부  
유진수

# **Microstructure Modification and Mechanical Properties of Fe-based Alloys Prepared by Liquid Phase Sintering and Field Assisted Sintering**

지도 교수 홍 성 현

이 논문을 공학박사 학위논문으로 제출함  
2021년 8월

서울대학교 대학원  
재료공학부  
유진수

유진수의 공학박사 학위논문을 인준함  
2021년 4월

위원장 한홍남

부위원장 홍성현

위원 황농문

위원 장재일

위원 이혁모

## **Abstract**

# **Microstructure Modification and Mechanical Properties of Fe-based Alloys Prepared by Liquid Phase Sintering and Field Assisted Sintering**

JinSu You

Department of Materials Science and Engineering

College of Engineering

Seoul National University

Powder metallurgy (P/M) is metal consolidation technique for the manufacture of parts from raw starting powders by compaction and heating. P/M technique has been used in various industries and applications, because of its efficiency and net-shaped capability. However, the P/M applications are very limited due to the presence of porosity ranging from 5 to 15 vol. %. To solve this problem, several sintering techniques, such as liquid phase sintering, hot pressing and field assisted sintering have been extensively investigated. However, the improvement of mechanical properties was still limited, and thus microstructure modification is required to enhance the mechanical properties. In addition, the microstructural development and densification mechanism during sintering have not been fully explored.

In this thesis, the effects of sintering methods, sintering condition, composition and heat treatment on microstructure were intensively studied, and then the effect of microstructure modification on the mechanical properties of Fe-based alloys was thoroughly investigated. The mentioned above will be discussed in more detail on the three main topics. 1) Microstructure modification of liquid phase sintered Fe-Ni-B-C alloys for improved mechanical properties, 2) Effects of molybdenum addition on microstructure and mechanical properties of Fe-B-C sintered alloys, and 3) Effect of field assisted sintering on densification, microstructure and mechanical properties of Fe-Ni alloys.

First, Ni addition was employed to decrease the eutectic temperature and improve the densification and mechanical properties of Fe-B-C alloys. To solve the formation of continuous network of hard eutectics, the composition was controlled to achieve the system with the optimized hard phase fraction, and heat treatment was performed to induce the coarsening of solidified  $\alpha$ -Fe particles into the matrix. As a result of microstructure modification, the post annealed Fe-1Ni-0.4B-0.8C alloy resulted in the high elongation to failure of 5.2 %.

Second, molybdenum (Mo) was introduced in Fe-B-C alloy system to modify the grain boundary microstructure through the formation of two Fe-Mo-B and Fe-B-C solidified phases. For this, Fe-xMo-0.4B-0.8C ( $x=1.0\sim 5.0$  in wt%) alloys were prepared by LPS and their microstructure and mechanical properties were investigated. With Mo addition, the matrix grain changed from pearlite and re-precipitated ferrite to pearlite (or pearlite/bainite) and the grain boundary changed from a continuous network to a lamella structure composed of MoFe(C,B) (WCoB-

type boride) and  $(\text{Fe,Mo})_3(\text{C,B})$  ( $\text{Fe}_3\text{C}$ -type carbide). As a result of microstructure modification, the mechanical properties such as hardness, tensile strength, and elongation to failure were significantly improved. In particular, Fe-5Mo-0.4B-0.8C alloy exhibited a high tensile strength of 674 MPa and a high elongation to failure of 4.92%.

Third, Fe-xNi alloys ( $x=0\sim 5.0$  in wt%) were consolidated by conventional sintering (CS), field assisted sintering (FAS), and hot pressing (HP) methods, and their densification, microstructure, mechanical properties were comparatively investigated, particularly focusing on the field or current effects of FAS technique. The Ni addition promoted the densification and suppressed the grain growth in Fe-Ni alloys consolidated by both CS and FAS, and the FAS produced the Fe-Ni alloys with higher apparent density and smaller grain size. Consequently, the Fe-Ni alloys fabricated by FAS exhibited a significant improvement in the bulk hardness compared to those consolidated by CS and HP. The obtained results indicated that the electric current together with mechanical pressure in FAS promoted the Ni diffusion along the grain boundaries, which resulted in the enhanced densification with suppressed grain growth.

**Keywords : Liquid phase sintering, Field assisted sintering, Microstructure, Grain boundary, Modification, Mechanical properties**

*Student Number* : 2014-31057

# Table of Contents

<b>Abstract .....</b>	<b>i</b>
<b>Table of Contents.....</b>	<b>iv</b>
<b>List of Figures .....</b>	<b>vi</b>
<b>List of Abbreviations.....</b>	<b>xiv</b>
<b>Chapter 1.</b>	
<b>General background.....</b>	<b>1</b>
<b>1.1. Powder metallurgy .....</b>	<b>1</b>
<b>1.2. Liquid phase sintering.....</b>	<b>5</b>
<b>1.3. Field assisted sintering .....</b>	<b>11</b>
<b>Chapter 2.</b>	
<b>Microstructure modification of liquid phase sintered Fe-Ni-B-C alloys for high mechanical properties .....</b>	<b>19</b>
<b>2.1. Introduction .....</b>	<b>19</b>
<b>2.2. Experimental.....</b>	<b>21</b>
<b>2.3. Results and discussion.....</b>	<b>23</b>
<b>2.4. Conclusions .....</b>	<b>28</b>

### **Chapter 3.**

<b>Effect of Molybdenum Addition on the Microstructure and Mechanical Properties of Fe-Mo-B-C Sintered Alloys .....</b>	<b>58</b>
<b>3.1. Introduction .....</b>	<b>58</b>
<b>3.2. Experimental.....</b>	<b>60</b>
<b>3.3. Results and discussion.....</b>	<b>61</b>
<b>3.4. Conclusions .....</b>	<b>68</b>

### **Chapter 4.**

<b>Densification Mechanism and Microstructure Development of Fe-Ni Alloys Consolidated by Field Assisted Sintering .....</b>	<b>108</b>
<b>4.1. Introduction .....</b>	<b>108</b>
<b>4.2. Experimental.....</b>	<b>107</b>
<b>4.3. Results and discussion.....</b>	<b>109</b>
<b>4.4. Conclusions .....</b>	<b>114</b>

<b>Abstract in Korean.....</b>	<b>140</b>
--------------------------------	------------

## List of Figures

Figure 1.1. Schematic diagram of changes in mechanical properties according to sintered density

Figure 1.2. A schematic of the mechanism of densification in liquid phase sintering.

Figure 1.3. The principle of the liquid phase sintering and the schematic diagram of the microstructure changes during liquid phase sintering.

Figure 1.4. Examples of the microstructure variation with the liquid fraction changes. The white colored liquid area was Cu, and the dark colored solid grain was Co.

Figure 1.5. A conceptual outline of the changes associated with solution-precipitation densification where both grain growth and grain shape accommodation act to release liquid to fill residual pores.

Figure 1.6. A schematic of the mechanism of densification in liquid phase sintering.

Figure 1.7. A schematic illustration of the FAS machine.

Figure 1.8. Sample field assisted sintering tooling assembly.

Figure. 2.1. Ternary projection of the liquidus surface including solidification paths of the analyzed alloys.

Figure. 2.2. The effect of C addition on densification behavior of Fe-B alloys

Figure. 2.3. The elemental mapping and phase identification of FeBC-Ni steel sintered at 1250 °C

Figure. 2.4. Crack formation and propagation in Fe-B-C alloys

Figure. 2.5. Schematic diagram of the effect of microstructural modification in Fe-B-C based alloys

Figure. 2.6. Schematic diagram of the effect of Ni addition and post-annealing on microstructure of Fe-Ni-B-C alloys

Figure 2.7. Volume fraction of liquid phase in Fe-0.6B-0.8C, Fe-0.4B-0.8C, Fe-1Ni-0.6B-0.8C, and Fe-1Ni-0.4B-0.8C alloys as a function of temperature.

Figure 2.9. Apparent density of liquid phase sintered Fe-0.6B-0.8C, Fe-0.4B-0.8C, Fe-1Ni-0.6B-0.8C, and Fe-1Ni-0.4B-0.8C alloys.

Figure. 2.9 Green density of Fe-0.6B-0.8C, Fe-0.4B-0.8C, Fe-1Ni-0.6B-0.8C, and Fe-1Ni-0.4B-0.8C pellets prepared at a compacting pressure of 600 MPa.

Figure 2.10. Apparent density of Fe-0.6B-0.8C, Fe-0.4B-0.8C, Fe-1Ni-0.6B-0.8C, and Fe-1Ni-0.4B-0.8C alloys quenched from 1180 °C.

Figure 2.11. Optical and SEM micrographs of (a) Fe-0.6B-0.8C, (b) Fe-0.4B-0.8C, (c) Fe-1Ni-0.6B-0.8C, and (d) Fe-1Ni-0.4B-0.8C alloys

Figure 2.12. FE-SEM image of Fe-0.6B-0.8C alloy and chemical composition of selected areas by EDS measurements.

Figure 2.13. Apparent density of liquid phase sintered Fe-0.6B-0.8C, Fe-0.4B-0.8C, Fe-1Ni-0.6B-0.8C, and Fe-1Ni-0.4B-0.8C alloys.

Figure 2.14. Phase identification and fraction determined by EBSD in (a) Fe-0.6B-0.8C, (b) Fe-0.4B-0.8C, (c) Fe-1Ni-0.6B-0.8C, and (d) Fe-1Ni-0.4B-0.8C alloys.

Figure 2.15 Calculated phase changes during the solidification of Fe-0.6B-0.8C (dash line) and Fe-1Ni-0.6B-0.8C alloys (solid line) under the equilibrium condition.

Figure 2.16. Optical micrographs of Fe-0.6B-0.8C and Fe-1Ni-0.6B-0.8C alloys

quenched from 950 °C.

Figure 2.17. (a) Bulk hardness and (b) load-elongation curves of Fe-0.6B-0.8C, Fe-0.4B-0.8C, Fe-1Ni-0.6B-0.8C, and Fe-1Ni-0.4B-0.8C alloys.

Figure 2.18 Nanoindentation load-displacement curves of grain and grain boundary of (a, b) Fe-0.6B-0.8C and (c, d) Fe-1Ni-0.6B-0.8C alloys.

Figure 2.19. (a) Optical and (b) SEM micrographs of Fe-1Ni-0.4B-0.8C alloy post annealed at 1000 °C for 24 h, (c) low magnification HAADF-STEM image of grain and grain boundary in Fe-1Ni-0.4B-0.8C alloy and selected area diffraction patterns (SADPs) of (d) spot 1 ( $\alpha$ -Fe) and (e) spot 2 ((Fe, Ni)<sub>3</sub>(C, B)).

Figure 2.20. Optical and SEM micrographs of Fe-1Ni-0.6B-0.8C alloys quenched from 1180 °C.

Figure 2.21 Optical micrographs of Fe-1Ni-0.6B-0.8C alloys post annealed at 1000 °C for (a) 3h and (b) 12 h.

Figure 2.22. Apparent density of liquid phase sintered Fe-0.6B-0.8C, Fe-0.4B-0.8C, Fe-1Ni-0.6B-0.8C, and Fe-1Ni-0.4B-0.8C alloys.

Figure 2.23. Load-elongation curves of furnace cooled, quenched, and post annealed Fe-1Ni-0.4B-0.8C alloys.

Figure 3.1. Microstructures of the liquid phase sintered Fe-B-C based alloys without (a and b) NiB and (c and d) with NiB.

Figure 3.2. The schematic the microstructure development in Fe-Mo-B-C with low Mo content (0.5~1.5 wt%).

Figure 3.3. The schematic the microstructure development in Fe-Mo-B-C with high Mo content (>3.5

Figure 3.4. A Fe-Mo-0.4B-0.8C phase diagram as a function of the Mo content calculated using a thermodynamic database TCFE2000 of Thermo-Calc.

Figure 3.5. Sintered density of Fe-Mo-B-C alloys as a function of Mo content.

Figure 3.6. Optical micrographs of (a) Fe-0.4B-0.8C, (b) Fe-1Mo-0.4B-0.8C, (c) Fe-3Mo-0.4B-0.8C and (d) Fe-5Mo-0.4B-0.8C alloys.

Figure 3.7. Volume fraction of liquid phase in Fe-Mo-B-C alloys as a function of Mo content.

Figure 3.8. FE-SEM images (a) Fe-0.4B-0.8C, (b) Fe-1Mo-0.4B-0.8C, (c) Fe-3Mo-0.4B-0.8C, and (d) Fe-5Mo-0.4B-0.8C alloys and (e) EDS mapping images of grain boundary in Fe-5Mo-0.4B-0.8C alloy.

Figure 3.9. FE-SEM image of Fe-0.4B-0.8C alloy and chemical compositions of selected areas by EDS measurements.

Figure 3.10. EDS mapping images of (a) Fe-1Mo-0.4B-0.8C, (b) Fe-3Mo-0.4B-0.8C and (c) Fe-5Mo-0.4B-0.8C alloys.

Figure 3.11 Optical micrograph of Fe-4Mo-0.4B-0.8C alloy.

Figure 3.12. SEM images of Fe-0.4B-0.8C and Fe-5Mo-0.4B-0.8C alloys quenched from 950 °C.

Figure 3.13. (a) Low magnification HAADF-STEM image of grain boundary in Fe-5Mo-0.4B-0.8C alloy, selected area diffraction patterns (SADPs) of (b) spot 1 ((Fe,Mo)<sub>3</sub>(C,B)) and (c) spot 2 (MoFe(C,B)), and (d) HAADF-STEM image of spot 2 (MoFe(C,B)) observed by Cs-corrected STEM.

Figure 3.14. Point-scan EDS analysis and STEM-EDS mapping images of Fe-5Mo-0.4B-0.8C alloy.

Figure 3.15. Atomic structural models and lattice parameters of MoFe(C,B)

stabilized by relaxation of DFT calculation.

Figure 3.16. Simulated diffraction pattern of (a)  $\text{MoFe}(\text{C}_{0.25}\text{B}_{0.75})$ , (b)  $\text{MoFe}(\text{C}_{0.5}\text{B}_{0.5})$ , and (c)  $\text{MoFe}(\text{C}_{0.75}\text{B}_{0.25})$  from the DFT atomic structure by JEMS4 software and (d) experimentally obtained diffraction pattern of  $\text{MoFe}(\text{C},\text{B})$ .

Figure 3.17. SEM micrographs and EDS mapping images of Fe-5Mo-0.4B-0.8C alloy quenched from (a) 1180 and (b) 1080 °C.

Figure 3.18. A schematic illustration of microstructural development in Fe-B-C and Fe-Mo-B-C system during solidification.

Figure 3.19. Rockwell A hardness of Fe-Mo-B-C alloys as a function of Mo content.

Figure 3.20. (a) FE-SEM micrograph and (b) EDS mapping images of Fe-5Mo-0.4B-0.8C alloy after nano indentation experiment and (c) nanoindentation load-displacement curves for constituent phases in Fe-5Mo-0.4B-0.8C alloy.

Figure 3.21. Nanoindentation load-displacement curves of (a) grain and (b) grain boundary of Fe-0.4B-0.8C, Fe-1Mo-0.4B-0.8C, Fe-3Mo-0.4B-0.8C and Fe-5Mo-0.4B-0.8C alloys.

Figure 3.22. Load-elongation curves of Fe-Mo-B-C alloys as a function of Mo content.

Figure 3.23. Optical micrographs of (a) Fe-0.4B-0.8C, (b) Fe-1Mo-0.4B-0.8C, (c) Fe-3Mo-0.4B-0.8C, and (d) Fe-5Mo-0.4B-0.8C alloys after tensile test.

Figure 3.24. SEM images of (a) Fe-0.4B-0.8C, (b) Fe-1Mo-0.4B-0.8C, (c) Fe-3Mo-0.4B-0.8C, and (d) Fe-5Mo-0.4B-0.8C alloys after indentation test.

Figure 3.25. SEM image of Fe-5Mo-0.4B-0.8C alloy after indentation test (old one).

Figure 3.26. A Schematic diagram of the effect of lamellar structure on preventing

the crack propagation in Fe-Mo-B-C alloys.

Figure 3.27. Comparison of the measured tensile strength and elongation to failure of boron-containing alloys prepared by liquid phase sintering.

Figure 4.1. Sintered density of Fe-5Ni alloys prepared by FAS method depending on the sintering temperature.

Figure 4.2. Apparent density of Fe-xNi alloys sintered by CS, HP and FAS as a function of Ni contents ( $x = 0\sim 5$  in wt%).

Figure 4.3. (a) Green density of Fe-Ni alloys as a function of Ni content, and (b) FE-SEM image of Fe starting powder.

Figure 4.4. FE-SEM micrographs of pure Fe sintered by (a) CS and (b) FAS.

Figure 4.5. Optical micrographs of conventionally sintered Fe-xNi alloys. ((a)  $x = 0.1$ , (b)  $x = 0.5$ , (c)  $x = 1$  and (d)  $x = 5$ ).

Figure 4.6. FE-SEM micrographs and EDS mapping images of Fe-5Ni alloys sintered by (a) CS and (b) FAS.

Figure 4.7. SEM micrographs and EDS mapping images of Fe-5Ni alloys, which were sintered at 1150 °C for (a) 0 min, (b) 30 min, (c) 60 min, and (d) 120 min and water-quenched.

Figure 4.8. Sintered densities of Fe-5Ni alloys which were sintered at 1150 °C for 0~120 min and water-quenched.

Figure 4.9. OM, FE-SEM and EDS mapping images Fe-xNi alloys consolidated by FAS (a)  $x = 0.1$ , (b)  $x = 0.5$  and (c)  $x = 1$ .

Figure 4.10. SEM micrographs and EDS mapping images of Fe-5Ni alloy consolidated by FAS, and chemical compositions (at%) of selected points.

Figure 4.11. (a) Apparent density of CS-1000, HP-1000, FAS-1000, and FAS-1000P alloys

Figure 4.12. FE-SEM micrographs and EDS mapping images of (a) CS-1000, (b) HP-1000, and (c) FAS-1000P alloys.

Figure 4.13. FE-SEM images of Fe-5Ni alloys as a function of mechanical pressure: (a) 37.7 MPa, (b) 45 MPa and (c) 68.8 MPa.

Figure 4.14. (a) The area fraction of Ni-rich phases in Fe-5Ni alloys as a function of mechanical pressure, and their (b) apparent densities and bulk hardness.

Figure 4.15. (a) Low magnification HAADF-STEM and EDS mapping images of fine grains (Ni-rich region), and selected area diffraction patterns (SADPs) of (b) spot 1, (c) spot 2, and (d) spot 3, and (e) EDS line scanning profile across the specimen as marked by the line.

Figure 4.16 Apparent density of CS-1000, HP-1000, FAS-1000, and FAS-1000P alloys

Figure 4.17. The cross-sectional images of simple Fe-Ni diffusion couples prepared by (a) CS (1150 °C for 120 min), (b) HP (1000 °C for 10 min) and (c) FAS (1000 °C for 10 min) with their elemental mapping of Ni K.

Figure 4.18. Rockwell A hardness of Fe-xNi alloys sintered by CS, HP and FAS as a function of Ni contents ( $x = 0\sim 5$  in wt%).

Figure 4.19. Rockwell C hardness of Fe-5Ni alloys consolidated by CS, HP and FAS.

## List of Abbreviations

P/M	Powder metallurgy
CS	Conventional solid state sintering
LPS	Liquid phase sintering
SPS	Spark plasma sintering
FAS	Field assisted sintering
HP	Hot pressing
OM	Optical microscopy
SEM	Scanning electron microscope
EBSD	Electron backscatter diffraction
TEM	Transmission electron microscopy
EDS	Energy dispersive X-ray spectroscopy
SAED	Selected area electron diffraction
M <sub>2</sub> B	M <sub>2</sub> (C,B) type boride (M=Fe, Mo ,Ni etc)
M <sub>3</sub> B	M <sub>3</sub> (C,B) type carbide (M=Fe, Mo ,Ni etc)
DFT	Density functional theory
FIB	Focused ion beam technique
VASP	Vienna Ab Initio Simulation Package
HAADF	High angle annular dark field
Thermo-Calc.	Thermo Calculation software
α-Fe	Ferrite
γ-Fe	Austenite

# **Chapter 1. General background**

## **1.1. Powder metallurgy (P/M)**

Powder metallurgy (P/M) is well-known technology for the manufacture of parts from raw starting powders by compaction and heating. The heating process is mainly performed at a temperature lower than the melting point of the raw powders, and this process is called sintering. P/M technique has been used in various industries and applications, because of its efficiency and net-shaped capability [1-3]. Recently, ferrous P/M parts account for most of the powder metallurgy, and its usage in automobile industry is increasing every year [4,5]. However, conventional solid state sintering produces sintered parts with porosity, thus the requirements of mechanical properties are not satisfied due to the presence of porosity ranging from 5 to 15 vol. % [6]. Since mechanical properties such as tensile strength and elongation increased with the sintered density, and thus sintered density is the key factor with respect to the mechanical properties of sintered specimen [7]. Fig. 1.1 presents the schematic diagram of changes in mechanical properties according to sintered density.

To develop the improved mechanical properties of Fe-based alloys for various applications, several strengthening mechanisms have been investigated. For example, solid-solution, precipitation and microstructural design are the typical strengthening mechanisms in Fe-based alloys.

### 1.1.1 Solid-solution

Solid-solution strengthening is well-known technique for Iron (Fe)-based alloys to improve the mechanical properties. When adding an alloying elements to the lattice, atomic displacement provides stronger obstacle to dislocation motion through stress field [8,9]. Depending on the size of the alloying element, interstitial solid solution and substitutional solid solution can be occurred. Boron (B) and Carbon (C) are primarily interstitial solid solutions studied in Fe-based alloys [10,11]. Boron (B) element has all the features of an effective sintering enhancer for ferrous systems with high hardenability and mechanical properties, resulting from the eutectic reaction. In addition, Carbon (C) is an indispensable element for PM alloy steels due to its low cost and high mechanical properties. These interstitial atoms not only are solid-soluted in Fe, but also form boride or carbide, which dramatically improves hardness and strength. On the other hands, alloying elements commonly used to form the substitutional solid solutions include nickel (Ni), Chromium (Cr), Molybdenum (Mo), vanadium (V), silicon (Si), titanium (Ti), tungsten (W) and manganese (Mn) [12-19]. When these atoms are solid-soluted, local lattice distortion results in an increase in strength of Fe-based alloys.

### 1.1.2 Precipitation

Precipitation hardening is one of common strengthening mechanisms in Fe-based alloys. Due to the difference between the temperature and solubility limit, secondary phases can be formed according to the phase diagram. For this reason, these second precipitates (intermetallic compound and impurity phase) are formed by heat

treatment such as quenching, tempering and tempering [20,21]. Also, the second phase precipitates impede the movement of dislocations and defects, thus improving the mechanical properties [22]. This strengthening effect is due to both modulus effect and interfacial energy (surface energy).

### 1.1.3 Phase & Microstructure

The role of microstructure in explaining the mechanical properties for Fe-based alloys. The traditional well-known method to improve the strength of Fe-based alloys is a decrease of grain size according to the Hall-Petch equation [23]. However, there is a typical trade-off relationship between strength and elongation. For this reason, microstructural design of Fe-based alloys has attracted increasing interest for mechanical properties. The manganese twinning-induced plasticity (TWIP) steel has the most beneficial effect on decrease of the dislocation mean free path, thus increasing both strength and ductility [24,25]. The addition of ductile phases to alloys has also been investigated to be an effective to improve the fracture resistance of a given materials. Similarly, compounds reinforced with additional phase or intermetallic contribute to improve the mechanical properties by hindering the dislocation motion [26-28]. These approaches have similar strategies to improve the mechanical properties of the Fe-based alloy by designing microstructures that facilitate or interfere with crack propagation.

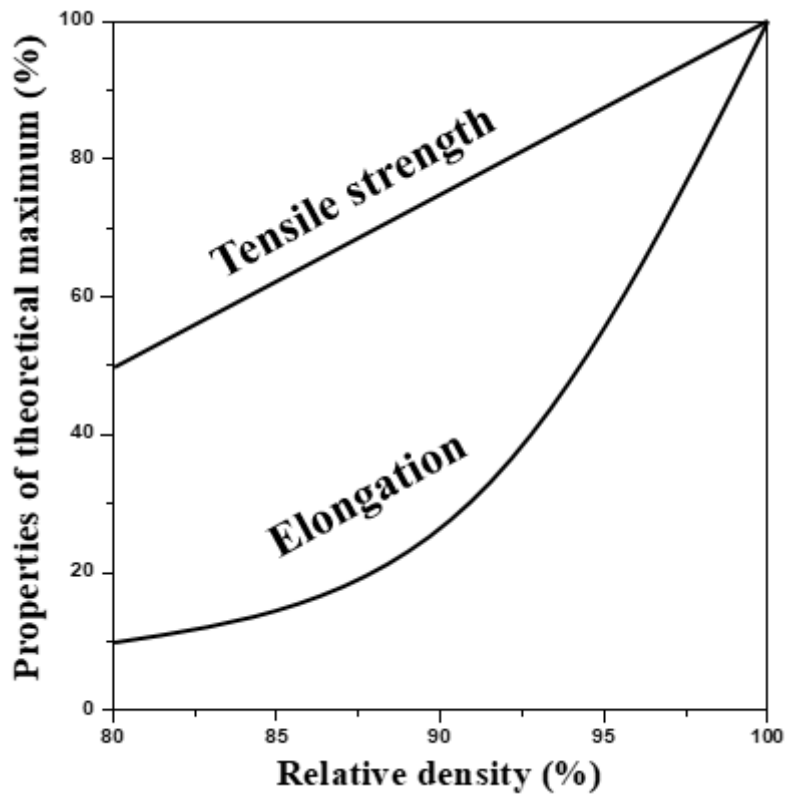


**Figure 1.1.** Schematic diagram of changes in mechanical properties according to sintered density

## 1.2. Liquid phase sintering (LPS)

Liquid phase sintering (LPS) is one of promising technique to assist densification by sintering the compaction of raw powder above the liquidus line of the phase diagram [29]. For this reason, the liquid phase exists at the sintering temperature and liquid phase improves the mass transfer and diffusion. The concept of liquid phase sintering was invented based on the idea of firing ceramics with a glass bond, and was further developed in the 1930s based on several materials such as WC-Co, Cu-Sn, W-Ni-Cu, Fe-Cu-C and TiC-Fe [30-34].

Cannon and Lenel suggested an initial concept model by dividing the mechanism of liquid phase sintering into three states: rearrangement, solution-precipitation and solid-state sintering (Fig. 1.2) [35]. The schematic diagram of the microstructure changes during liquid phase sintering also shows the mechanism of densification in liquid phase sintering (Fig. 1.3). The solid grains coalesce together with neck growth [36], when the first liquid spreads. The solid grains are partially soluble in the liquid phase, and this solubility results in the liquid to wet the solid. In this case, high diffusion rates are associated with liquids and induces the grain arrangement, thus assisting the densification [37]. Then, microstructural change was controlled by dihedral angle and liquid volume fraction in the solution-precipitation step [38]. With low dihedral and contact angles, the liquid can promote the densification in liquid phase sintering [39]. Also, the microstructural change can be varied by the volume fraction of liquid phase [40]. For example, in the Co-Cu system [41], solid grains gradually changed into spherical structure and densification was accelerated

between solid-liquid contacts as increasing the liquid phase (Fig. 1.4). However, the simulation of liquid phase sintering shows that the distortion and shrinkage was occurred in the specimen, when there is too much liquid phase [42]. After the solution-precipitation step, the liquid phase solidifies to produce a networked composite microstructure during cooling [43]. As a result, microstructure was composed of grain, solidified liquid phase, and residual pores after liquid phase sintering and results in the final densification (Fig. 1.5).

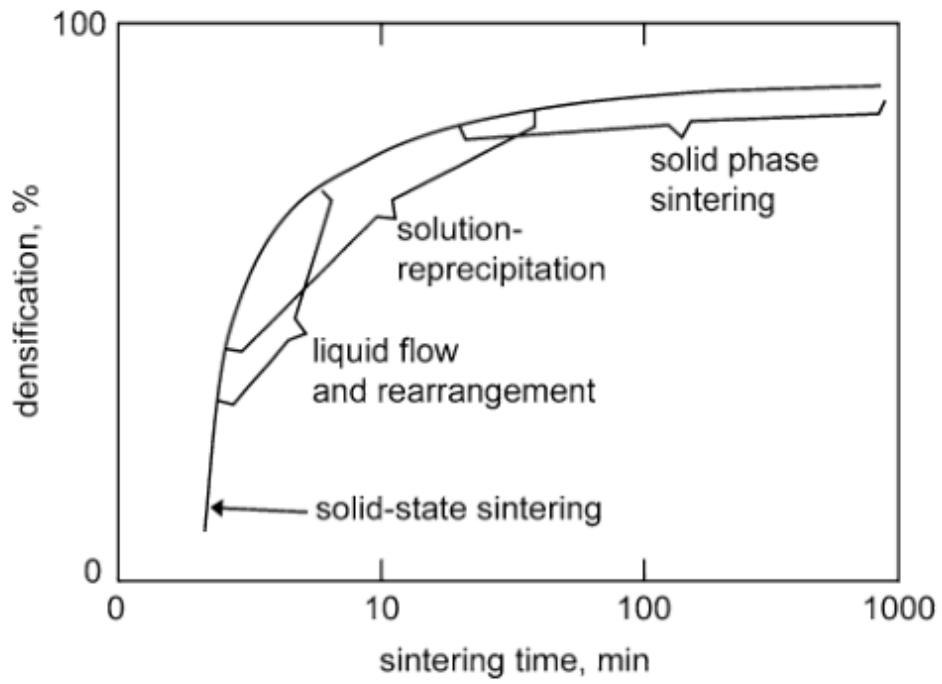


**Figure 1.2.** A schematic of the mechanism of densification in liquid phase sintering

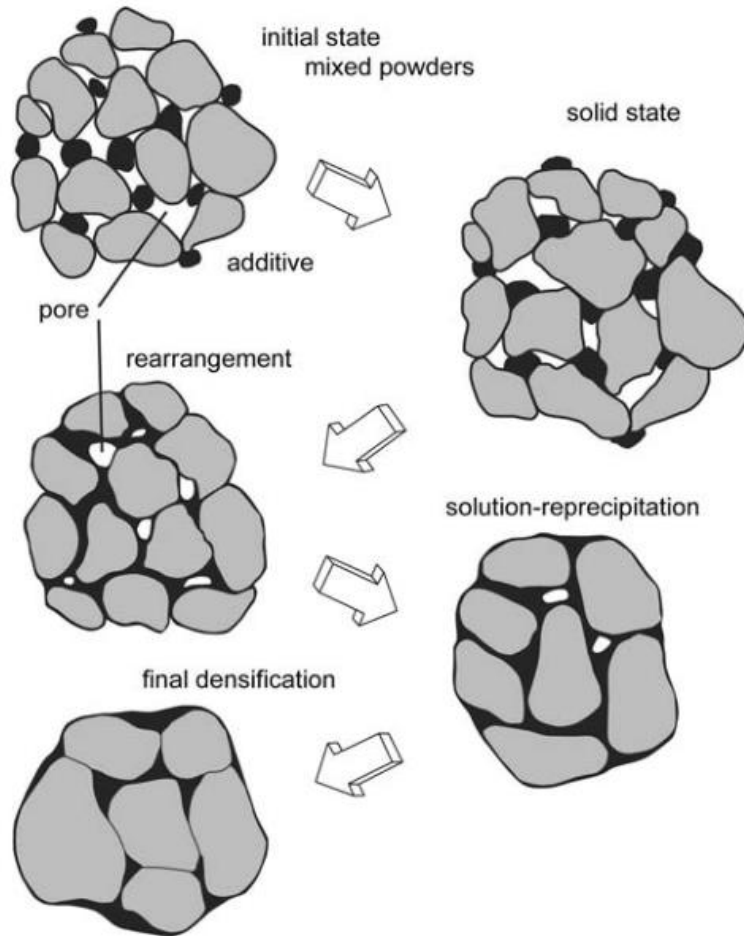


**Figure 1.3.** The principle of the liquid phase sintering and the schematic diagram of the microstructure changes during liquid phase sintering

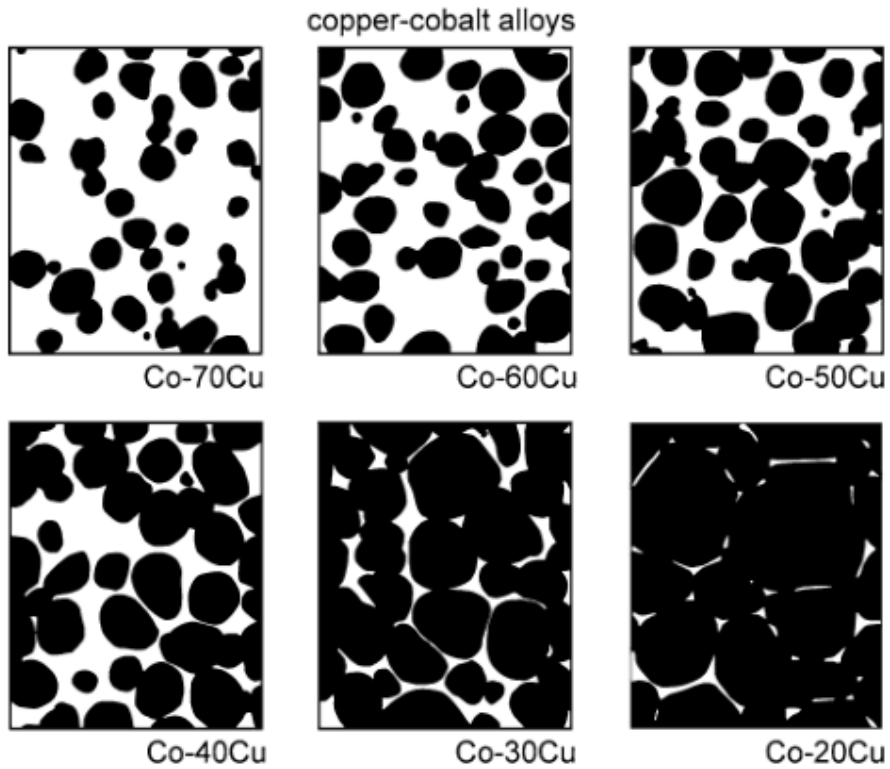


**Figure 1.4.** Examples of the microstructure variation with the liquid fraction changes. The white colored liquid area was Cu, and the dark colored solid grain was Co.

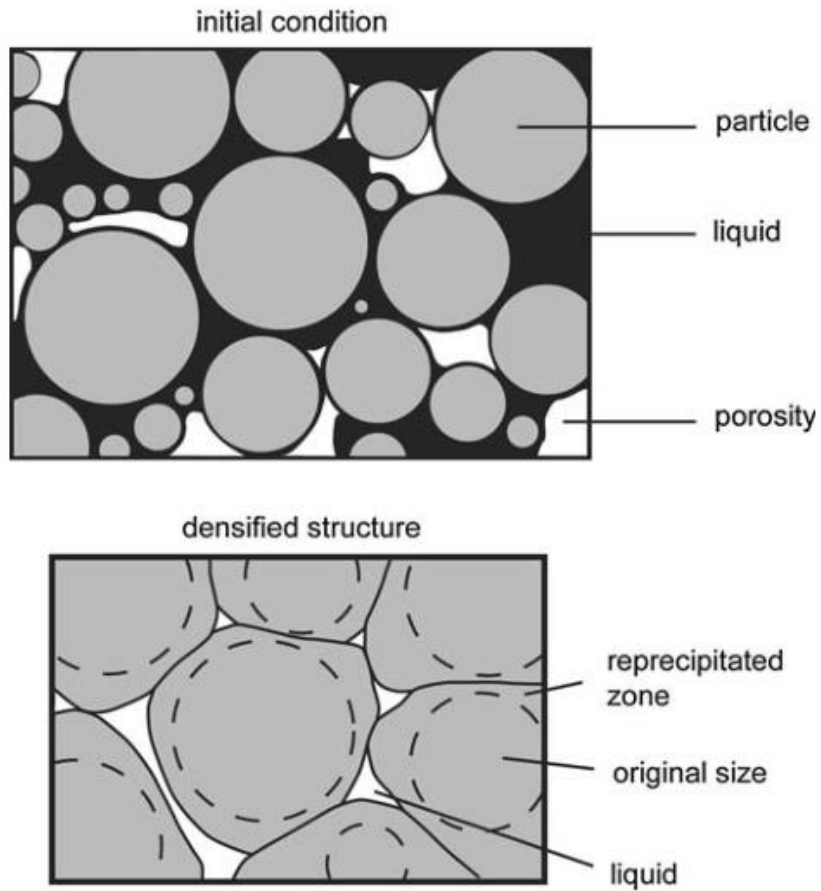


**Figure 1.5.** A conceptual outline of the changes associated with solution-precipitation densification where both grain growth and grain shape accommodation act to release liquid to fill residual pores

### **1.3. Field assisted sintering (FAS)**

Field assisted sintering (FAS), or spark plasma sintering (SPS), is a promising process, which can sinter the high-dense materials. FAS can consolidate the metal or ceramic powder in a short period, without substantial grain growth, and providing a high pulsed current throughout the compaction [44-46]. For this reason, FAS has been used to sinter the various materials such as nano powder, intermetallic compound and metal/ceramic composite [47-49].

Firstly, the idea of FAS was invented in the 1960s by Inoue et al by sintering under pulsed current [50], and more than 9700 papers have been reported according to the Web of Science. The mechanisms of FAS is known to be densified due to mechanical, thermal and electrical effects [51]. The schematic diagram shows that electric current through the particle leads to the neck growth, which can enhance the densification (Fig. 1.6). Recently, Zhang et al reported that the high temperature spark plasma could be generated due to the discharge effect and the densification can be attributed to the combination of spark discharge, Joule heating, electrical diffusion and plastic deformation effect [52], but the mechanism of FAS is still highly controversial.

The FAS machine system consists of a water-cooled vacuum chamber with atmosphere control system, a pyrometer, a DC pulse power and electrode with a vertical single-axis press (Fig 1.7). To maximize the thermal and electrical effect produced by Joule heating, raw powder is prepared in the graphite die and punches with spacers (Fig. 1.8).

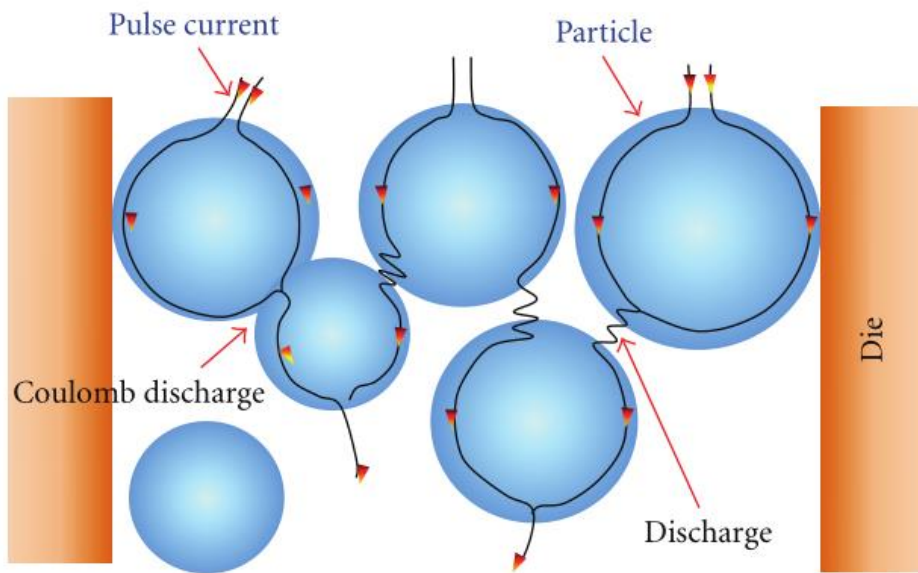


**Figure 1.6.** A schematic of the mechanism of densification in liquid phase sintering

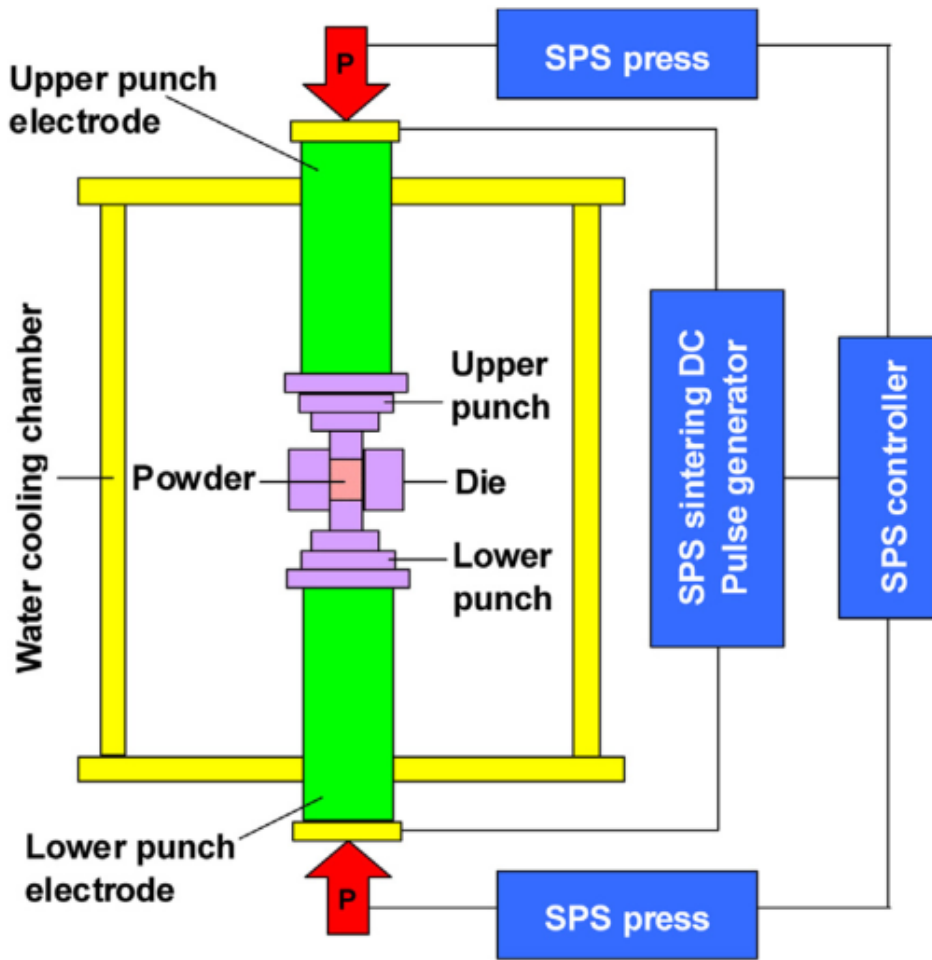
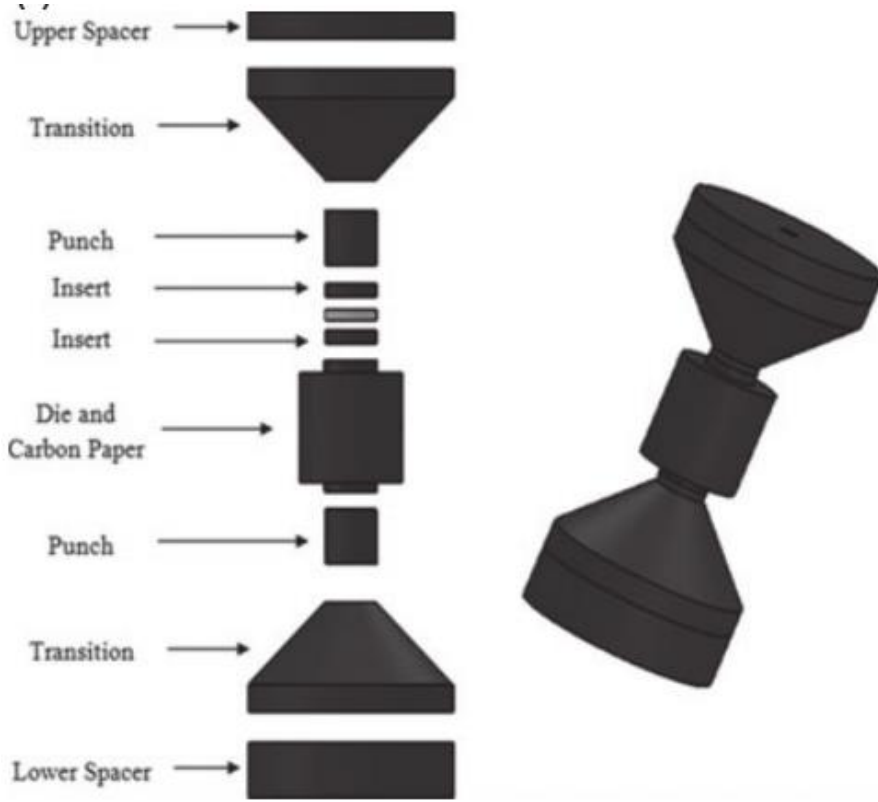


Figure 1.7. A schematic illustration of the FAS machine.



**Figure 1.8.** Sample field assisted sintering tooling assembly

## Reference

- [1] P. C. Angelo, R. Subramanian, Powder metallurgy: Science technology and applications (2009) 1-18.
- [2] C. –J. Yu, H. H. Eifert, J. Banhart, J. Baumeister, Mater. Res. Innov. 3 (1998) 181-188.
- [3] H. Fayazfar, M. Salarian, A. Rogalsky, D. Sarker, Paola Russo, V. Paserin, E. Toyserkani, Mater. Des. 144 (2018) 98-128.
- [4] S. Akhtar, M. Saad, M. R. Misbah, M. C. Sati, Today: SAVE Proc. 5 (2018) 18649-18655.
- [5] P. Ramakrishnan, Automotive Applications of Powder Metallurgy (2013) 493-519.
- [6] K.S. Narasimhan, Mater. Chem. Phys. 67 (2001) 56-65.
- [7] M. Yakout, M. A. Elbestawi, S. C. Veldhuis, J. Mater. Process. Tech. 266 (2019) 397-420.
- [8] L. Vitos, J. –O. Nilsson, B. Johansson, Acta Mater. 54 (2006) 3821-3826.
- [9] H. Essoussi, S. Ettaqi, E. Essadiqi, Procedia Manuf. 22 (2018) 129-134.
- [10] D. H. Jack, K. H. Jack, Mater. Sci. Eng. 11 (1973) 1-27
- [11] Y. Hayashi, T. Sugero, Acta Mater. 18 (1970) 693-697.

- [12] N. Chawla, D. Babic, J. J. Williams, S.J. Polasik, *Advances in powder metallurgy & particulate materials*, MPIF, Princeton 104 (2002)
- [13] H. Zhang, B. Johansson, R. Ahuja, L. Vitos, *Comput. Mater. Sci.* 55 (2012) 269-272.
- [14] F. Han, B. Hwang, D. -W. Suh, Z. Wang, D. L. Lee, S. -J. Kim, *Met. Mater. Int.* 14 (2008) 667-672.
- [15] S. S. Bhatnagar, B. K. Guha, R. K. Sinha, *J. Mater. Sci.* 14 (1979) 1631-1640.
- [16] V. Ollilainen, W. Kasprzak, L. Holappa, *J. Mater. Process. Tech.* 134 (2003) 405-412.
- [17] L. J. Cuddy, H. E. Knechtel, W. C. Leslie, *Metall. Trans.* 5 (1974) 1999-2003
- [18] Y. Lv, Y. Sun, J. Zhao, G. Yu, J. Shen, S. Hu, *Mater. Des.* 39 (2012) 303-308.
- [19] C. Scott, B. Remy, J. -L. Collet, A. Cael, C. Bao, F. Danoix, B. Malard, C. Curfs, *Int. J. Mater. Res.* 102 (2011) 538-549.
- [20] M. H. Jacobs, A. G. Doggett, M. J. Stowell, *J. Mater. Sci.* 9 (1974) 1631-1643.
- [21] P. Liu, A. H. Stigenberg, J. -O. Nilsson, *Acta Metall. Mater.* 43 (1995) 2881-2890.
- [22] A. Deschamps, M. Militzer, W. J. Poole, *ISIJ Int.* 41 (2001) 196-205.
- [23] J. W. Morris, *Proceedings of the international symposium on ultrafine grained steels*, Tokyo: Iron and Steel Institute (2001) 34.
- [24] S. Liu, L. Qian, J. Meng, D. Li, P. Ma, F. Zhang, *Scr. Mater.* 127 (2017) 10-14.

- [25] I. Jutierrez-Urrutia, D. Raabe, *Acta Mater.* 60 (2012) 5791-5802.
- [26] J. Inoue, S. Nambu, Y. Ishimoto, T. Koseki, *Scr. Mater.* 59 (2008) 1055-1058.
- [27] C. T. Cui, J. T. Guo, Y. H. Qi, H. Q. Ye, *Mater. Sci. Eng. A* 396 (2005) 194-201.
- [28] S. Cheng, Y. H. Zhao, Y. T. Zhu, E. Ma, *Acta Mater.* 55 (2007) 5822-5832.
- [29] R. M. German, Plenum Press, London (1985).
- [30] S. Kim, S. -H. Han, J. -K. Park, H. -E. Kim, *Scr. Mater.* 48 (2003) 635-639.
- [31] M. Azadbeh, H. Danninger, C. Gierl-Mater, *Powder Metall.* 56 (2013) 342-346.
- [32] D. N. Yoon, W. J. Huppmann, *Acta Metall.* 27 (1979) 693-698.
- [33] S. J. Jamil, G. A. Chadwick, *Powder Metall.* 28 (1985) 65-71.
- [34] P. Persson, A. E. W. Jarfors, S. Savage, *J. Mater. Process. Tech.* 127 (2002) 131-139.
- [35] H. S. Cannon, F. V. Lenel, *Plansee proceedings. Metallwerk Plansee. Reutte, Austria* (1953).
- [36] W. D. Kingery, M. D. Narasimhan, *J. Appl. Phys.* 30 (1958) 307-310.
- [37] J. Liu, R.M. German, *Metall. Mater. Trans. A*, 32 (2001) 3125-3131.
- [38] R. M. German, *Metall. Trans. A* 16 (1985) 1247-1285.
- [39] P. Chhillar, S. Sangal, A. Upadhyaya, *Z Metallkd.* 95 (2004) 3-7.
- [40] J. Liu, R.M. A. Lal, R. M. German, *Acta Mater.* 47 (1999) 4615-4626.
- [41] C. H. Kang, D. N. Yoon, *Metall. Trans. A* 12 (1981) 65-69.

- [42] S. J. Park, S. H. Chung, J. L. Johuson, R. M. German, *Mater. Trans.* 47 (2006) 2745-2752.
- [43] J. Lentz, A. Röttger, W. Theisen, *Acta Mater.* 99 (2015) 119-129.
- [44] E. A. Olevsky, W. L. Bradbury, C. D. Haines, D. G. Martin, D. Kapoor, *J. Am. Ceram. Soc.* 95 (2012) 2406-2413.
- [45] S. Diouf, A. Molinari, *Powder Tech.* 221 (2012) 220-227.
- [46] S. R. Oke, O. O. Ige, O. E. Falodun, A. M. Okoro, M. R. Mphahlele, P. A. Olubambi, *Int. J. Adv. Manuf. Tech.* 102 (2019) 3271-3290.
- [47] N. Saheb, Z. Iqbal, A. Khalil, A. S. Hakeem, N. A. Aqeeli, T. Laoui, A. -Q. R. Kirchner, *J. Nanomater.* 2012 (2012) 1-13.
- [48] R. Li, T. Yuan, X. Liu, K. Zhou, *Scr. Mater.* 110 (2016) 105-108.
- [49] I. J. Shon, Z. A. Munir, *J. Am. Ceram. Soc.* 79 (1996) 1875-1880.
- [50] K. Inoue, US Patent 3,340,052, 1967.
- [51] O. Guillon, J. Gonzalez-Julian, B. Dargatz, T. Kessel, G. Schierning, J. Räthel, M. Herrmann, *Adv. Eng. Mater.* 16 (2014) 830-849
- [52] Z. -H. Zhang, Z. -F. Liu, J.-F. Lu, X. -B. Shen, F. -C, Wang, Y. -D. Wang, *Scr. Mater.* 81 (2014) 56-59.

# **Chapter 2. Microstructure modification of liquid phase sintered Fe-Ni-B-C alloys for high mechanical properties**

## **2.1. Introduction**

Powder metallurgy (P/M) is an efficient process for manufacturing the mechanical parts of high quality and accuracy at low cost [1]. However, the use of conventionally sintered products is limited due to their low relative density of 85 to 95% [2]. Liquid phase sintering (LPS) is a consolidation process of powder compacts at the temperature above the solidus of more than one component, that is, in the presence of wetting liquid phase. The densification can be achieved via particle rearrangement, solution-precipitation, and coarsening and grain growth [3,4]. The appropriate amount of liquid phase during LPS is known to be 5~15 vol.% [4,5]. Among the various alloying elements for LPS [6-8], boron (B) has all the features of an effective sintering enhancer for ferrous systems with high hardenability and mechanical properties, resulting from the eutectic reaction ( $\gamma\text{-Fe} + \text{Fe}_2\text{B} \rightarrow \text{L}$ ) [9-13] (Fig. 2.1). Carbon (C) is an indispensable element for P/M alloy steels due to its low cost and high mechanical properties (Fig. 2.2) [14,15], and also facilitates the LPS densification by lowering the temperature of liquid formation [16-18]. Moreover, several attempts have been made to further improve the densification and mechanical

properties of boron-containing alloys through the addition of alloying elements such as Mo, Cu, Cr, Al, and Mn [19-23]. Among them, nickel (Ni) is an important element for Fe-based alloys due to its high strength, hardenability, and solid solution strengthening [24-26]. Several studies have reported that the Ni addition to the Fe-B system accelerated the boron diffusion in  $\alpha$ -Fe similar to carbon and decreased the temperature for eutectic reaction and thus, improved the densification of boron-containing alloys [27-30]. In addition, Wu et al. found that the Ni addition to the Fe-Mo-B-C steels lowered the temperature of eutectic reaction, resulting in the microstructural change from  $\text{Fe}_2\text{B}$  and  $\text{Fe}_3(\text{C},\text{B})$  to  $\text{M}_3(\text{C},\text{B})$  (Ni  $\sim$ 0.8 at%) (Fig. 2.3) [31,32]. Likewise, the addition of the appropriate alloying elements was beneficial to the densification of boron-containing alloys, however, the improvement of elongation property was very limited because a large amount of liquid phase produced the continuous network of eutectic hard phases ( $\text{M}_2\text{B}_6$ ,  $\text{M}_3\text{B}$ , and  $\text{M}_2\text{B}$ ) at the grain boundaries (Fig. 2.4) [33,34].

Recently, the mechanical properties of liquid phase sintered alloys have been studied based on the microstructural modification, which prevented the continuous network of eutectic phases and increased the grain continuity [35-37]. Several studies suggested that the microstructure of boron-containing alloys can be modified by composition [9,12] and heat treatment [36,38] (Fig. 2.5). Peng et al. reported that the amount of boron-carbides remarkably decreased as the boron content decreased [10]. Lentz et al. found that the volume fraction of the eutectic hard phases ( $\text{Fe}_3(\text{C},\text{B})$  and  $\text{Fe}_2\text{B}$ ) decreased by lowering the  $\text{B}/(\text{B}+\text{C})$  ratio of Fe-B-C alloys [12]. In addition, Li et al. suggested that the heat treatment has the effects on the morphology of hard phase, which obviously prevented the formation of continuous hard phase

network [38]. Liu et al. indicated that the boride network was broken up and changed into isolated distribution after heat treatment [36]. It is speculated that the ductile property of Fe-Ni-B-C alloys can be improved through the composition control and heat treatment, which optimize the volume fraction of solidified phases and reduce the continuous network of eutectic phases (Fig. 2.6). However, the effect of microstructure modification on mechanical properties of Fe-Ni-B-C alloys has been rarely investigated.

The objective of the present study was focused on improving the elongation to failure in Fe-B-C ternary alloys. The Ni addition was introduced to promote the eutectic reaction and thus, improve the densification of boron-containing alloys. To reduce the continuous network of hard eutectics, the composition was controlled to achieve the system with the optimized hard phase fraction, and heat treatment was performed to induce the coarsening of solidified  $\alpha$ -Fe particles into the matrix. In addition, the effects of microstructure modification on the mechanical properties of Fe-Ni-B-C alloys were thoroughly investigated. Under the optimized condition, the post-annealed Fe-1Ni-0.4B-0.8C alloy exhibited a significant increase of ductility (elongation to failure).

## **2.2. Experimental**

The starting powders used for sintering were commercially available water-atomized iron (<150  $\mu\text{m}$ , ASC100.29, Hogan's), boron ( $\sim 15$   $\mu\text{m}$  (D50), iNexus, Inc.), synthetic graphite (<20  $\mu\text{m}$ , Sigma Aldrich), and nickel (<50  $\mu\text{m}$ , Sigma Aldrich)

powders. The investigated compositions were Fe-0.6B-0.8C, Fe-0.4B-0.8C, Fe-1Ni-0.6B-0.8C and Fe-1Ni-0.4B-0.8C in wt%. The powder mixture was prepared by hand or V-mixer and compacted into  $\varnothing$ 10 mm pellets at a compacting pressure of 600 MPa without a lubricant. All the samples were sintered at 1180 °C for 3 h in a vacuum ( $10^{-2}$ ~ $10^{-3}$  torr). The water quenching was carried out at a cooling rate of 150 °C/min and the post annealing was performed at 1000 °C for 0~24 h under a vacuum condition ( $10^{-2}$ ~ $10^{-3}$  torr). The sintered density (apparent density) of Fe-Ni-B-C alloys was determined by Archimedes immersion method. For the microstructure observation, the surface of sintered samples was prepared by grinding, mechanical polishing with diamond slurry down to 0.25  $\mu$ m, and then electro-polishing using 10 % perchloric acid and 90 % methanol solution for 30 s, and investigated by optical microscopy (Nikon L-150, OM), scanning electron microscope (Fe-SEM, SU-70) equipped with electron backscatter diffraction (EBSD) and energy dispersive X-ray spectroscopy (EDS). For transmission electron microscopy (TEM, Tecnai F20, FEI) observation, the cross sectional specimen was prepared by focused ion beam (FIB, Helios Nano Lab450, FEI) technique. The bulk hardness was measured by using Rockwell A hardness measurement (Mitutoyo, Japan) on the polished surface, and the nano indentation was carried out by Hysitron TriboLab 750 Ubi nano-indentation system equipped with a Berkovich indenter. For the tensile test, the specimens were prepared as per MPIF standard 10 and a small amount of lubricant (0.4 wt%, Kenolube) was used to minimize the friction between pressing die and specimen. The tensile test was carried out using a universal testing machine (Instron 5584) with a strain rate of 1.86 mm/min.

### 2.3. Results and discussion

The volume fraction of liquid phase in Fe-B-C and Fe-Ni-B-C alloy systems was calculated with Thermo-Calc [39] using a TCFE 2000 thermodynamic database (Fig. 2.7). The Ni addition to Fe-B-C system slightly decreased the liquid phase formation temperature and increased the volume fraction of liquid phase, because Ni contributes to the formation of  $\gamma$ -Fe and promotes the eutectic reaction  $\gamma$ -Fe + Fe<sub>2</sub>B → L [27-32]. When the B content decreased from 0.6 to 0.4 wt% at fixed C content of 0.8 wt%, the volume fraction of liquid phase significantly decreased from 26 to 18 vol% at 1180 °C. As a result, the apparent density of Fe-0.4B-0.8C alloy (7.65 g cm<sup>-3</sup>) was higher than that of Fe-0.6B-0.8C alloy (7.44 g cm<sup>-3</sup>) (Fig. 2.8), possibly due to the appropriate amount of liquid phase for pore filling in green compacts. The relative green density was in the range of 89.7~91.1 % at a compacting pressure of 600 MPa (Fig. 2.9). In addition, the Ni addition promoted the densification and thus, Fe-Ni-B-C alloys showed the higher apparent density compared to the Fe-B-C alloys. Furthermore, the apparent density of quenched Fe-Ni-B-C alloy had the higher density than that of quenched Fe-B-C alloy, indicating that the Ni-containing liquid phase enhanced the diffusion and promoted the densification at the sintering temperature (Fig. 2.10). The slightly lower apparent density of quenched alloys compared to the furnace-cooled counterparts can be attributed to the limited diffusion leading to the densification during solidification.

The optical and SEM micrographs of liquid phase sintered Fe-B-C and Fe-Ni-B-C alloys are shown in Fig 2.11. The Fe-B-C alloys showed the typical liquid phase

sintered microstructure consisting of spherical grains (pearlite and re-precipitated ferrite) and  $\alpha$ -Fe particle embedded  $\text{Fe}_3(\text{C}, \text{B})$  continuous network (Fig. 2.11(a) and (b)). The EDS analysis further confirmed the constituent phases and element distribution in the Fe-B-C alloy (Fig. 2.11). On the other hand, the re-precipitated ferrite was not observed in the Fe-Ni-B-C alloys and the microstructure of Fe-Ni-B-C alloys was composed of pearlite grains and  $\alpha$ -Fe particle embedded  $(\text{Fe}, \text{Ni})_3(\text{C}, \text{B})$  grain boundaries (solidified phases) (Fig.2.11(c) and (d)). The OM and SEM images also indicated that the decrease of B content in Fe-B-C and Fe-Ni-B-C alloys decreased the extent of agglomeration of solidified phases, resulting in the increase of grain continuity. The point EDS analysis indicated that Ni was relatively homogeneously present at both grains and grain boundaries, and the Ni addition did not change the hard phases ( $\text{Fe}_3\text{C}$  type) and distribution of B and C (Fig. 2.13) [31,32].

The volume fraction of solidified phases in the sintered alloys was determined by electron backscatter diffraction (EBSD) (Fig.2.14). Consistent with the Thermo-Calc results (Fig. 2.7), the decrease of B content from 0.6 to 0.4 wt% decreased the volume fraction of solidified phases from 15~16 to 10 %, which led to the increase of grain continuity. However, the addition of 1 wt% Ni did not significantly change the content of solidified phases. To investigate the effect of Ni addition on the microstructure development, the phase change during the solidification of Fe-0.6B-0.8C and Fe-1Ni-0.6B-0.8C alloys was calculated by Thermo-Calc. under the equilibrium condition (Fig. 2.15) [12,29]. As the temperature was lowered from sintering temperature, the amount of liquid was rapidly dropped and the liquid

transformed to the solidified phases (M2B and M23C6) along with the progress of the solidification process. Upon the subsequent cooling, phase transformation and diffusion occurred resulting in the pearlite grain ( $\alpha$ -Fe and Fe<sub>3</sub>C) and hard phase (Fe<sub>3</sub>(C, B) or (Fe, Ni)<sub>3</sub>(C, B)). The Ni addition to the Fe-B-C system facilitated the eutectic reaction [31,32], and thus the fraction of solidified phases (M2B, M23C6 and Fe<sub>3</sub>C) increased compared to that in Fe-0.6B-0.8C alloy. In addition, a complete austenite decomposition to ferrite and carbides has been observed at the higher temperature. The microstructure of the Fe-0.6B-0.8C and Fe-1Ni-0.6B-0.8C alloys quenched from 950 °C (below the solidus temperature) was further examined to investigate the effect of Ni addition on the microstructure development (Fig. 2.16). From this period,  $\gamma$ -Fe particles formed from the liquid were diffused and coalesced into the matrix grain. A large number of  $\gamma$ -Fe particles were observed at the grain boundaries of quenched Fe-0.6B-0.8C alloy (Fig. 2.16(a)). Upon the subsequent cooling, phase transformation and rearrangement occurred exhibiting the spherical grains composing of pearlite and ferrite in Fe-0.6B-0.8C alloy (Fig. 2.11(a)). On the other hand, most of  $\gamma$ -Fe particles were diffused into Fe matrix before the transformation to pearlite, resulting in the coalesced grains in quenched Fe-1Ni-0.6B-0.8C alloy (Fig. 2.16(b)). It implied that the Ni addition also facilitated the diffusion of solidified  $\gamma$ -Fe during solidification, which lead to the improved densification (7.44 vs. 7.75 g cm<sup>-3</sup>) and induced the microstructure change from pearlite/re-precipitated ferrite to pearlite.

To examine the effects of composition on the mechanical properties, hardness and tensile tests were carried out on the sintered specimens. Figure 2.17(a) represents the

bulk hardness of Fe-B-C and Fe-Ni-B-C alloys determined by Rockwell A hardness measurement. With Ni addition, the bulk hardness of Fe-Ni-B-C alloys greatly increased from 33.3~34.5 to 53.1~58.8, which can be attributed to the enhanced density, solid solution strengthening, and microstructural change of grains from pearlite and re-precipitated ferrite to pearlite and of grain boundary from  $\text{Fe}_3(\text{C}, \text{B})$  to  $(\text{Fe}, \text{Ni})_3(\text{C}, \text{B})$ . With decreasing the B content, the sintered density increased in both systems, but the bulk hardness of the Fe-Ni-B-C alloy slightly decreased from 58.8 to 53.1, which can be attributed to the decrease of the volume fraction of solidified phases from 15~16 to 10% with decreasing the B content. To compare the hardness of constituent phases, the nano indentation test was performed on the Fe-0.6B-0.8C and Fe-1Ni-0.6B-0.8C alloys. The hardness was calculated from the load-displacement curve using Oliver-Pharr method [40]. With Ni addition, the hardness of grain (pearlite) increased from 2.7 to 3.1 GPa and the hardness of grain boundary increased from 13.8 to 16.8 GPa, which can be attributed to the solid solution strengthening (Fig. 2.18). The load-elongation curves for Fe-B-C and Fe-Ni-B-C alloys are presented in Fig. 2.17(b). The tensile strength of specimen increased from 280~296 to 362~363 MPa with Ni addition, [35-37] which was due to the similar reasons for the improved bulk hardness. The elongation to failure increased from 2.2~3.0 to 3.6~4.4 %, which can be attributed to the increased apparent density. Especially, the elongation to failure was greatly improved with decreasing the B content in Fe-B-C and Fe-Ni-B-C alloys. It indicated that the decrease of the volume fraction of solidified phases was effective to increase the grain continuity and suppress the failure at the grain boundaries during tensile test [38,39]. As a result of composition variation, the elongation to failure reached 4.4 % in Fe-1Ni-0.4B-0.8C

alloy.

To further improve the elongation to failure, the quenching and post annealing was carried out in an aim to obtain the desired microstructure through the coarsening of solidified  $\alpha$ -Fe particles to the matrix grains. Fig. 2.19(a) and (b) present the optical and SEM micrographs of Fe-1Ni-0.4B-0.8C alloy after post annealing. The asymmetric quenching process led to the microstructural change of the grain boundaries into the well-dispersed alternated layers of hard phase and  $\alpha$ -Fe (Fig. 2.20) [45,46]. However, during post annealing, the embedded  $\alpha$ -Fe particles started to coarsen and merge into the grains (Fig. 2.21(a)) and the grain boundary was gradually changed from continuous boride network to discontinuous structure (Fig. 2.21(b)). After 24 h post annealing, the Fe-1Ni-0.4B-0.8C alloy exhibited a necklace microstructure such that the pearlite grains were linked with each other and hard phases were isolated at the grain boundaries. To investigate the constituent phases of post annealed Fe-1Ni-0.4B-0.8C alloy, the specimen which contained the grains and grain boundaries was prepared by FIB technique as shown in the low magnification TEM image (Fig. 2.19(c)). The selected area electron diffraction (SAED) pattern of the grain area (spot 1) was indexed to be  $\alpha$ -Fe with a  $[01\bar{2}]$  zone axis (Fig. 2.19(d)) and the hard phase area (spot 2) was indexed to be  $\text{Fe}_3\text{C}$  with a  $[1\bar{2}0]$  zone axis (Fig. 2.19(e)) [47]. Based on the microstructure and EDS analysis (Fig. 2.19), the grain and hard phase were identified to be pearlite and  $(\text{Fe}, \text{Ni})_3(\text{C}, \text{B})$ , respectively, which were identical to those before the heat treatment. Thus, a significant grain coarsening with an obvious necking was observed after post annealing without the transformation. Upon quenching and post annealing, the mechanical characteristics

(apparent density, bulk hardness and tensile strength) of post annealed Fe-1Ni-0.4B-0.8C alloy were mostly recovered to their initial values (Fig. 2.22) [43]. Especially, the elongation to failure dramatically increased from 2.8 to 5.2 % (Figure 2.23), which was even higher than the initial value (4.4 %). The increase of elongation to failure can be attributed to the increase of grain continuity after the post annealing. This results showed that the microstructure consisting of linked pearlite grains and isolated  $(\text{Fe, Ni})_3(\text{C, B})$  particles was to be highly resistant to failure, improving the elongation of failure in Fe-1Ni-0.4B-0.8C alloys.

## 2.4. Conclusions

In this study, Fe-Ni-B-C alloys were successfully fabricated by liquid phase sintering to achieve a high densification. Ni addition was employed to decrease the eutectic temperature and improve the densification and mechanical properties of Fe-B-C alloys. The Ni addition facilitated the diffusion of solidified  $\gamma$ -Fe during solidification, which lead to the improved densification and induced the microstructure change from pearlite/re-precipitated ferrite to pearlite. For the improvement of elongation property, the composition controlling and post annealing were performed to modify the microstructure. The decrease of B content decreased the volume fraction of hard phases, and the post annealing induced the discontinuous grain boundary structure composed of the isolated hard phases. A significant improvement on elongation was observed in Fe-Ni-B-C alloy. The increase of elongation to failure can be attributed to the optimized volume fraction of hard phase and the increase of grain continuity, which suppressed the continuous network of

eutectic phases. As a result of microstructure modification, the post annealed Fe-1Ni-0.4B-0.8C alloy resulted in the high elongation to failure of 5.2 %.

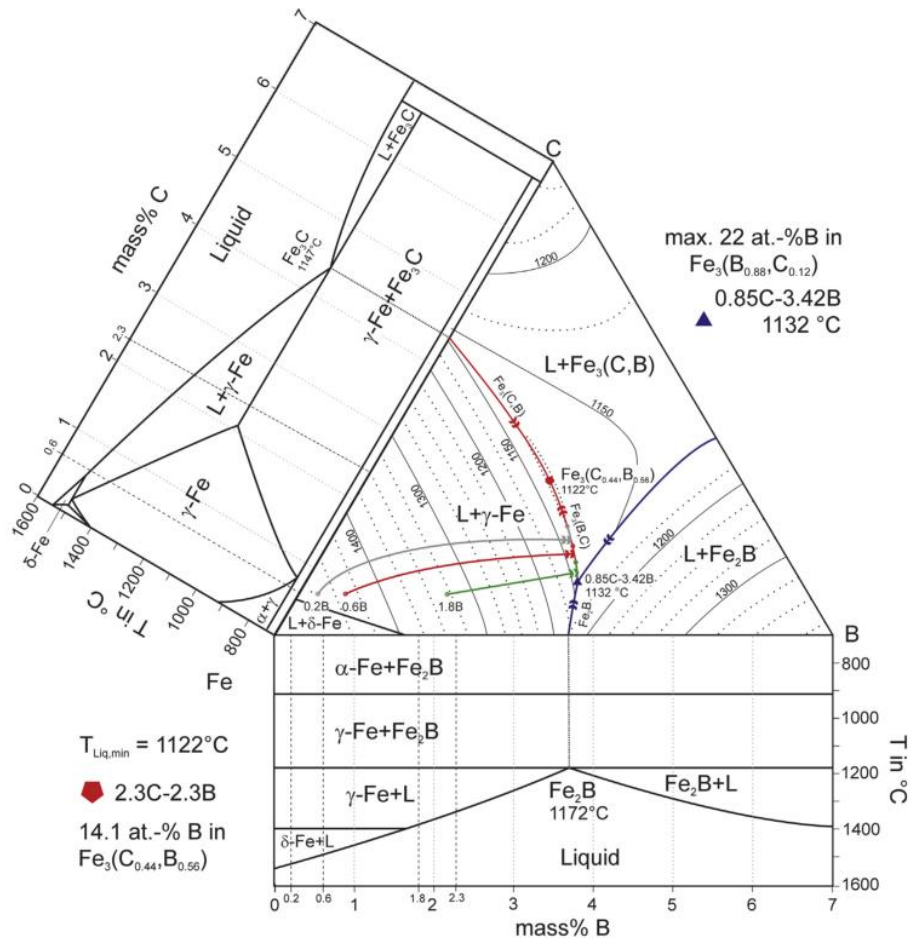
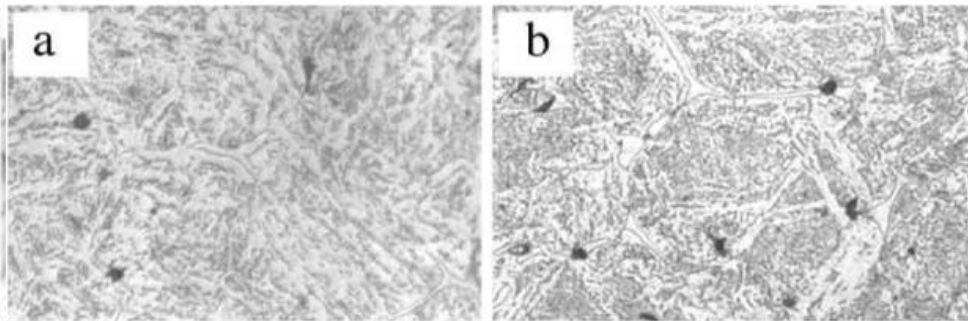


**Figure. 2.1.** Ternary projection of the liquidus surface including solidification paths of the analyzed alloys.



Carbon	Maximum shrinkage rate	Temperature for maximum shrinkage rate	Total shrinkage	Sintered density
(a) 0.2 wt%	$4.7 \times 10^{-5} \text{ s}^{-1}$	1136 °C	2.36 %	7.45 g/cm <sup>3</sup>
(b) 0.44 wt%	$9.9 \times 10^{-5} \text{ s}^{-1}$	1110 °C	3.18 %	7.58 g/cm <sup>3</sup>

### Lowering the temperature of eutectic reaction

**Figure. 2.2.** The effect of C addition on densification behavior of Fe-B alloys

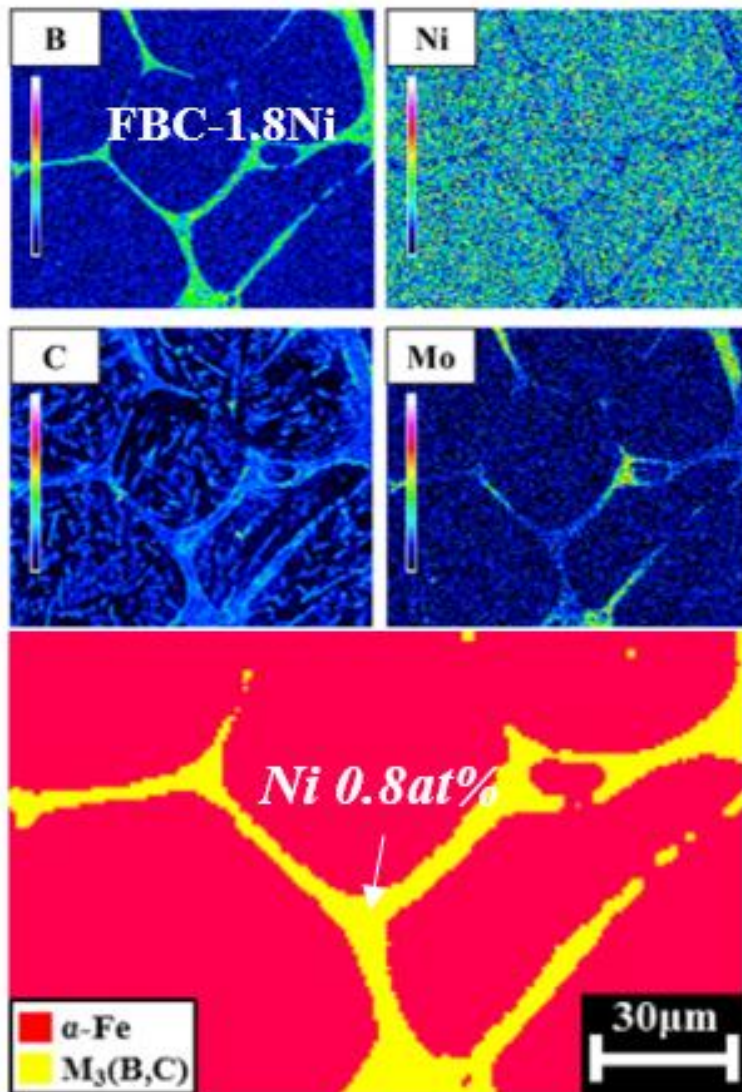


**Figure. 2.3.** The elemental mapping and phase identification of FeBC-Ni steel sintered at 1250 °C

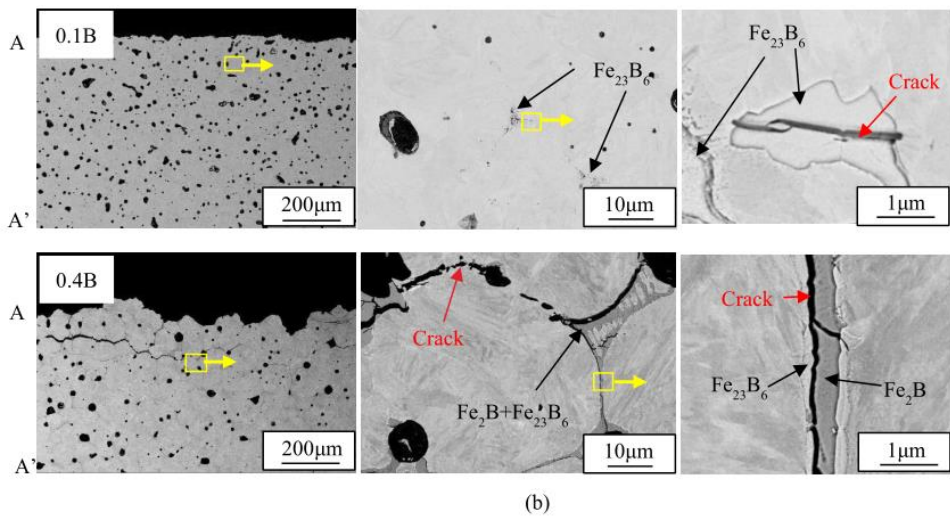


**Figure. 2.4.** Crack formation and propagation in Fe-B-C alloys

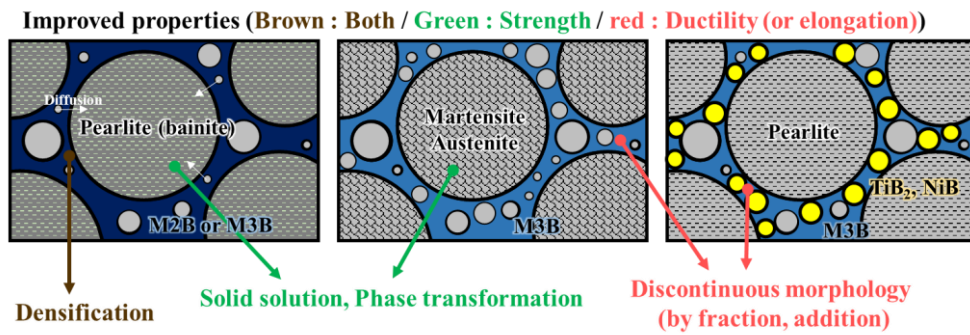


**Figure. 2.5.** Schematic diagram of the effect of microstructural modification in Fe-B-C based alloys

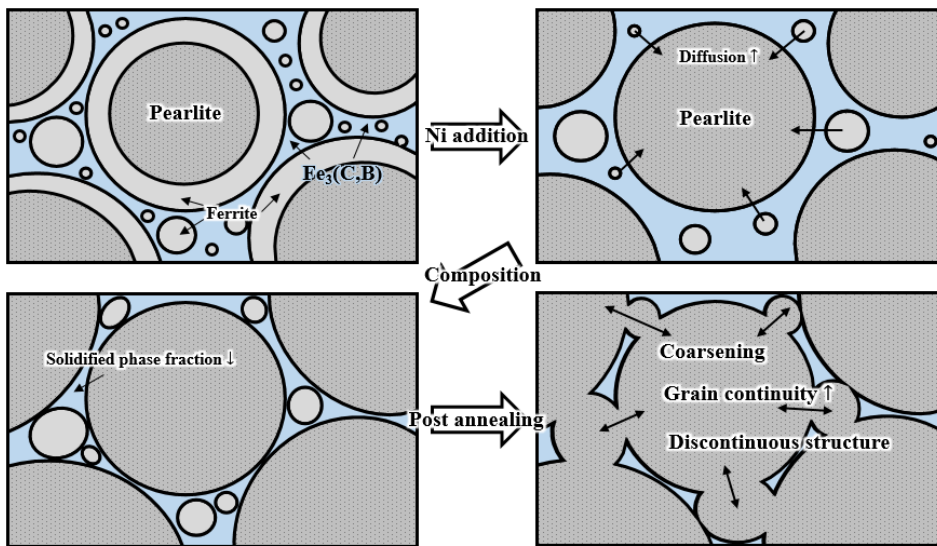


**Figure. 2.6.** Schematic diagram of the effect of Ni addition and post-annealing on microstructure of Fe-Ni-B-C alloys

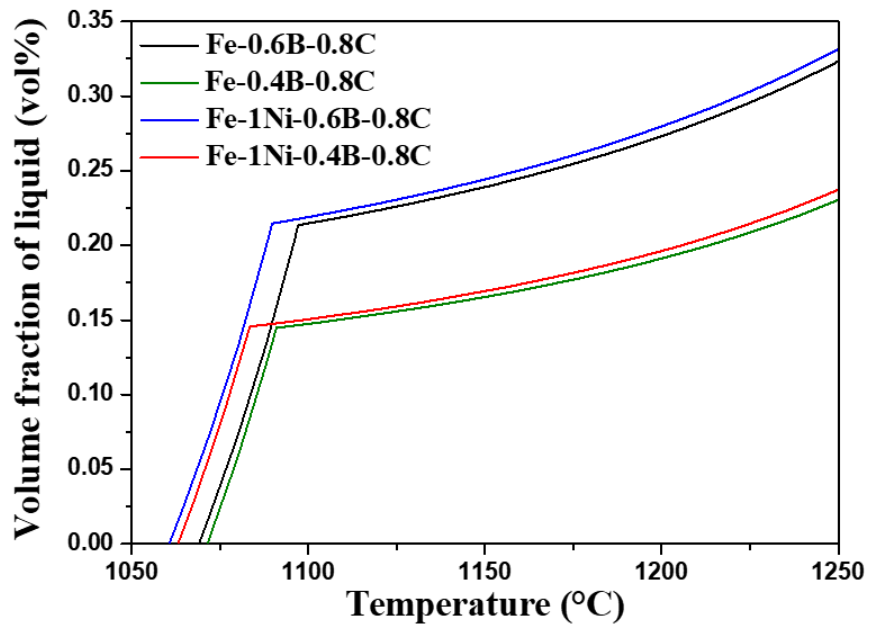


**Figure 2.7.** Volume fraction of liquid phase in Fe-0.6B-0.8C, Fe-0.4B-0.8C, Fe-1Ni-0.6B-0.8C, and Fe-1Ni-0.4B-0.8C alloys as a function of temperature.

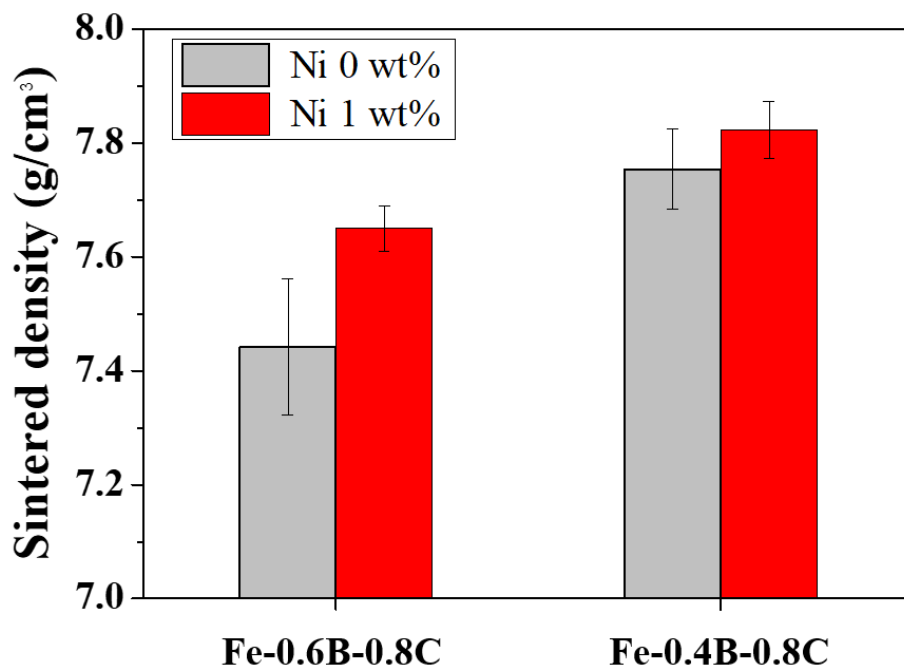


**Figure 2.8.** Apparent density of liquid phase sintered Fe-0.6B-0.8C, Fe-0.4B-0.8C, Fe-1Ni-0.6B-0.8C, and Fe-1Ni-0.4B-0.8C alloys.

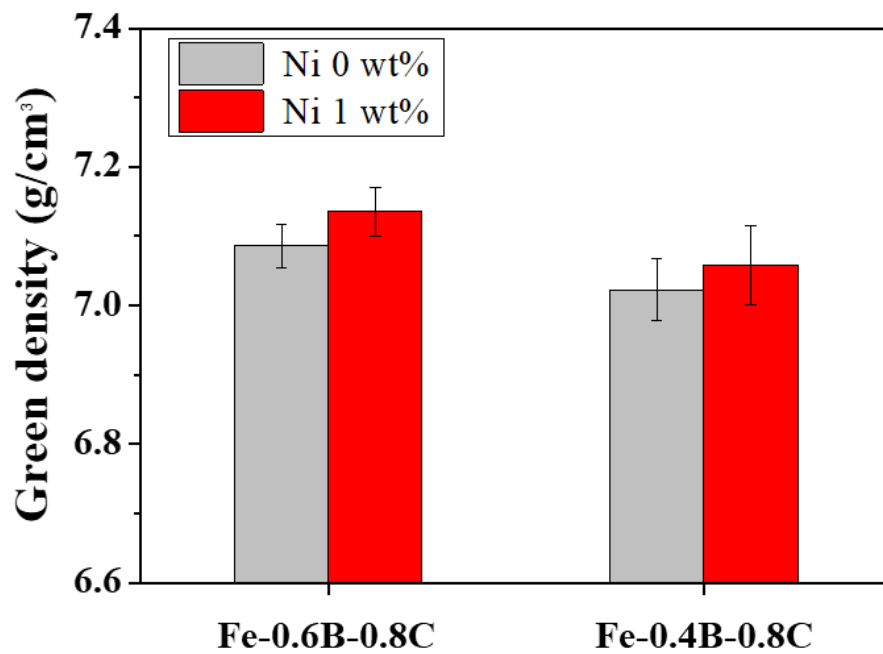


**Figure. 2.9** Green density of Fe-0.6B-0.8C, Fe-0.4B-0.8C, Fe-1Ni-0.6B-0.8C, and Fe-1Ni-0.4B-0.8C pellets prepared at a compacting pressure of 600 MPa.

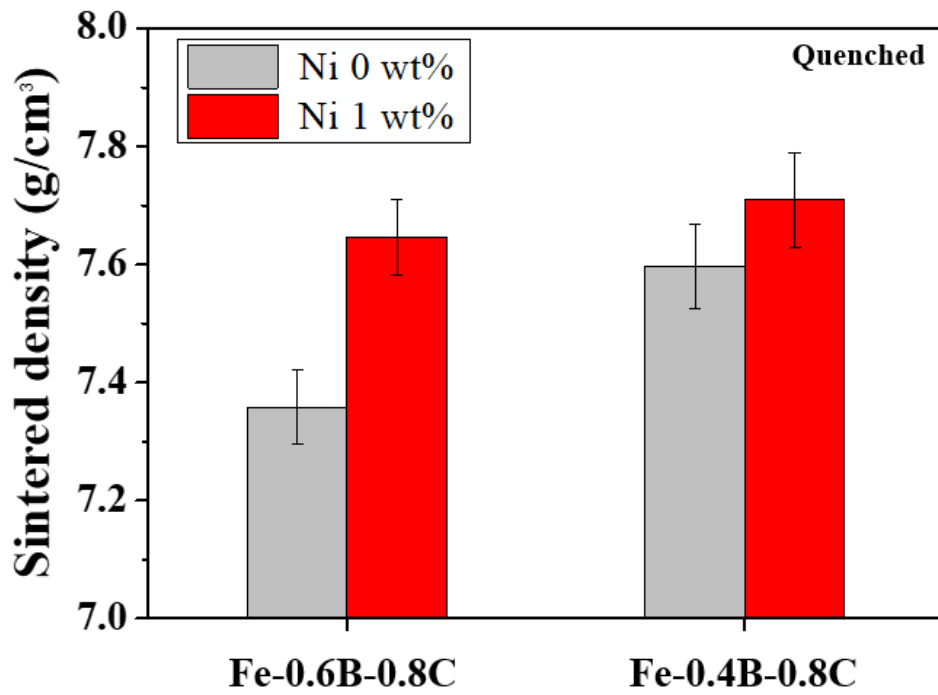


**Figure 2.10.** Apparent density of Fe-0.6B-0.8C, Fe-0.4B-0.8C, Fe-1Ni-0.6B-0.8C, and Fe-1Ni-0.4B-0.8C alloys quenched from 1180 °C.

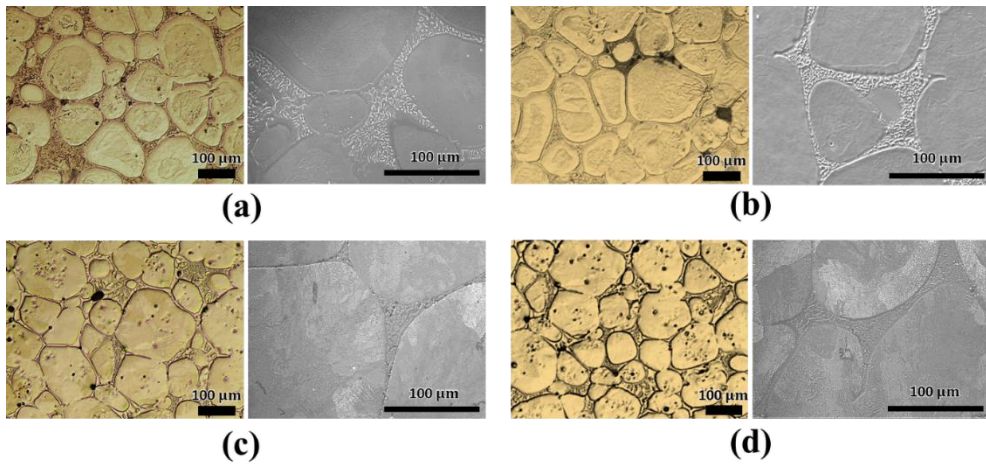
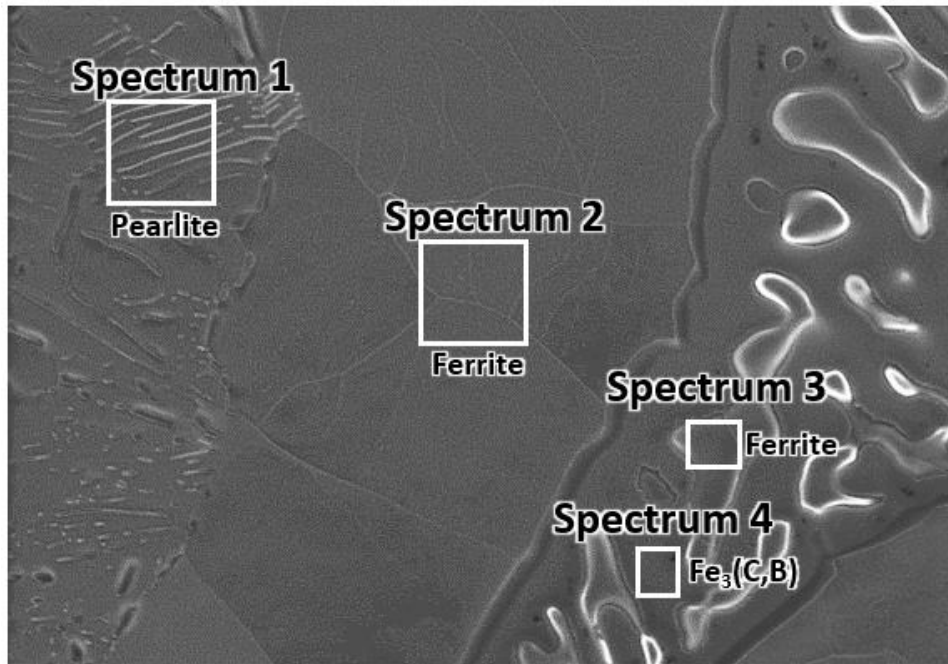


**Figure 2.11.** Optical and SEM micrographs of (a) Fe-0.6B-0.8C, (b) Fe-0.4B-0.8C, (c) Fe-1Ni-0.6B-0.8C, and (d) Fe-1Ni-0.4B-0.8C alloys



Chemical composition (wt%)				
	Fe	Ni	B	C
Spectrum 1	97.22	-	-	2.78
Spectrum 2	99.32	-	-	0.68
Spectrum 3	100	-	-	0
Spectrum 4	93.6	-	2.1	4.1

**Figure 2.12.** FE-SEM image of Fe-0.6B-0.8C alloy and chemical composition of selected areas by EDS measurements.

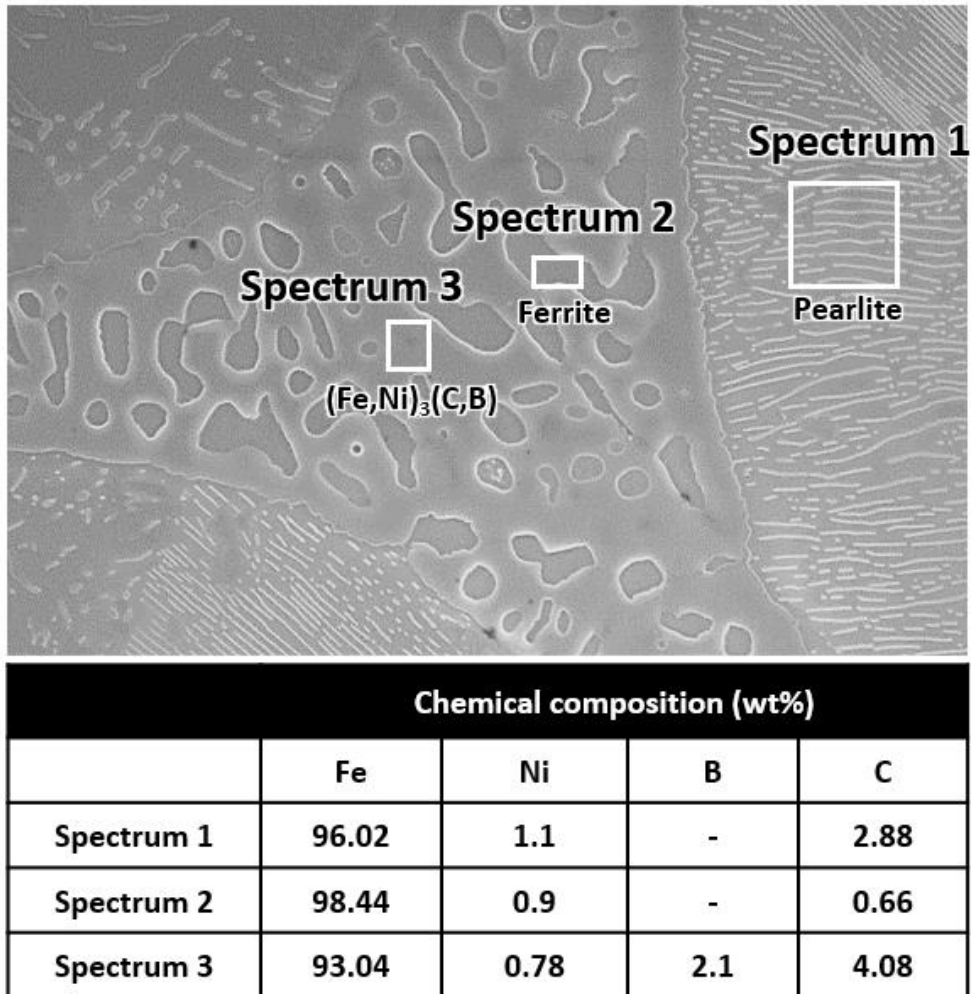


**Figure 2.13.** Apparent density of liquid phase sintered Fe-0.6B-0.8C, Fe-0.4B-0.8C, Fe-1Ni-0.6B-0.8C, and Fe-1Ni-0.4B-0.8C alloys.

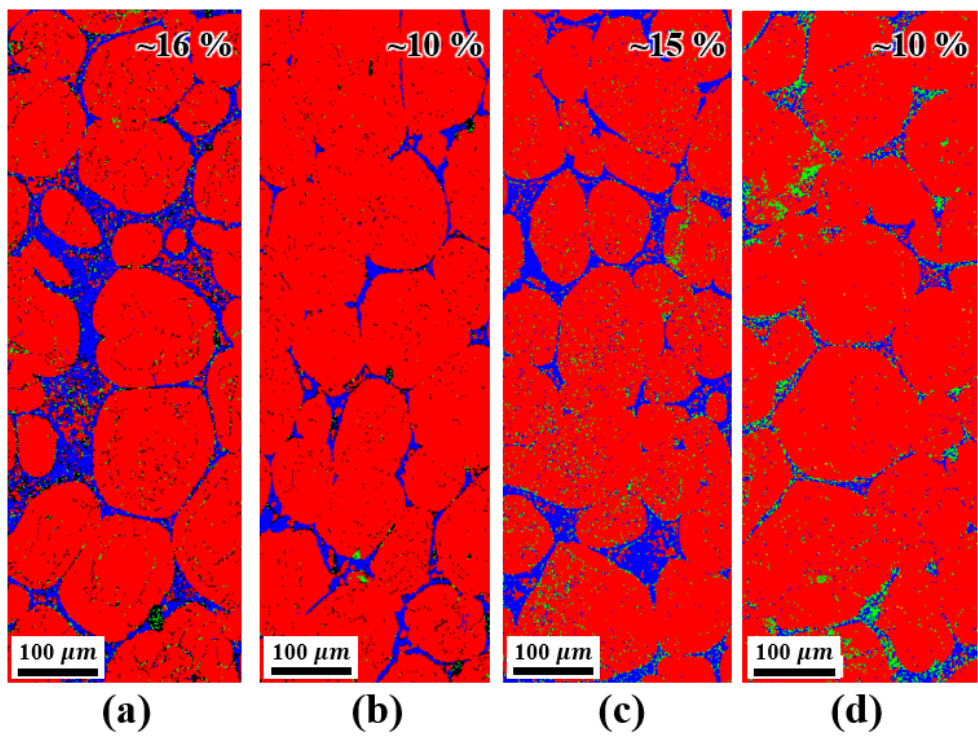


**Figure 2.14.** Phase identification and fraction determined by EBSD in (a) Fe-0.6B-0.8C, (b) Fe-0.4B-0.8C, (c) Fe-1Ni-0.6B-0.8C, and (d) Fe-1Ni-0.4B-0.8C alloys.

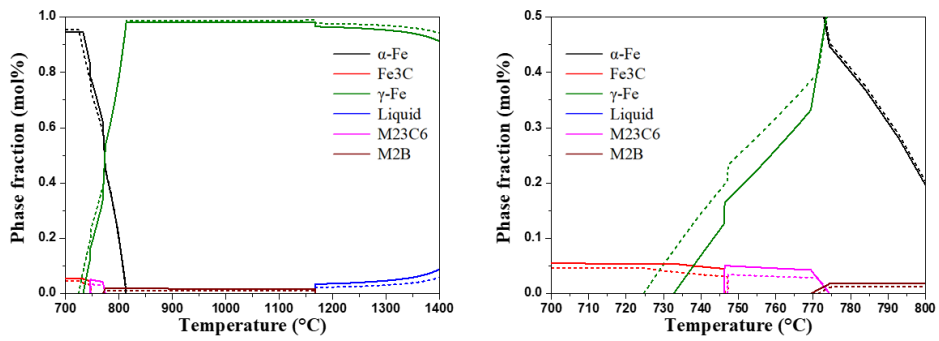


**Figure 2.15** Calculated phase changes during the solidification of Fe-0.6B-0.8C (dash line) and Fe-1Ni-0.6B-0.8C alloys (solid line) under the equilibrium condition.

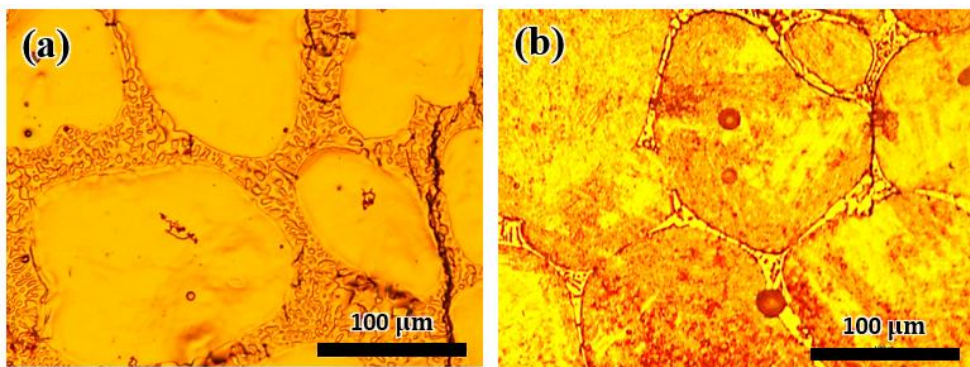


**Figure 2.16.** Optical micrographs of Fe-0.6B-0.8C and Fe-1Ni-0.6B-0.8C alloys quenched from 950 °C.

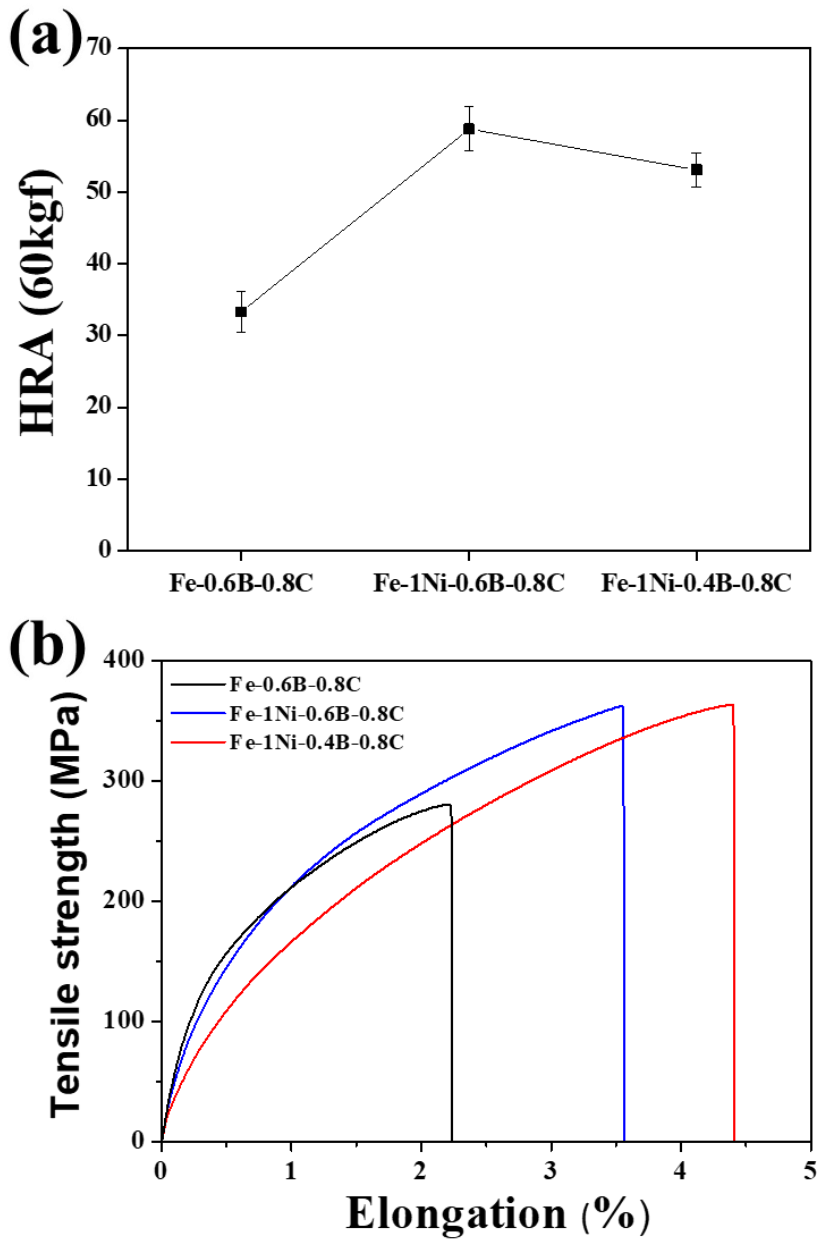


**Figure 2.17.** (a) Bulk hardness and (b) load-elongation curves of Fe-0.6B-0.8C, Fe-0.4B-0.8C, Fe-1Ni-0.6B-0.8C, and Fe-1Ni-0.4B-0.8C alloys.

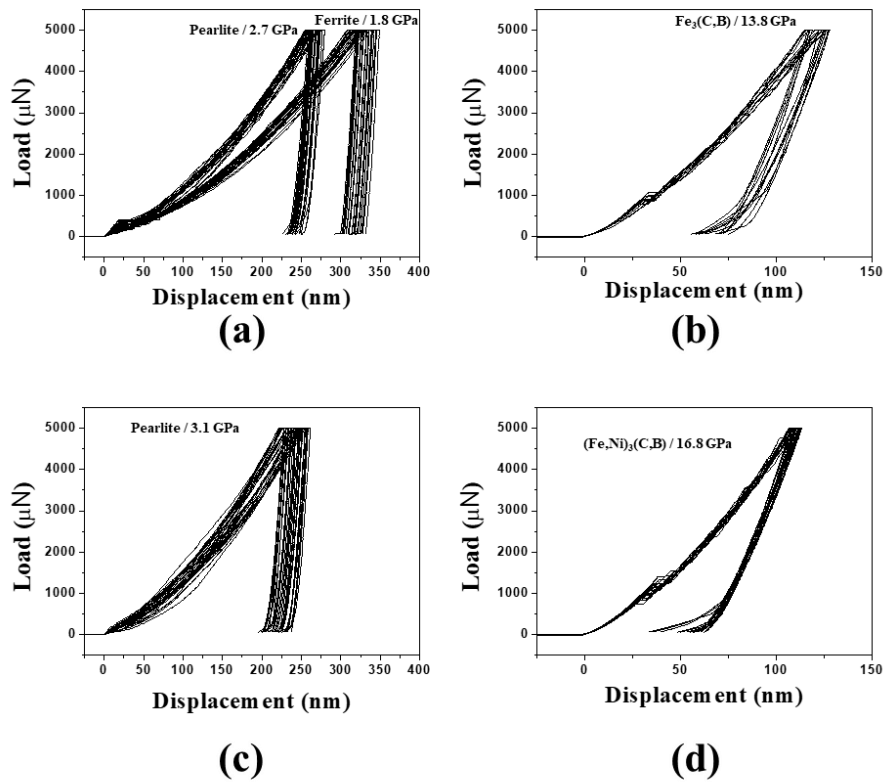


**Figure 2.18** Nanoindentation load-displacement curves of grain and grain boundary of (a, b) Fe-0.6B-0.8C and (c, d) Fe-1Ni-0.6B-0.8C alloys.

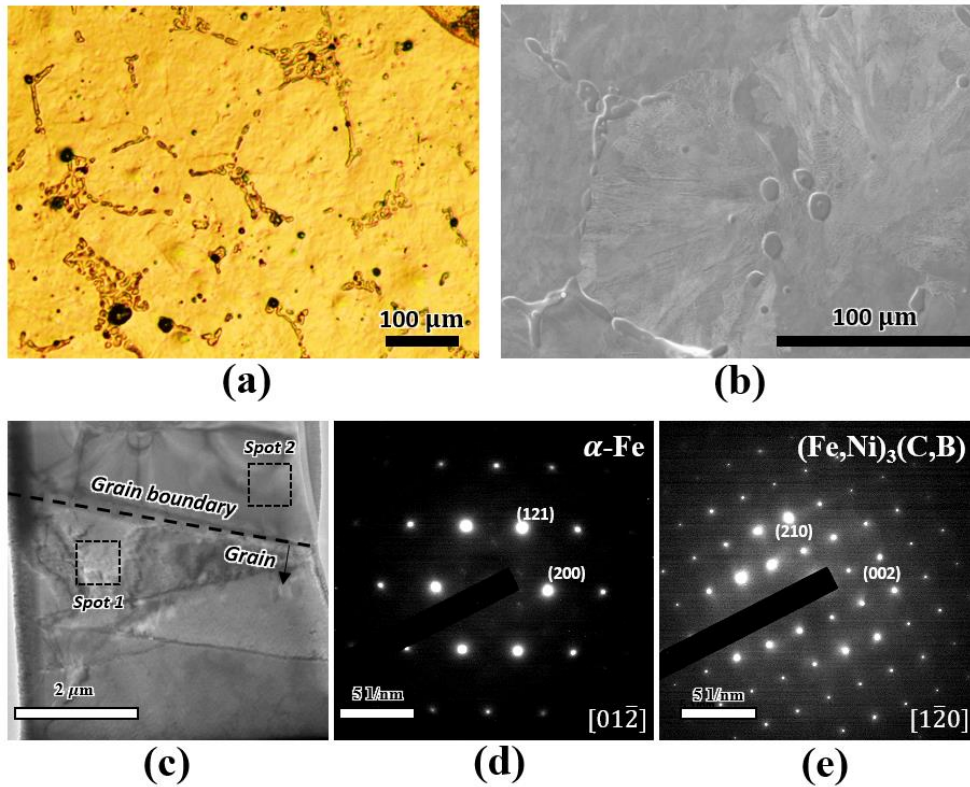


**Figure 2.19.** (a) Optical and (b) SEM micrographs of Fe-1Ni-0.4B-0.8C alloy post annealed at 1000 °C for 24 h, (c) low magnification HAADF-STEM image of grain and grain boundary in Fe-1Ni-0.4B-0.8C alloy and selected area diffraction patterns (SADPs) of (d) spot 1 ( $\alpha$ -Fe) and (e) spot 2 ( $(\text{Fe, Ni})_3(\text{C, B})$ ).

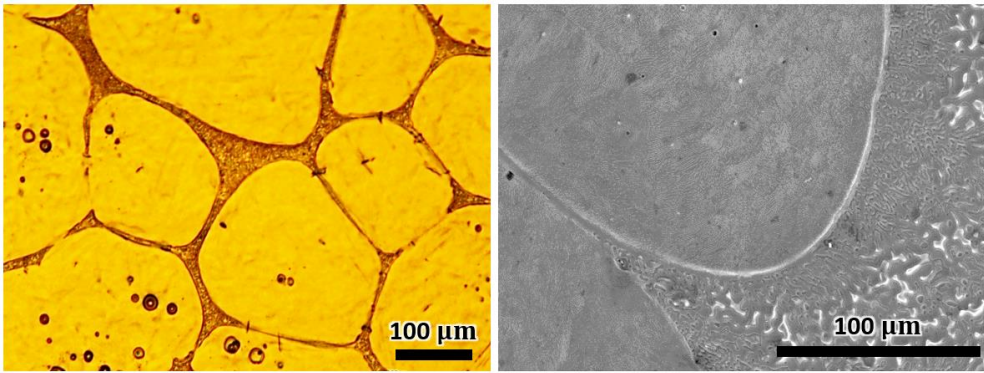


**Figure 2.20.** Optical and SEM micrographs of Fe-1Ni-0.6B-0.8C alloys quenched from 1180 °C.

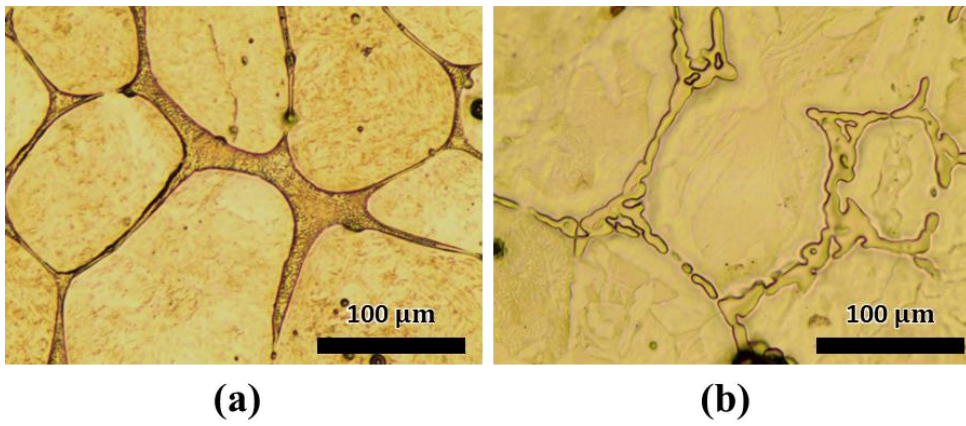


**Figure 2.21** Optical micrographs of Fe-1Ni-0.6B-0.8C alloys post annealed at 1000 °C for (a) 3h and (b) 12 h.

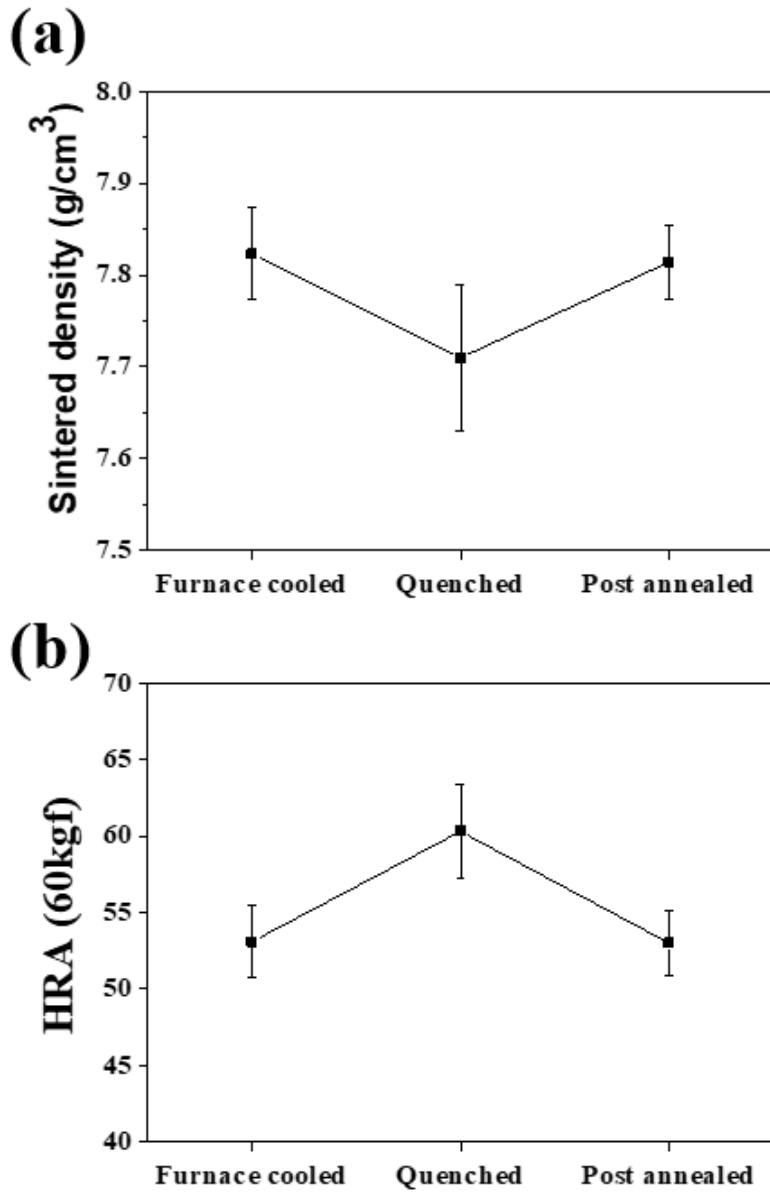
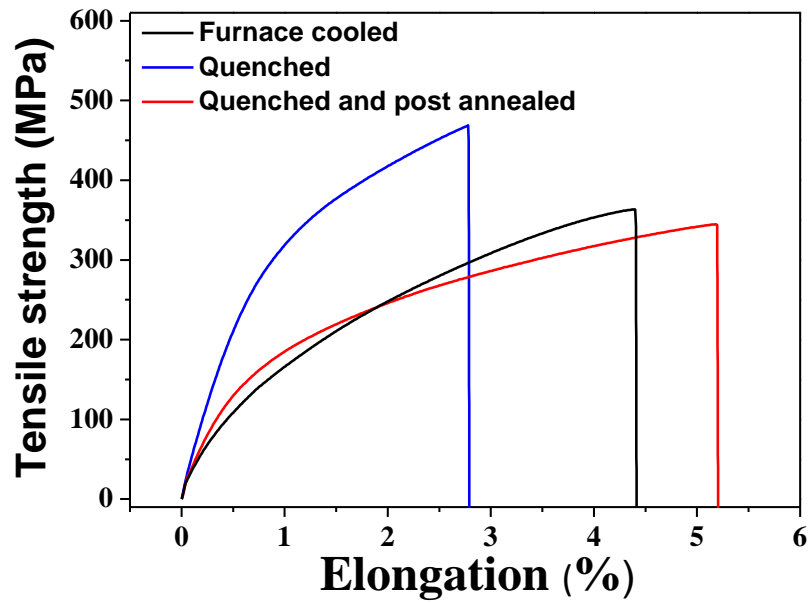


Figure 2.22. Apparent density of liquid phase sintered Fe-0.6B-0.8C, Fe-0.4B-0.8C, Fe-1Ni-0.6B-0.8C, and Fe-1Ni-0.4B-0.8C alloys.



**Figure 2.23.** load-elongation curves of furnace cooled, quenched, and post annealed Fe-1Ni-0.4B-0.8C alloys.

## Reference

- [1] K.S. Narasimhan: *Mater. Chem. Phys.*, 2001, vol. 67, pp. 56-65.
- [2] A. Hadrboletz, and B. Weiss: *Int. Mater. Rev.*, 1997, vol. 42, pp. 1-44.
- [3] B.A. James: *Powder Metall.*, 1985, vol. 28, pp. 121-30.
- [4] R.M. German, P. Suri and S. J. Park: *J. Mater. Sci.*, 2009, vol. 44, pp. 1-39.
- [5] J. Liu, A. Upadhyaya, and R.M. German: *Metall. Mater. Trans.A.*, 1999, vol. 30, pp. 2209-20.
- [6] H. Borgström, and L. Nyborg: *J. Iron Steel Res. Int.*, 2007, vol. 14, 70-76.
- [7] H. Preusse, and J.D. Bolton: *Powder Metall.*, 1999, vol. 42, pp. 51-62.
- [8] S.J. Jamil, and G.A. Chadwick: *Powder Metall.* 1985, vol. 28, pp. 65-71.
- [9] M. Marucci, A. Lawley, R. Causton, and S. Saritas: *Proc. Powder Metall. Congr. Exhib. Orlando, Florida, USA, 2002*, pp. 53-62.
- [10] Y.C. Peng, H.J. Jin, J.H. Liu, and G.L. Li: *Mater. Sci. Eng. A*, 2011, vol. 529, pp. 321-25.
- [11] H.O. Gulsoy, M.K. Bilici, Y. Bozkurt, and S. Salman: *Mater. Des.*, 2007, vol. 28, pp. 2255-59.
- [12] J. Lentz, A. Röttger, and W. Theisen: *Acta Mater.*, 2015, vol. 99, pp. 119-29.
- [13] C. Yang, F. Liu, G. Yang, Y. Chen, N. Liu, and Y. Zhou: *J. Alloys. Compd.*, 2007, vol. 441, pp. 101-06.

- [14] Y. Tomita: *Int. Mater. Rev.*, 2000, vol. 45, pp. 27-37.
- [15] H. Fayazfar, M. Salarian, A. Rogalsky, D. Sarker, P. Russo, V. Paserin, and E. Toyserkani: *Mater. Des.*, 2018, vol. 144, pp. 98-128.
- [16] Z. Xiu, A. Salwen, X. Qin, F. He, and X. Sun: *Powder Metall.*, 2003, vol. 46, pp. 171-74.
- [17] M.W. Wu, Y.C. Fan, H.Y. Huang, and W.Z. Cai: *Metall. Mater. Trans. A*, 2015, vol. 46, pp. 5285-95.
- [18] T.B. Sercombe: *Mater. Sci. Eng. A*, 2003, vol. 344, pp. 312-17.
- [19] M. Sarasola, T. Gómez-Acebo, and F. Castro: *Acta Mater.*, 2004, vol. 52, pp. 4614-22.
- [20] R. Annamalai, A. Upadhyaya, and D. Agrawal: *Bull. Mater. Sci.*, 2013, vol. 36, pp. 447-56.
- [21] F.L. Serafini, M. Peruzzo, I. Krindges, M.F.C. Ordoñez, D. Rodregues, R.M. Souza, and M.C.M. Farias: *Mater. Charact.*, 2019, vol. 152, pp. 253-64.
- [22] S. Ma, J. Xing, S. Guo, Y. Bai, H. Fu, P. Lyu, Z. Huang and W. Chen: *Mater. Chem. Phys.*, 2017, vol. 199, pp. 356-69.
- [23] M. Selecka, A. Salak, L. Parilak and H. Danninger: *Proceedings of 2000 PM World Congress, Kyoto, Japan, JPMA ED.*, 2000, Part.1, pp. 16-20.
- [24] T. Ogawa, and T. Koseki: *Weld. Res. Suppl.*, 1989, vol. 68, pp. 181-91.
- [25] M. Selecká, A. Šalák, and H. Danninger: *J. Mater. Process. Tech.*, 2003, vol. 143,

pp. 910-915.

- [26] X. Wei, Z. Chen, J. Zhong, L. Wang, W. Yang, and Y. Wang: *Comput. Mater. Sci.*, 2018, vol. 147, pp. 322-30.
- [27] M. Sarasola, S. Sainz, and F. Castro: *European PM Conference Proceedings*, 2005, vol. 1, pp. 349-56.
- [28] C. Tojal, T. Gómez-Acebo, and F. Castro: *Mater. Sci. Forum.*, 2007, vol. 534-536, pp. 661-64.
- [29] M. Skałoń, M. Hebda, K. Sulikowska, and J. Kazior: *Mater. Des.*, 2016, vol. 108, pp. 462-69.
- [30] M.V. Sundaram, K.B. Surreddi, E. Hryha, A. Veiga, S. Berg, F. Castro, and L. Nyborg: *Metall. Mater. Trans. A*, vol. 49, pp. 255-63.
- [31] M.W. Wu, W.Z. Cai, Z. Lin, and S. Chang: *Mater. Des.*, 2017, vol. 133, pp. 536-48.
- [32] M.W. Wu and W.Z. Cai: *Mater. Charact.*, 2016, vol. 113, pp. 90-97.
- [33] S. Egashira, T. Sekiya, T. Ueno and M. Fujii: *Jpn. Soc. Mech. Eng.*, 2019, vol. 6, pp. 1-11.
- [34] B.H. Rabin and R.M. German: *Metall. Trans. A*, 1988, vol. 19, pp. 1523-32.
- [35] H.I. Bakan, D. Heaney and R. M. German: *Powder Metall.*, 2001, vol. 44, pp. 235-42.
- [36] Z. Liu, X. Chen, Y. Li and K. Hu: *J. Iron. Steel. Res. Int.*, 2009, vol. 16, pp. 37-

42.

[37] H. Fu, Q. Xiao, J. Kuang, and J. Xing: *Mater. Sci. Eng. A*, 2017, vol. 466, pp. 160-65.

[38] F. Li and Z. Li: *J. Alloys. Compd.*, 2014, vol. 587, pp. 267-72.

[39] J.O. Andersson, T. Helander, L. Hoglund, P. Shi and B. Sundman: *CALPHAD*, 2002, vol. 26, pp. 273-312.

[40] Y. Yi, Q. Li, J. Xing, H. Fu, D. Yi, Y. Liu and B. Zheng: *Mater. Sci. Eng. A.*, 2019, vol. 754, pp. 129-39.

[41] N. Tosangthum, P. Kunnam, M. Morakotjinda, W. Koetnuyom, R. Krataitong, P. Wila and R. Tongsri: *Key Eng. Mater.*, 2019, vol. 798, pp. 9-16.

[42] J. Karwan-Baczewska: *Arch. Metall. Mater.*, 2011, vol. 56, pp. 789-96.

[43] W. Koetnuyom, P. Chantawet, N. Tosangthum, M. Morakotjinda, T. Yotkaew, P. Wila, and R. Tongsri: *J. Met. Mater. Miner.*, 2019, vol. 29, pp. 22-30.

[44] R.M. German and K.A. D'Angelo: *Int. Met. Rev.*, 1984, vol. 29 (4), pp. 229-272.

[45] P. Sang, H. Fu, Y. Qu, C. Wang and Y. Lei: *Werkstofftech.*, 2015, vol. 46, pp. 962-69.

[46] X. Ren, H. Fu, J. Xing, Y. Yang, and S. Tang: *J. Mater. Res.*, 2017, vol. 32, pp. 3078-88.

[47] Y. Penghui, F. Hanguang, L. Guolu, L. Jinhai, and Z. Xuebo: *Mater. Des.*, 2020,

vol. 186, pp. 108363.

[48] M.A. Taha, A.F. Yousef, K.A. Gany, and H.A. Sabour: Mat.-wiss. u. Werkstofftech., 2012, vol. 43, pp. 913-23.

# **Chapter 3. Effect of Molybdenum Addition on the Microstructure and Mechanical Properties of Fe-Mo-B-C Sintered Alloys**

## **3.1. Introduction**

Powder metallurgy (P/M) is a metal consolidation technique to produce the near net shape components and has been widely applied to automobile, home appliances, and electronic devices due to its high productivity and low cost [1]. However, the P/M applications are very limited due to the poor mechanical properties, in particular, low ductility, resulting from the presence of porosity ranging from 5 to 15 vol. % [2]. Liquid phase sintering (LPS) is an attractive method to achieve a nearly full densification via particle rearrangement, solution-re-precipitation, and solid-state sintering [3,4]. Among the various LPS systems [5-7], Fe-B-C system has received a great attention because of its hardenability, sinterability, cost effectiveness, and mechanical properties [1,8-11]. Boron (B) forms a liquid phase at low temperature through the eutectic reaction  $\gamma\text{-Fe} + \text{Fe}_2\text{B} \rightarrow \text{L}$  even with a small addition, wetting the grain boundaries and filling the pores [1,8-12]. Carbon (C) is primarily used to improve the mechanical properties of Fe-based alloys through the formation of cementite and pearlite [13,14] and also promotes the liquid generation by lowering the temperature of eutectic reaction [12,15,16]. However, the brittle eutectic phases

( $\text{Fe}_3(\text{C},\text{B})$  and  $\text{Fe}_2\text{B}$ ) are formed along the grain boundary during solidification, which is detrimental to the mechanical properties [17,18]. Several attempts have been explored to increase the ductility of Fe-B-C based alloys including composition [8-10,14,19,20], heat treatment [21-23], and modification [24-26]. However, the improvement of ductility was very limited due to the presence of continuous network of brittle eutectic solidified phases along the grain boundary. In addition, the first principle calculations using density functional theory (DFT) indicated that the alloying elements (Ti, V, Cr, Co, Ni, and Cu) can enhance the ductility of the  $\text{Fe}_2\text{B}$ , but cannot change the intrinsic brittle nature of the  $\text{Fe}_2\text{B}$  [27]. On the other hand, the nickel boride (NiB) addition to 316L stainless steel produced a discontinuous boride phase at the grain boundary resulting from the localized increase in nickel concentration, which improved the tensile strength and elongation properties (Fig. 3.1) [28]. The above results suggested that the ductility of Fe-B-C based alloys can be enhanced by adding the appropriate alloying elements, which can form the discontinuous grain boundary with the alternating solidified phases.

Molybdenum (Mo) is an important alloying element for PM alloy steels due to its high hardenability, low oxygen affinity, and solid solution strengthening [29-31]. Xiu et al. reported that the addition of Mo into Fe-B-C system led to the ternary reaction to form another liquid phase with  $\text{Fe}_3\text{C}$  and  $\text{Mo}_2\text{C}$  [32]. Sarasola et al. found that the liquid formation was strongly dependent on the Mo content and the Mo-rich  $(\text{Fe},\text{Mo})_2\text{B}$  precipitates formed at 3.5 wt% Mo suppressed the liquid formation at the temperature of the eutectic reaction between Fe and  $\text{Fe}_2\text{B}$  [33-35]. Wu et al. showed that two separate liquid formation reactions occurred at different temperatures in Fe-Mo-B-C system, but the grain boundary was composed of a continuous network of

M2B or M3B, possibly due to the low concentration of Mo (0.5~1.5 wt%) [36-40]. Above studies which contain Mo addition to the Fe-B-C alloys were summarized in Fig. 3.2. It is speculated that in Fe-Mo-B-C system with high Mo content, two solidification reactions with different solidus temperatures sequentially occur during cooling, which results in the grain boundary with alternating two eutectic solidified phases and suppresses the crack propagation. The schematic microstructure of Fe-Mo-B-C alloys are present in Fig. 3.3. However, the microstructure development in Fe-Mo-B-C with high Mo content (>3.5 wt%) has not been examined. In addition, the effects of microstructure and constituent phases on the mechanical properties of Fe-Mo-B-C alloy have not been thoroughly investigated.

In this study, Mo addition was employed to improve the ductility of Fe-B-C sintered alloys by modifying the grain boundary microstructure. For this, the amount of Mo addition was varied from 1.0 to 5.0 wt%. Then, the microstructure and mechanical properties of Fe-Mo-B-C alloys were comparatively investigated. Indeed, the grain boundary with a lamella structure was realized at high Mo content, and the constituent phases of lamella structure were analyzed by atomic resolution HAADF-STEM, SAED, EDS, and DFT calculation. As a result, a significant improvement of the tensile strength and ductility (elongation to failure) was achieved.

## **3.2. Experimental**

Commercially available Fe (ASC100.29, Hoganas), Mo (Sigma Aldrich), B (iNexus, Inc.), and C (Sigma Aldrich) were used as starting materials for synthesizing the

liquid phase sintered Fe-Mo-B-C alloys. The content of B and C was fixed to be 0.4 and 0.8 wt%, respectively and the amount of Mo was varied from 1.0 to 5.0 wt%. The starting powders were well mixed by hand or V-mixer and compacted into  $\varnothing 10$  mm pellets with a compacting pressure of 600 MPa. The sintering was carried out at 1280 °C for 3 h in a vacuum ( $10^{-2}\sim 10^{-3}$  torr). The density of sintered specimens was measured by Archimedes immersion method. The surface of sintered samples was prepared by standard metallographic technique and the microstructure was observed by optical microscopy (OM, Nikon L-150) and scanning electron microscope (FE-SEM, SU-70) equipped with energy dispersive X-ray spectroscopy (EDS). The grain boundary was examined by transmission electron microscopy (TEM, JEM-2100F and ARM-200F) and the TEM specimen was prepared by focused ion beam (FIB, Helios Nano Lab450, FEI) technique. The atomic structure was proposed by density functional theory (DFT) calculation using the Vienna Ab Initio Simulation Package (VASP). The hardness of Fe-Mo-B-C alloys was measured using Rockwell A hardness (Mitutoyo, Japan) and Vickers hardness measurement (HM-122, Mitutoyo, Japan) on the polished surface and the nanoindentation was also performed by Hysitron TriboLab 750 Ubi nano-indentation system equipped with a Berkovich indenter. The tensile specimens were prepared as per MPIF standard 10 and the testing was performed using a universal testing machine (Instron 5584) with a strain rate of 1.86 mm/min.

### **3.3. Results and discussion**

The quasi-binary phase diagram of the Fe-Mo-0.4B-0.8C system was calculated with Thermo-Calc [41] using a TCFE 2000 thermodynamic database. The Mo addition to Fe-B-C system increases the liquidus temperature from 1090 to 1180 °C (5.0 wt% Mo) and delays the liquid phase formation (Fig. 3.4 and Fig. 3.7). Integrating the results of previous researches and thermodynamic calculations, all specimens were sintered at 1280 °C (well above the solidus temperature) and thus, the continuous liquid with good wetting characteristics was formed in all the compositions investigated, which led to a nearly full densification (98.6~99.3 % of relative density) without the noticeable pores (Fig. 3.5). The apparent density increased with Mo addition ( $\rho_{\text{Fe}}=7.874$  vs.  $\rho_{\text{Mo}}=10.2$  g/cm<sup>3</sup>), but it slightly decreased after 3 wt%, which can be attributed to the different grain boundary (solidified) phases at high Mo content. In addition, the fraction of liquid phase was varied with Mo addition as shown in Fig. 3.9.

The optical and SEM micrographs of sintered Fe-Mo-B-C alloys are shown in Fig. 3.6 and Fig. 3.8, respectively. The Fe-0.4B-0.8C alloy exhibited the typical liquid phase sintered microstructure composed of spherical grains (pearlite and re-precipitated ferrite) and  $\alpha$ -Fe particle embedded continuous network of solidified phase (Fe<sub>3</sub>(C,B)) (Fig. 3.6(a) and Fig. 3.8(a)) [14]. The high magnification SEM image and EDS analysis (Fe, B, and C) clearly demonstrated the detailed microstructure and element distribution in the liquid phase sintered Fe-0.4B-0.8C alloy (Fig. 3.9). With the addition of Mo, re-precipitated ferrite and  $\alpha$ -Fe particles gradually disappeared from grains and grain boundaries, respectively, and the Fe-Mo-B-C alloys had the microstructures consisting of pearlite (or pearlite/bainite)

grains and  $(\text{Fe},\text{Mo})_3(\text{C},\text{B})$  grain boundaries (Fig. 3.6 (b), (c) and Fig. 3.8(b), (c)). The solubility limit of Mo into  $\gamma\text{-Fe}$  was  $\sim 3.0$  wt% at  $1280$  °C [42], but most of Mo was present at the grain boundary resulting in  $(\text{Fe},\text{Mo})_3(\text{C},\text{B})$  grain boundary (Fig. 3.10(a), (b)). Above 3 wt% Mo addition, the matrix grains maintained the pearlite (or pearlite/bainite) structure, but the grain boundary gradually changed from continuous network into lamellar structure (Fig. 3.11). At 5 wt% Mo addition, the grain boundary completely changed into lamellar structure of alternating solidified phase (Fig. 3.6(d) and Fig. 3.8(d)) [33-35]. The EDS mapping indicated that the lamellar structure was composed of alternating Mo-rich and Fe-rich phases (Fig. 3.8(e) and Fig. 3.10(c)). To investigate the microstructural change of matrix grains with Mo addition, the Fe-0.4B-0.8C and Fe-5Mo-0.4B-0.8C alloys were quenched from  $950$  °C (below the solidus temperature). A large number of  $\gamma\text{-Fe}$  particles were observed at the grain boundaries in Fe-0.4B-0.8C alloy (Fig. 3.12(a)). However, most of  $\gamma\text{-Fe}$  particles were diffused into the matrix grains in Fe-5Mo-0.4B-0.8C alloy (Fig. 3.12(b)). It implied that Mo addition facilitated the diffusion of solidified  $\gamma\text{-Fe}$  particles into matrix grains during solidification and thus, the re-precipitated ferrite disappeared from the grains after cooling resulting in the microstructural change from pearlite/re-precipitated ferrite to pearlite (or pearlite/bainite).

To further investigate the grain boundary of Fe-5Mo-0.4B-0.8C alloy, the cross sectional specimen was prepared by focused ion beam (FIB) technique and observed by TEM. The low magnification high angle annular dark field (HAADF)-scanning TEM (STEM) image showed that the grain boundary was composed of white colored single crystal-like layer of  $\sim 700$  nm thick and dark-colored polycrystalline layer of  $\sim 2$   $\mu\text{m}$  thick (Fig. 3.13(a)). The EDS mapping indicated that the white colored layer

was Mo, C, and B-rich and the dark colored layer was Fe-rich (Fig. 3.14). The selected area electron diffraction (SAED) pattern of dark colored layer (spot 1) was indexed to be  $\text{Fe}_3\text{C}$  with a  $[11\bar{1}3]$  zone axis (Fig. 3.13(b)) [43]. Combined with the EDS results, the dark colored layer was identified to be  $(\text{Fe},\text{Mo})_3(\text{C},\text{B})$ . On the contrary, the SAED pattern of white colored layer (spot 2) could not be indexed based on the reported crystallographic data, which contain Fe, Mo, B, and C (Fig. 3.13(c)). Instead, the atomic resolution HAADF-STEM image of white colored layer was obtained by Cs-corrected STEM, in which the dumbbells consisting of two outer bright dots and two inner less-bright dots are arranged in a herringbone pattern (Fig. 3.13(d)). The observed atomic structure was similar to that of WCoB (space group, Pnma) viewed along the  $[010]$  direction (Fig. 3.15) where bright dot and less-bright dots correspond to W and Co, respectively and B has no contrast [44,45]. Using WCoB-type structure, experimentally obtained d-spacing (Fig. 3.13(c)), and EDS results (Fig. 3.10), the new atomic structural model of  $\text{MoFe}(\text{C},\text{B})$  stabilized by relaxation of DFT calculation was proposed (Fig. 3.16). The simulated diffraction patterns of  $\text{MoFe}(\text{C},\text{B})$  by JEMS 4 were very similar irrespective of B and C content, and the simulated pattern of  $\text{MoFe}(\text{C}_{0.75},\text{B}_{0.25})$  was well matched with the experimental diffraction pattern after considering the B and C content by EDS (Fig. 3.13(c) and Fig. 3.15). The proposed  $\text{MoFe}(\text{C},\text{B})$  atomic structure model was superimposed on the HAADF-STEM image marked by white colored box (Fig. 3.15(d)). Consequently, the grain boundary of Fe-5Mo-0.4B-0.8C alloy was composed of alternating  $(\text{Fe},\text{Mo})_3(\text{C},\text{B})$  and  $\text{MoFe}(\text{C},\text{B})$  phases.

To examine the microstructure development of lamellar grain boundary in Fe-

5Mo-0.4B-0.8C alloy, the quenching experiment was carried out, which consisted of keeping the sintered specimen at the desired temperature immediately followed by a water quenching. Fig. 3.17(a) shows the SEM micrograph and EDS elemental mapping of Fe-5Mo-0.4B-0.8C alloy quenched from 1180 °C (below the liquidus temperature). The white colored solidified phase was nucleated around the grains ( $\gamma$ -Fe) and grew toward the liquid phase located at the center of the grain boundary, and the reprecipitated  $\gamma$ -Fe (white arrow) was observed around the grains. The EDS mapping indicated that the solidified phase was Mo, C, and B-rich. Based on the simulated phase diagram, the first solidification reaction ( $L$  (high C)  $\rightarrow \gamma$ -Fe + M2B (Mo-rich)) occurred and the first formed M2B was possibly close to  $Mo_2B$  [36,37]. From this period, the reprecipitated  $\gamma$ -Fe formed from the liquid phase was coalesced into the  $\gamma$ -Fe grain before the phase transformation to pearlite (or pearlite/bainite) [14,33-35]. For this reason, the reprecipitated ferrite phase was hardly observed after sintering of Fe-5Mo-0.4B-0.8C alloy (Fig. 3.10(d)). When the sintered specimen was quenched at 1080 °C (below the solidus temperature), the second solidification reaction ( $L$  (low C)  $\rightarrow \gamma$ -Fe + M2B (Fe-rich)) occurred and the grain boundary became the alternating microstructure of Mo and B-rich and Fe-rich solidified phases (Fig. 3.17(b)). Upon the subsequent cooling, phase transformation and diffusion occurred resulting in pearlite (or pearlite/bainite) grain ( $\gamma$ -Fe  $\rightarrow \alpha$ -Fe +  $Fe_3C$ ) and lamellar grain boundary composing of  $MoFe(C,B)$  and  $(Fe,Mo)_3(C,B)$ . Consequently, two solidification reactions with different solidus temperatures in Fe-Mo-B-C system resulted in the grain boundary with alternating two solidified phases. Based on the quenching experiment, the microstructure development of Fe-5Mo-0.4B-0.8C alloy during solidification was schematically depicted in Fig. 3.18.

To investigate the effects of Mo addition on the mechanical properties of Fe-B-C alloys, hardness and tensile tests were performed on the sintered specimens. The bulk hardness of Fe-B-C alloy was 33, but it increased to 60 at 1.0 wt% Mo addition and then, gradually increased with further Mo addition (Fig. 3.19) [46,47]. The bulk hardness of the alloys depends on the matrix (grain) and thus, the increase of hardness can be attributed to the microstructure change of grains from pearlite and re-precipitated ferrite to pearlite (or pearlite/bainite) with Mo addition (Fig. 3.6 and Fig. 3.8). The hardness of constituent phases (grain and grain boundary) in sintered specimens was measured by nano-indentation, and the hardness was calculated from the load-displacement curve using Oliver-Pharr method (Fig. 3.20 and Fig. 3.21) [48]. For reliability, more than 10 measurements were conducted at 10  $\mu\text{m}$  interval. The hardness of grain increased with increasing Mo content from 3.1 to 5.4~5.7 GPa (Fig. 3.21(a)) [49]. The increased hardness can be attributed to microstructural change from pearlite and re-precipitated ferrite to pearlite (or pearlite/bainite) and solid solution hardening with Mo addition [50]. It is known that Mo in steels delays the pearlite transformation reaction and increases the bainite formation [51]. The hardness of  $\text{Fe}_3(\text{C},\text{B})$  was 13.7 GPa in Fe-0.4B-0.8C alloy [52] and the hardness of the  $(\text{Fe},\text{Mo})_3(\text{C},\text{B})$  solidified phase slightly increased with increasing Mo content (Fig. 3.21(b)). Another solidified phase  $\text{MoFe}(\text{C},\text{B})$  formed at the grain boundary of Fe-5Mo-0.4B-0.8C alloy exhibited much higher hardness than  $(\text{Fe},\text{Mo})_3(\text{C},\text{B})$  (23.9~24.3 vs. 16.5 GPa). The SEM micrograph and EDS mapping images of Fe-5Mo-0.4B-0.8C alloy showed that the size of indentation decreased in the order of grain,  $(\text{Fe},\text{Mo})_3(\text{C},\text{B})$ , and  $\text{MoFe}(\text{C},\text{B})$ , which was well corresponded with the load-displacement curves (Fig. 3.20).

Fig. 3.22 shows the typical load-elongation curves of Fe-Mo-B-C alloys as a function of Mo content. The Fe-0.4B-0.8C alloy exhibited a tensile strength of 239 MPa and an elongation to failure close to 4.0% [53]. As expected, the tensile strength increased with Mo addition and reached 674 MPa at 5 wt% Mo addition [1,5,8,17,40,54,55]. The tensile strength mainly relies on the sintered density, but all the specimens in this study had the nearly full densification with the similar grain size and thus, the improved tensile strength with Mo addition can be attributed to the microstructural change of grain from pearlite and re-precipitated ferrite to pearlite (or pearlite/bainite) and of grain boundary from continuous network into lamellar structure and solid solution strengthening with Mo addition. On the other hand, the elongation to failure initially decreased to 2.2% (1 wt%) and it increased after 3 wt% Mo addition and reached 4.92% at 5 wt% Mo addition.

Fig. 3.23 represents the longitudinal cross-sectional SEM images of Fe-Mo-B-C alloys after the tensile test. All the specimens showed a typical crack propagation observed in LPS. The initial failure was originated from the solidified phase which acted as a weak-link [5,17,38]. Fig. 3.23(a-c) show that only a single major crack propagated through the cross-section of specimen when the transferred load exceeded the critical strength. On the other hand, several cracks (white arrows) were observed in Fe-5Mo-0.4B-0.8C alloy in a direction parallel to the fracture surface with the detectable damage in both grain boundary and grain (Fig. 3.23(d)). It indicates that the strain was effectively shared, thereby increasing the elongation to failure in Fe-5Mo-0.4B-0.8C alloy. This effect was more visible in the process of crack formation and propagation after indentation [56]. As shown in Fig. 3.24 (a-c), the Fe-0.4B-0.8C, Fe-1Mo-0.4B-0.8C, and Fe-3Mo-0.4B-0.8C alloys showed the

several cracks in the solidified phase around the indentation mark, which propagate through the continuous network of solidified phase and result in the specimen failure. Thus, the initial decrease of elongation to failure can be attributed to the decrease of ductility in Mo-containing solidified phase. On the other hand, the cracks were rarely observed around the indentation mark (Fig. 3.25) and could not propagate through the grain boundary with the lamella structure in Fe-5Mo-0.4B-0.8C alloy (Fig. 3.24 (d)). The discontinuous morphology led to suppress the crack propagation due to the extensive deformation during the indentation. It indicated that the alternating  $(\text{Fe,Mo})_3(\text{C,B})$  and  $\text{MoFe}(\text{C,B})$  with different mechanical properties (hardness) can be effective to suppress the crack propagation and failure of the sintered alloys. Based on the microstructure comparison after tensile test and indentation test, the effect of lamellar structure on the mechanical properties was schematically depicted in Fig. 3.26. Consequently, at 5 wt% Mo addition, the tensile strength of 674 MPa and elongation to failure of 4.92 % were achieved and the product of these two values obtained in this study was one of the best values in boron-containing alloys (Fig. 3.27) [1,5,8,17,39,57].

### **3.4. Conclusions**

In this work, Fe-Mo-B-C alloys were prepared by LPS and their microstructure and mechanical properties were examined. With the addition of Mo in Fe-B-C alloy system, the Fe-Mo-B and Fe-B-C solidification reactions sequentially occurred during solidification and the continuous liquid with a good wetting characteristics led to a nearly full densification in all the compositions investigated. A significant

improvement in mechanical properties such as hardness, tensile strength, and elongation to failure (ductility) was observed in the Mo-added alloys. The improved mechanical properties can be attributed to the microstructural changes of grain from pearlite and re-precipitated ferrite to pearlite (or pearlite/bainite) and of grain boundary from continuous network into lamellar structure. Based on the atomic resolution HAADF-STEM, SAED, EDS, and DFT calculation results, the alternating layers in the grain boundary were identified to be  $\text{MoFe}(\text{C}_{0.75}\text{B}_{0.25})$  and  $(\text{Fe},\text{Mo})_3(\text{C},\text{B})$ . The grain boundary with a lamella structure observed in Fe-5Mo-0.4B-0.8C alloy was effective to share the tensile stress and suppress the crack propagation, which resulted in high tensile strength of 674 MPa and high elongation to failure of 4.92%.

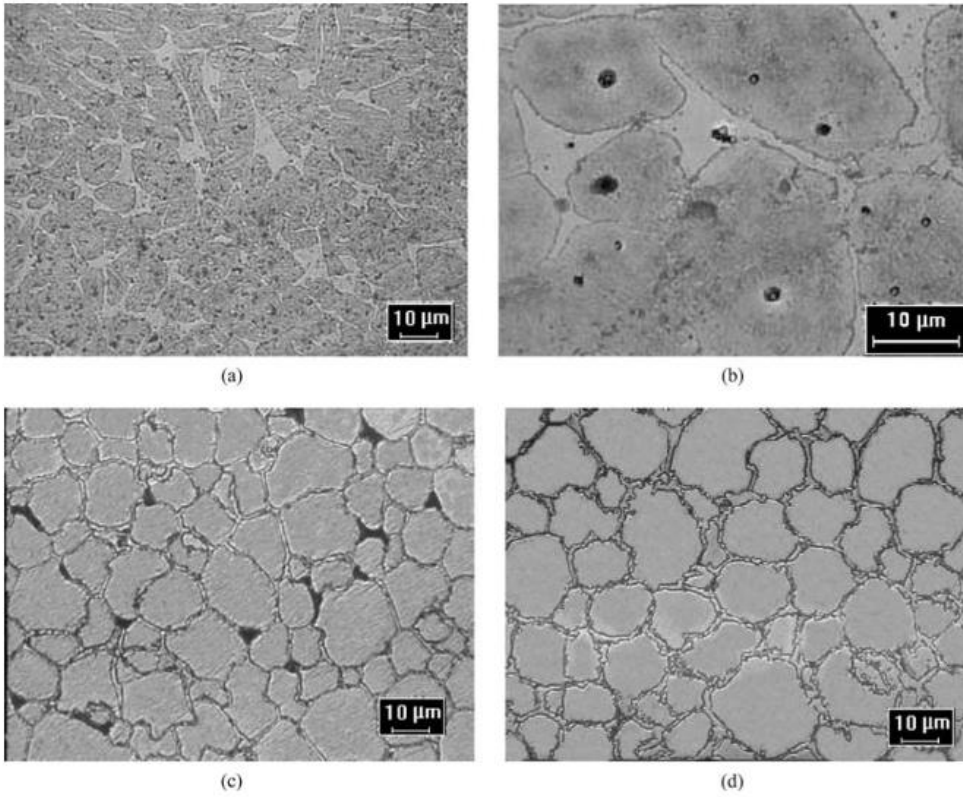


**Figure 3.1.** Microstructures of the liquid phase sintered Fe-B-C based alloys without (a and b) NiB and (c and d) with NiB.

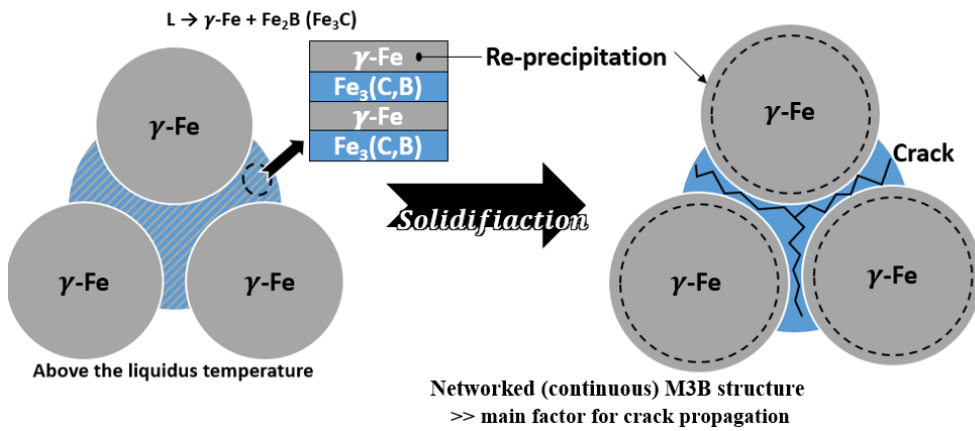


**Figure 3.2.** The schematic the microstructure development in Fe-Mo-B-C with low Mo content (0.5~1.5 wt%).

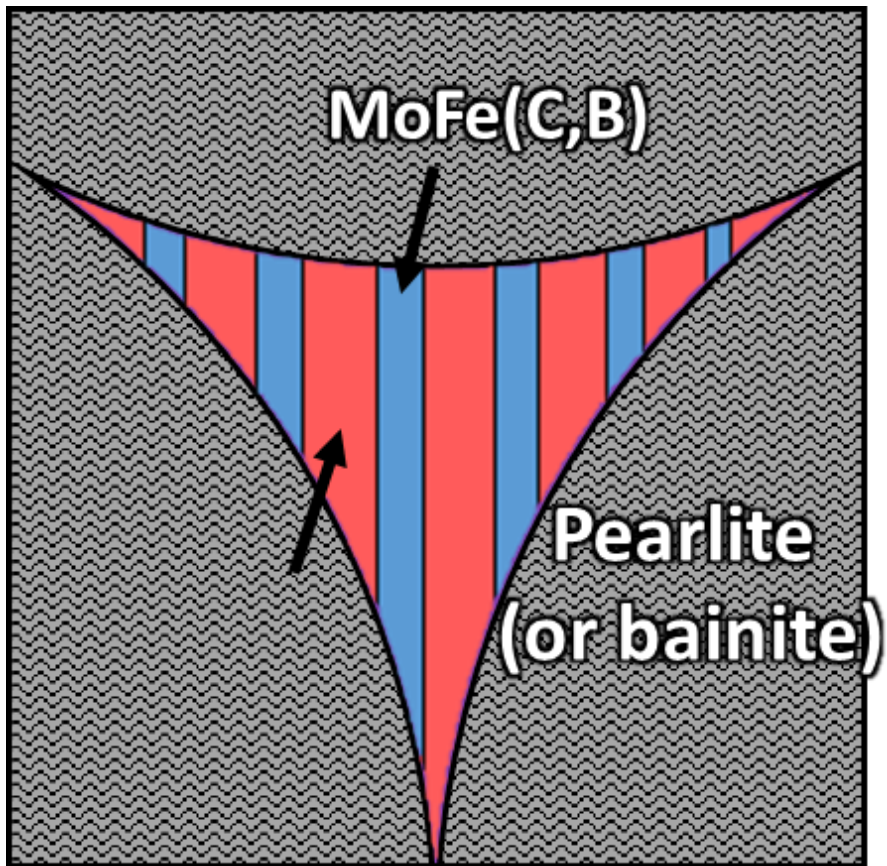


**Figure 3.3.** The schematic the microstructure development in Fe-Mo-B-C with high Mo content (>3.5 wt%)

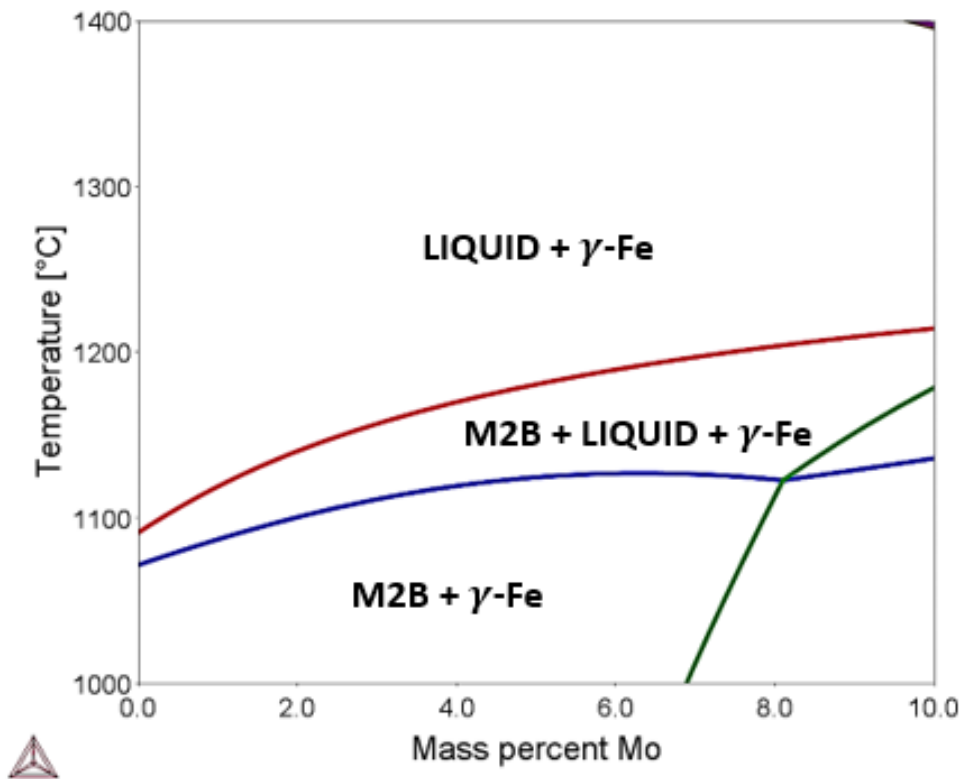


**Figure 3.4.** A Fe-Mo-0.4B-0.8C phase diagram as a function of the Mo content calculated using a thermodynamic database TCFE2000 of Thermo-Calc.

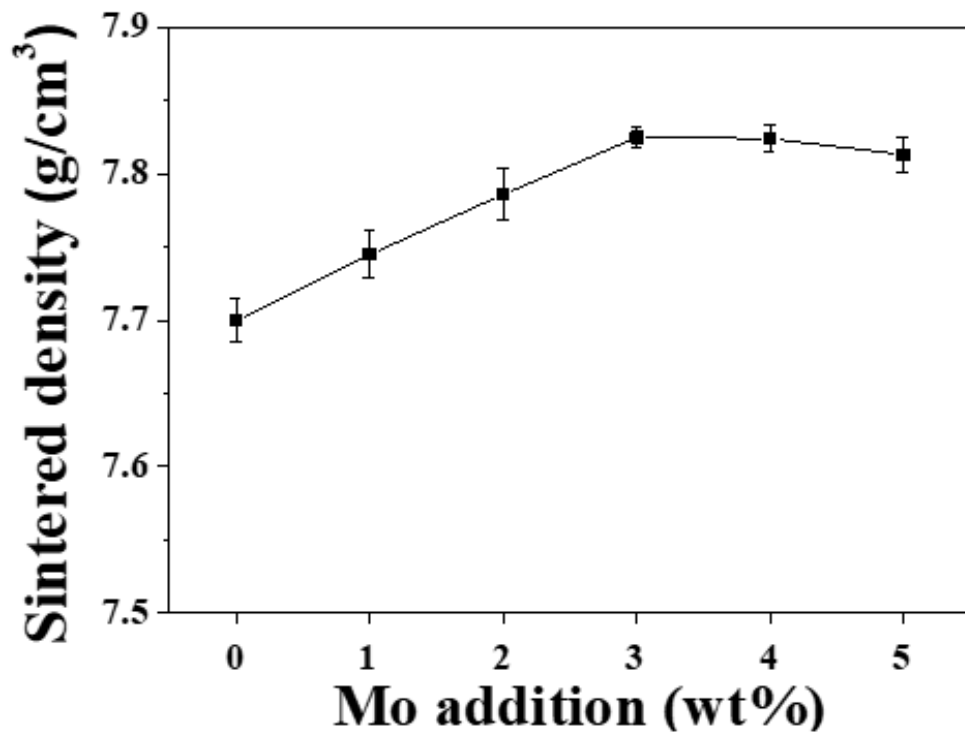
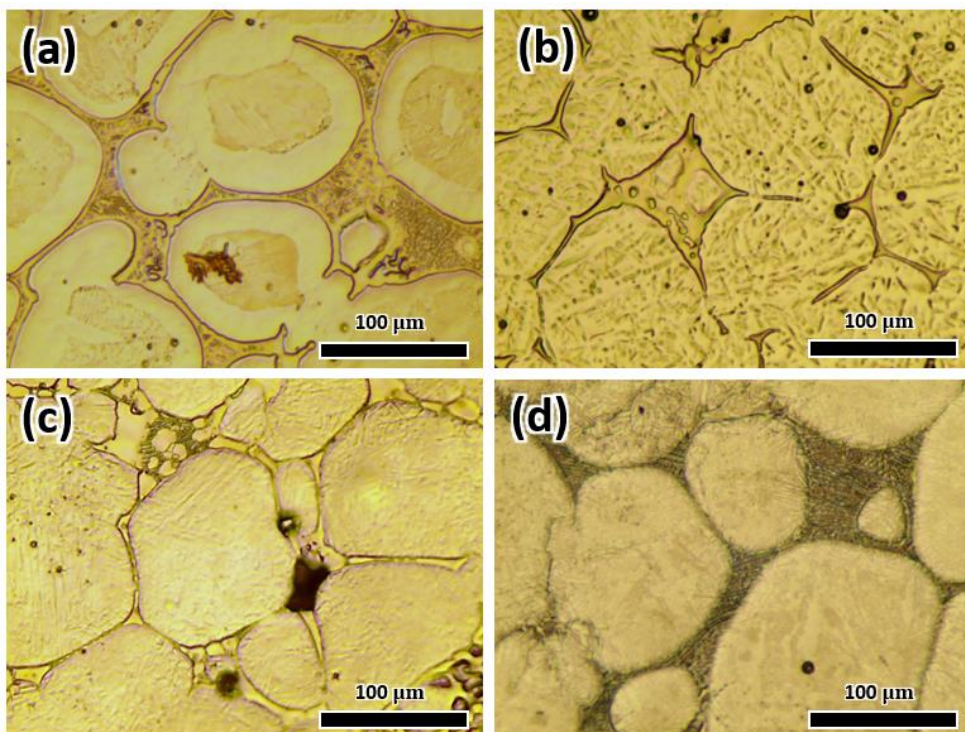
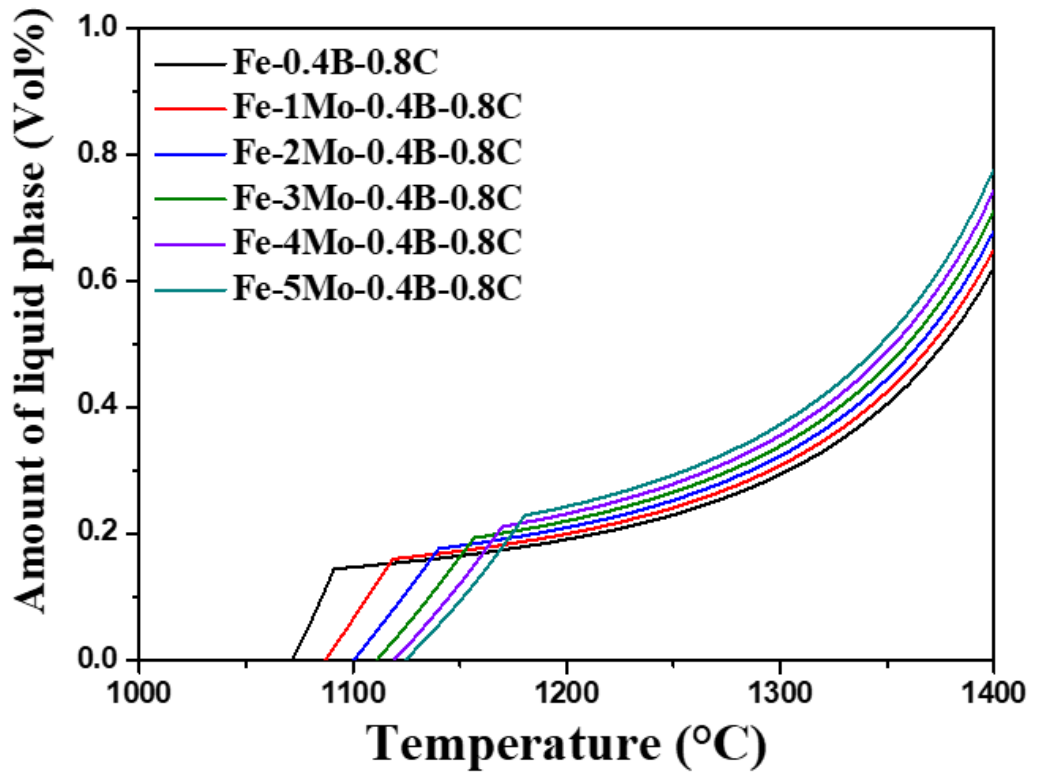


Figure 3.5. Sintered density of Fe-Mo-B-C alloys as a function of Mo content.



**Figure 3.6.** Optical micrographs of (a) Fe-0.4B-0.8C, (b) Fe-1Mo-0.4B-0.8C, (c) Fe-3Mo-0.4B-0.8C and (d) Fe-5Mo-0.4B-0.8C alloys.



**Figure 3.7.** Volume fraction of liquid phase in Fe-Mo-B-C alloys as a function of Mo content.

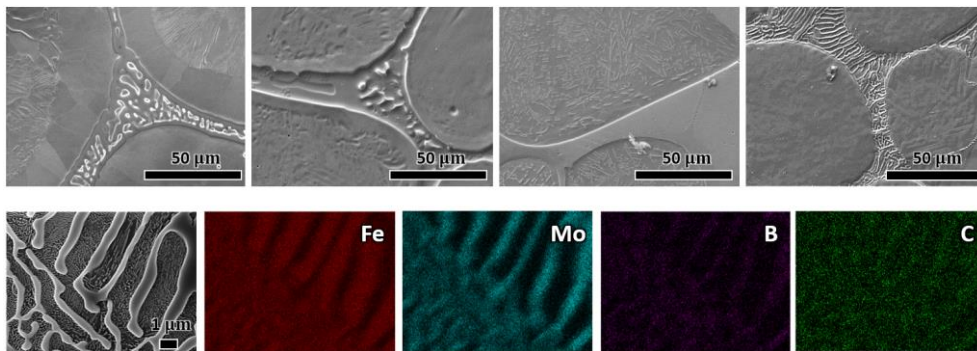
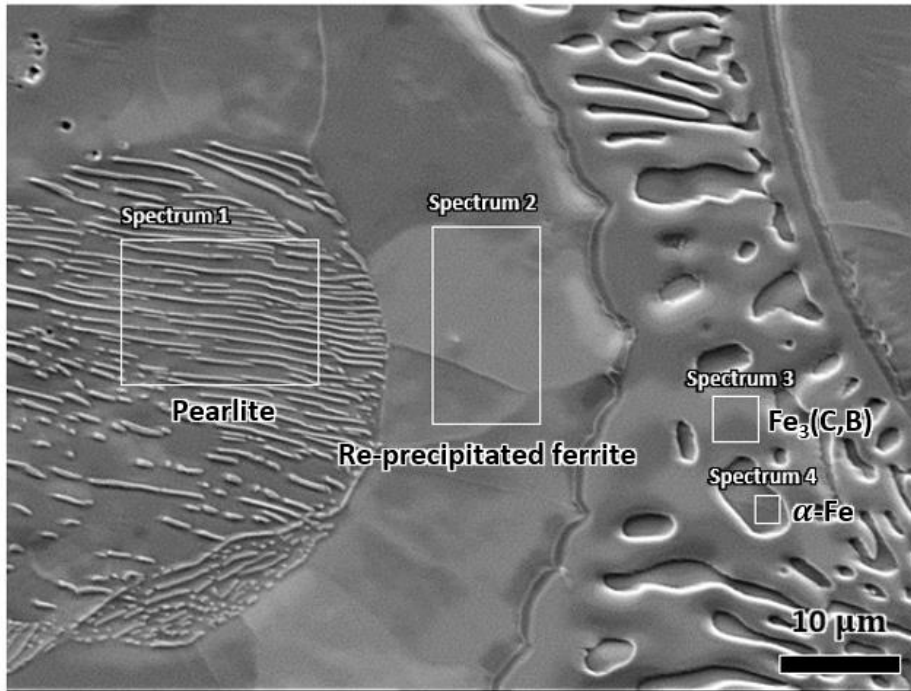


**Figure 3.8.** FE-SEM images (a) Fe-0.4B-0.8C, (b) Fe-1Mo-0.4B-0.8C, (c) Fe-3Mo-0.4B-0.8C, and (d) Fe-5Mo-0.4B-0.8C alloys and (e) EDS mapping images of grain boundary in Fe-5Mo-0.4B-0.8C alloy.



Chemical composition (wt %)			
	Fe	B	C
Spectrum 1	97.7	0	2.3
Spectrum 2	100	0	0
Spectrum 3	93.7	2.2	4.1
Spectrum 4	100	0	0

**Figure 3.9.** FE-SEM image of Fe-0.4B-0.8C alloy and chemical compositions of selected areas by EDS measurements.

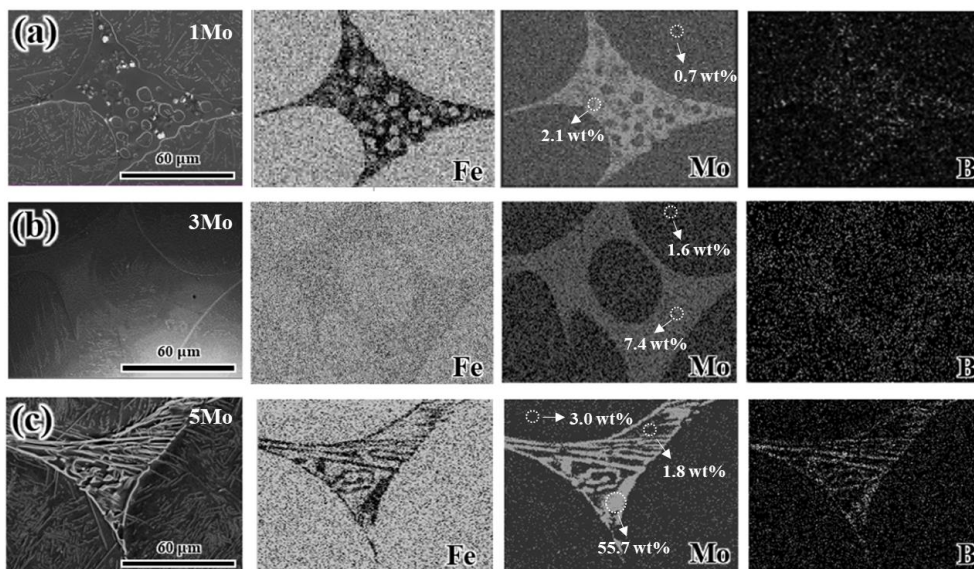


**Figure 3.10.** EDS mapping images of (a) Fe-1Mo-0.4B-0.8C, (b) Fe-3Mo-0.4B-0.8C and (c) Fe-5Mo-0.4B-0.8C alloys.

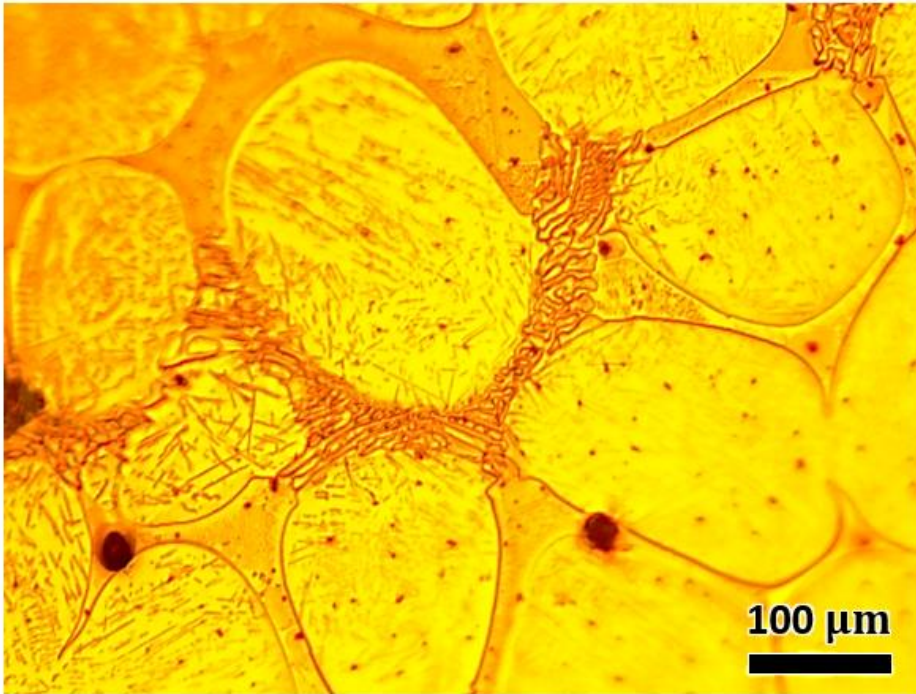


**Figure 3.11.** Optical micrograph of Fe-4Mo-0.4B-0.8C alloy

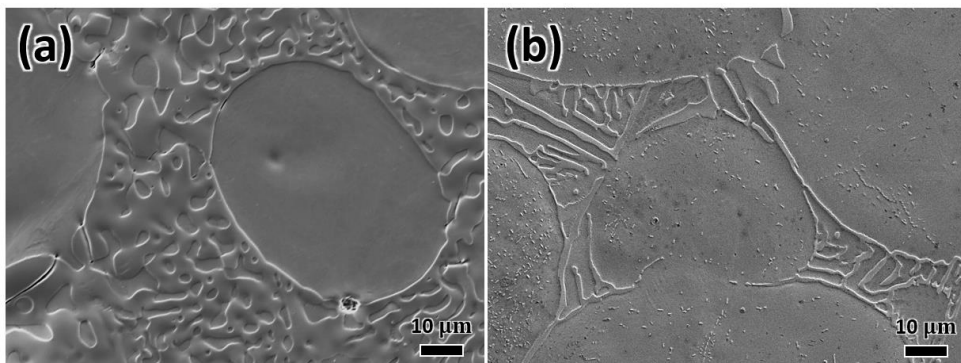


**Figure 3.12.** SEM images of Fe-0.4B-0.8C and Fe-5Mo-0.4B-0.8C alloys quenched from 950 °C.

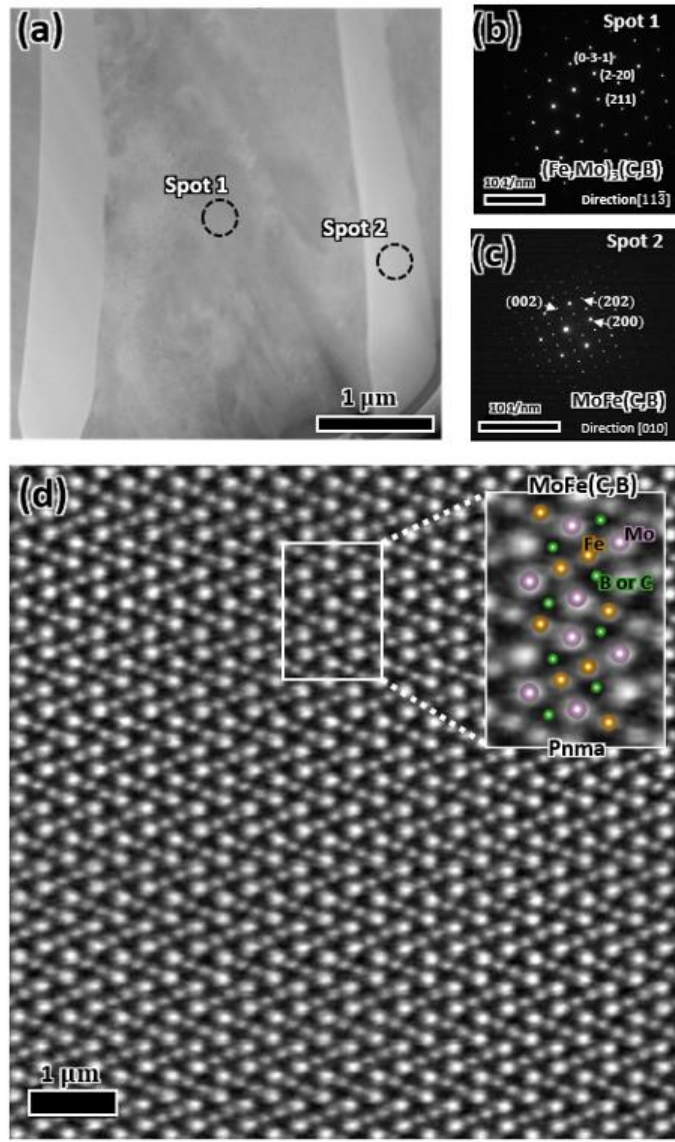


**Figure 3.13.** (a) Low magnification HAADF-STEM image of grain boundary in Fe-5Mo-0.4B-0.8C alloy, selected area diffraction patterns (SADPs) of (b) spot 1 ((Fe,Mo)<sub>3</sub>(C,B)) and (c) spot 2 (MoFe(C,B)), and (d) HAADF-STEM image of spot 2 (MoFe(C,B)) observed by Cs-corrected STEM.

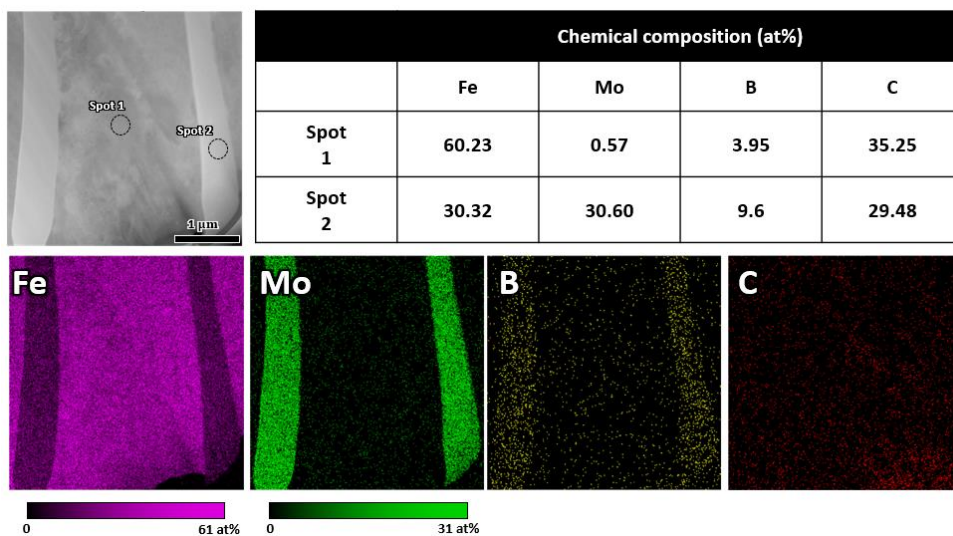


**Figure 3.14.** Point-scan EDS analysis and STEM-EDS mapping images of Fe-5Mo-0.4B-0.8C alloy.

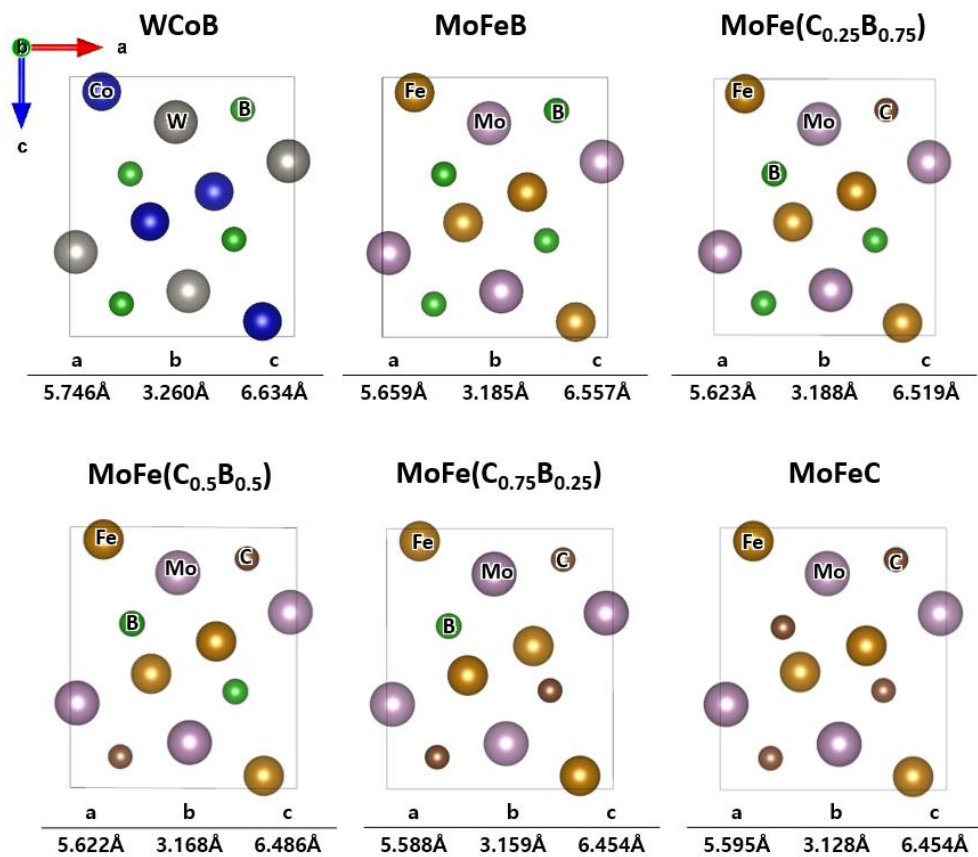


**Figure 3.15.** Atomic structural models and lattice parameters of MoFe(C,B) stabilized by relaxation of DFT calculation.

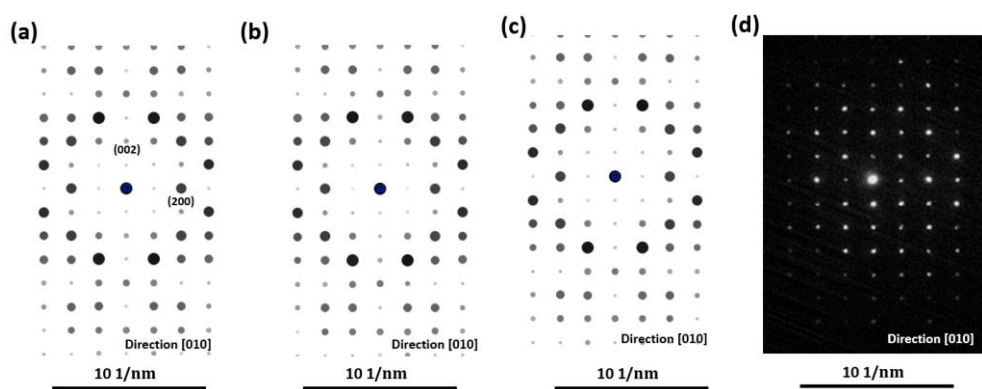


**Figure 3.16.** Simulated diffraction pattern of (a)  $\text{MoFe}(\text{C}_{0.25}\text{B}_{0.75})$ , (b)  $\text{MoFe}(\text{C}_{0.5}\text{B}_{0.5})$ , and (c)  $\text{MoFe}(\text{C}_{0.75}\text{B}_{0.25})$  from the DFT atomic structure by JEMS4 software and (d) experimentally obtained diffraction pattern of  $\text{MoFe}(\text{C},\text{B})$ .

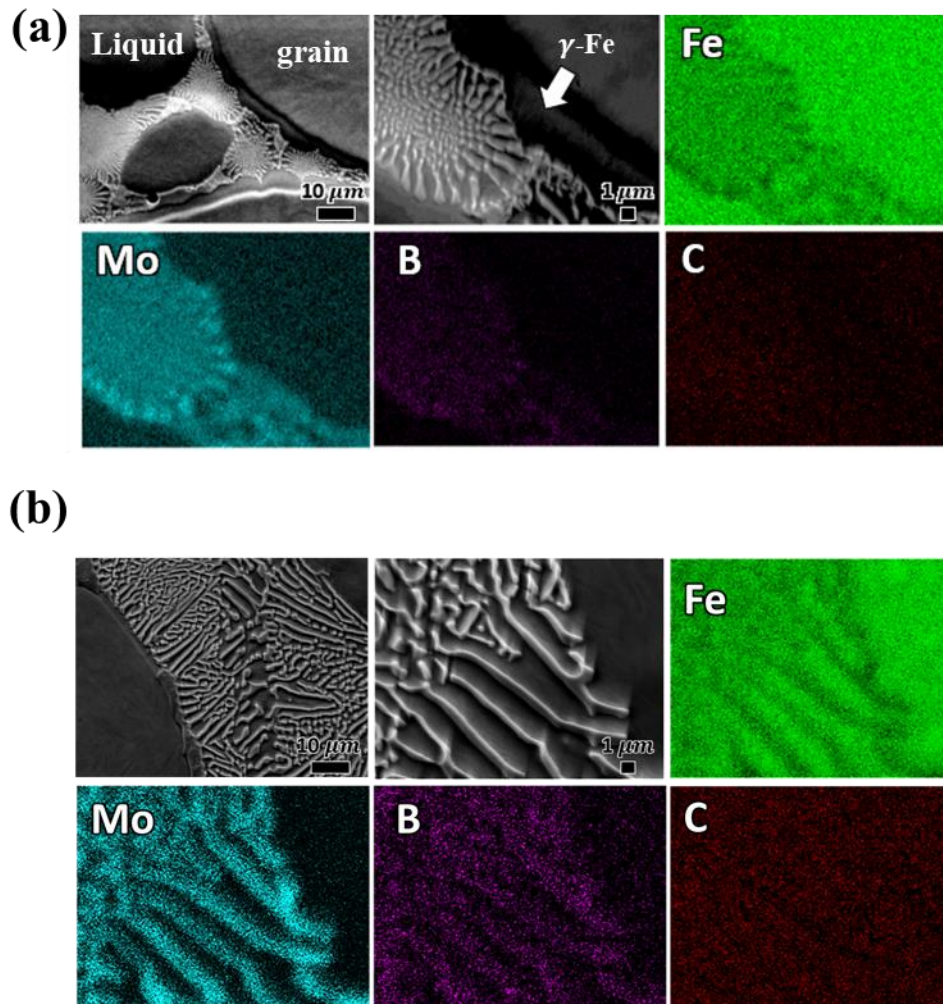


**Figure 3.17.** SEM micrographs and EDS mapping images of Fe-5Mo-0.4B-0.8C alloy quenched from (a) 1180 and (b) 1080 °C.

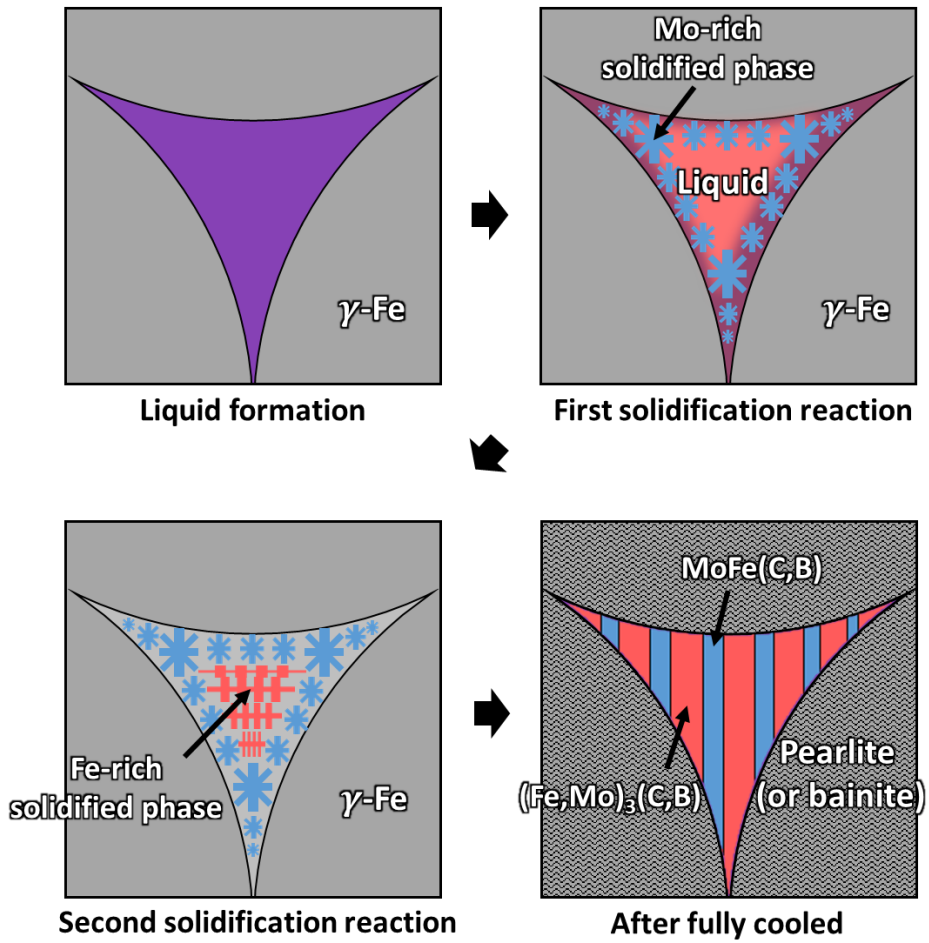


**Figure 3.18.** A schematic illustration of microstructural development in Fe-Mo-B-C system during solidification.

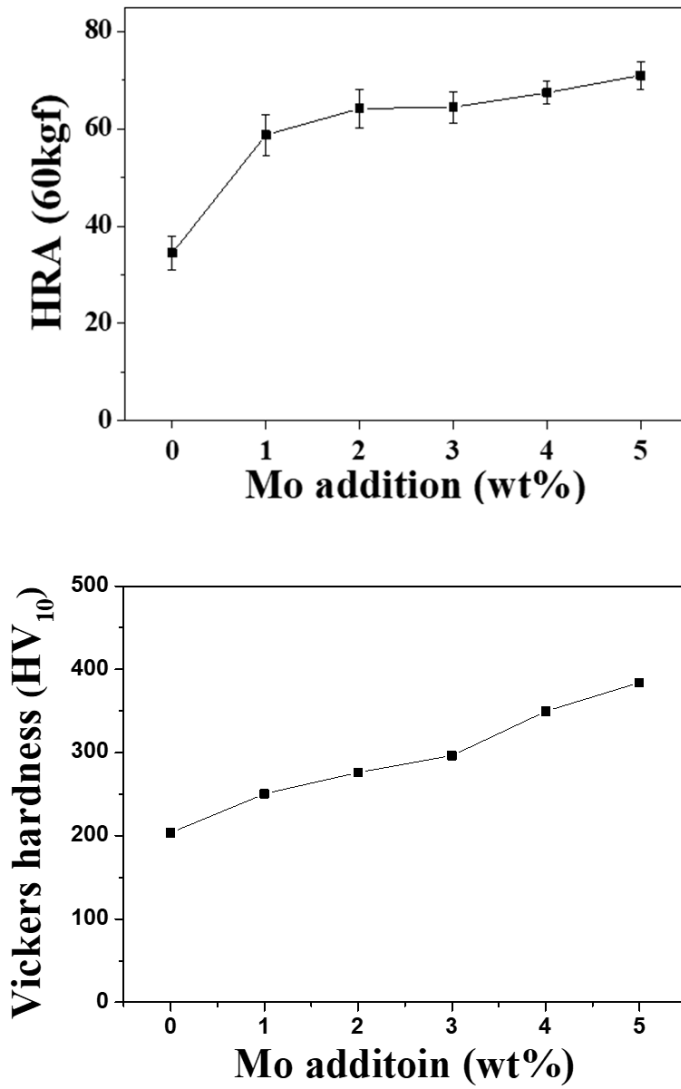


**Figure 3.19.** Rockwell A hardness and Vickers hardness (HV<sub>10</sub>) of Fe-Mo-B-C alloys as a function of Mo content.

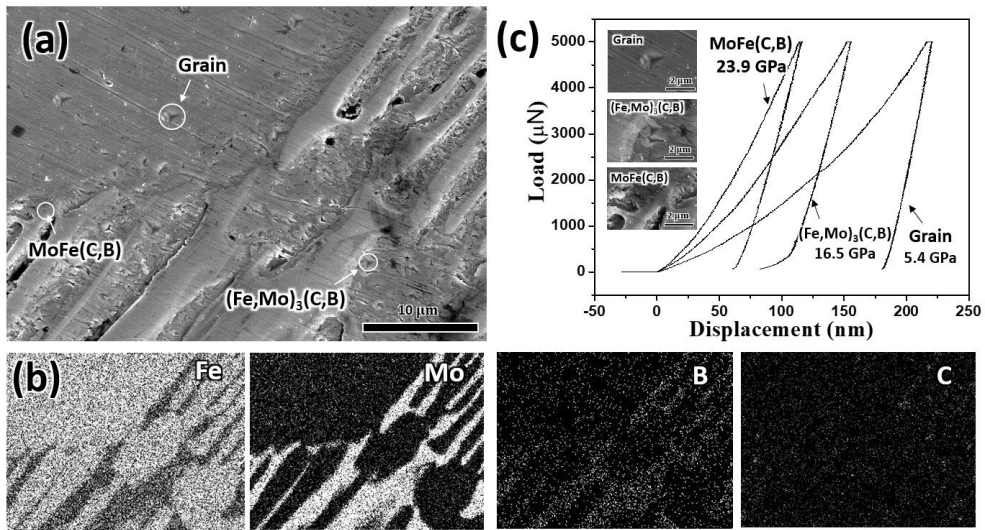


**Figure 3.20.** (a) FE-SEM micrograph and (b) EDS mapping images of Fe-5Mo-0.4B-0.8C alloy after nano indentation experiment and (c) nanoindentation load-displacement curves for constituent phases in Fe-5Mo-0.4B-0.8C alloy.

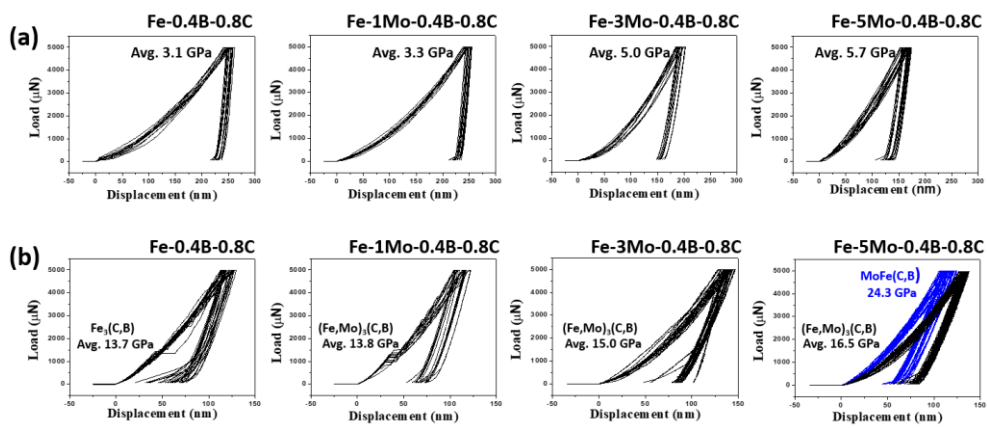


**Figure 3.21.** Nanoindentation load-displacement curves of (a) grain and (b) grain boundary of Fe-0.4B-0.8C, Fe-1Mo-0.4B-0.8C, Fe-3Mo-0.4B-0.8C and Fe-5Mo-0.4B-0.8C alloys.

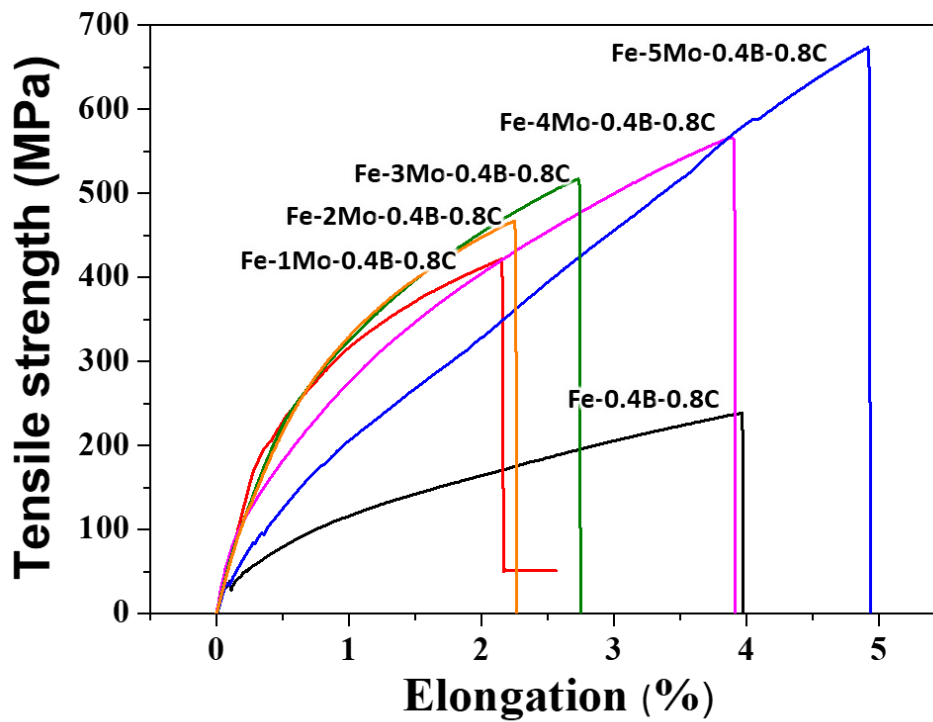
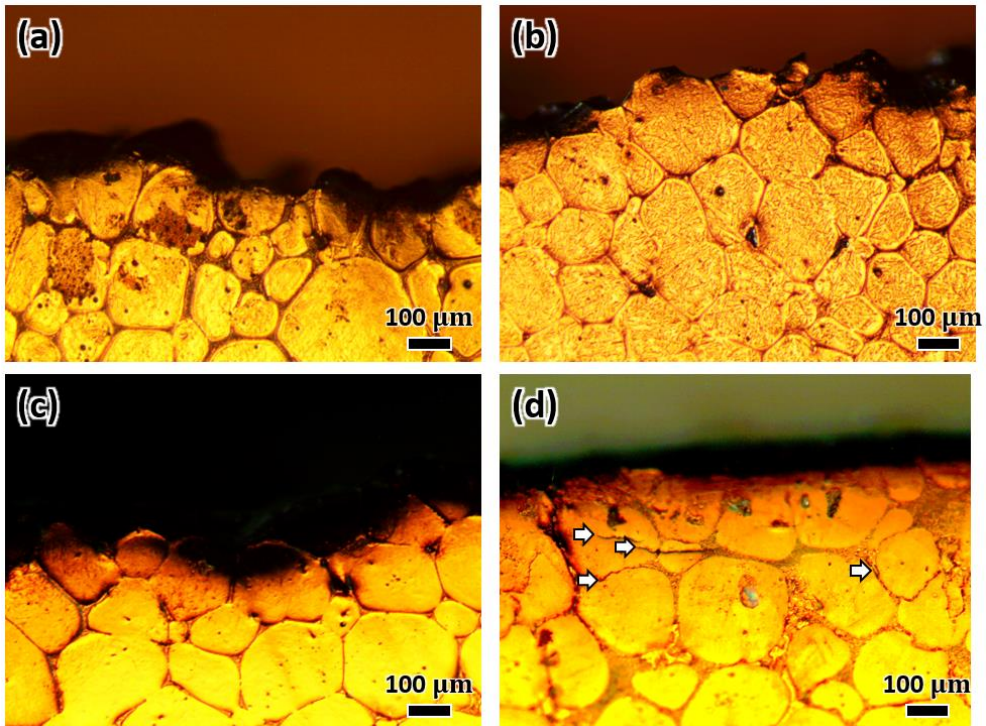
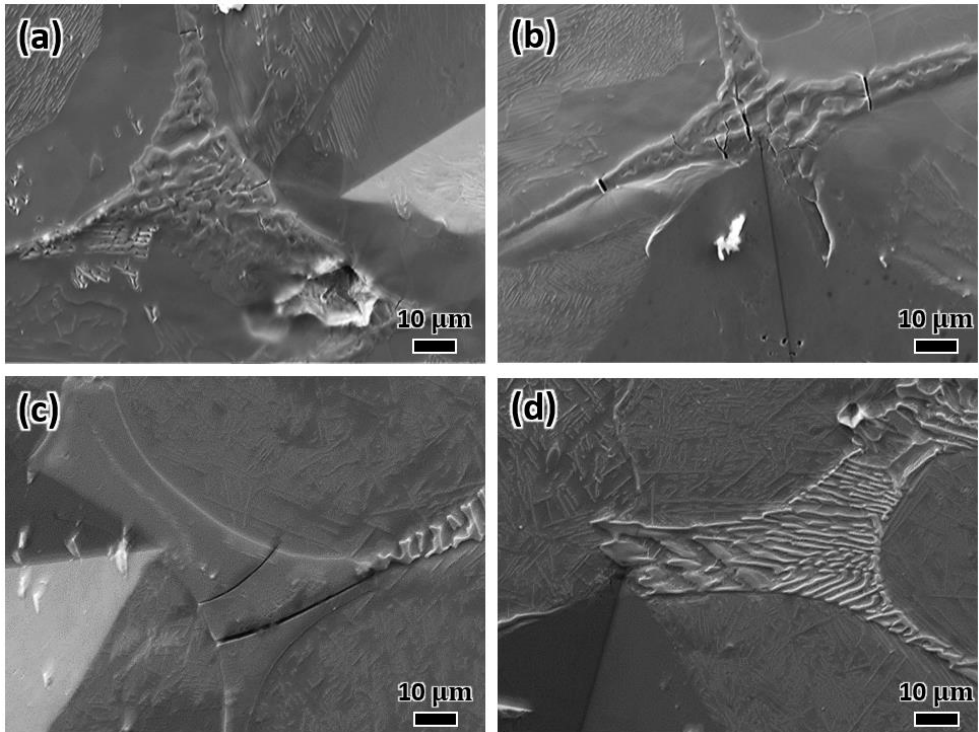


Figure 3.22. Load-elongation curves of Fe-Mo-B-C alloys as a function of Mo content.



**Figure 3.23.** Optical micrographs of (a) Fe-0.4B-0.8C, (b) Fe-1Mo-0.4B-0.8C, (c) Fe-3Mo-0.4B-0.8C, and (d) Fe-5Mo-0.4B-0.8C alloys after tensile test.



**Figure 3.24.** SEM images of (a) Fe-0.4B-0.8C, (b) Fe-1Mo-0.4B-0.8C, (c) Fe-3Mo-0.4B-0.8C, and (d) Fe-5Mo-0.4B-0.8C alloys after indentation test.

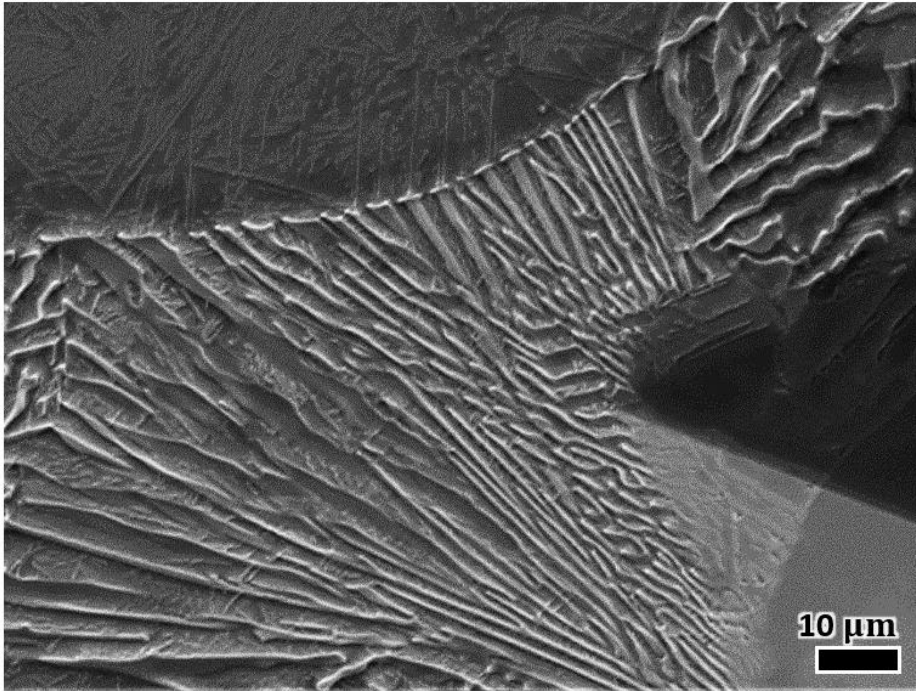


**Figure 3.25.** SEM image of Fe-5Mo-0.4B-0.8C alloy after indentation test (old one).

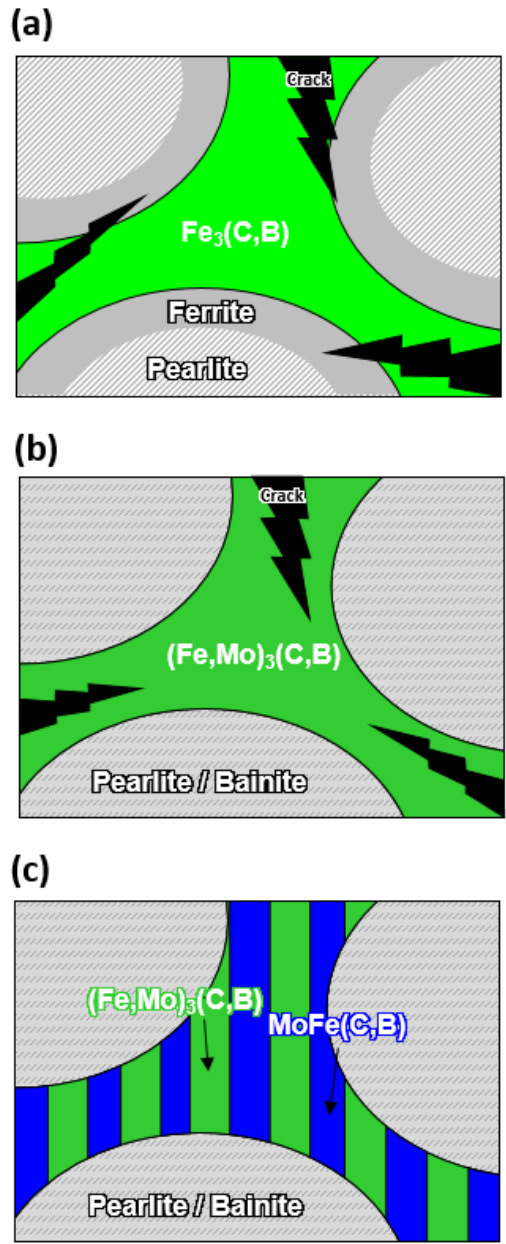


**Figure 3.26.** A Schematic diagram of the effect of lamellar structure on preventing the crack propagation in Fe-Mo-B-C alloys.

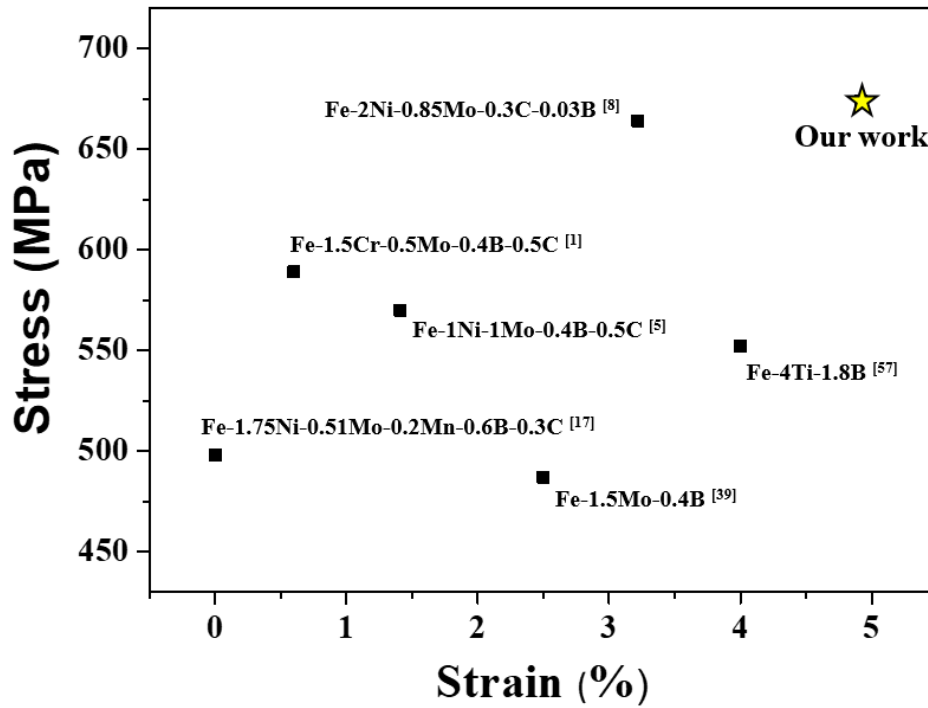


Figure 3.27. Comparison of the measured tensile strength and elongation to failure of boron-containing alloys prepared by liquid phase sintering

## Reference

- [1] K. S. Narasimhan, Sintering of powder mixtures and the growth of ferrous powder metallurgy, *Mater. Chem. Phys.* 67 (2001) 56-65.
- [2] A. Hadrboletz, B. Weiss, Fatigue behaviour of iron based sintered material: a review, *Int. Mater. Rev.* 42 (1997) 1-44.
- [3] R. M. German, Supersolidus liquid-phase sintering of prealloyed powders, *Metall. Mater. Trans. A* 28 (1997) 1553-1567.
- [4] R. M. German, P. Suri, S. J. Park, Review: liquid phase sintering, *J. Mater. Sci.* 44 (2009) 1-39.
- [5] J. Liu, A. Cardamone, T. Potter, R. M. German, F. J. Semel, Liquid phase sintering of iron-carbon alloys with boron additions, *Powder Metall.* 43 (2000) 57-61.
- [6] W. Khraisat, L. Nyborg, Liquid phase sintering of ferrous powder by carbon and phosphorus control, *Powder Metall.* 46 (2003) 265-270.
- [7] R. Annamalai, A. Upadhyaya, D. Agrawal, An investigation on microwave sintering of Fe, Fe-Cu and Fe-Cu-C alloys, *Bull. Mater. Sci.* 36 (2013) 447-456.
- [8] M. Marucci, A. Lawley, R. Causton, S. Saritas, Effect of small additions of boron on the mechanical properties and hardenability of sintered P/M steels, In: Arnhold, V., Chu, C.-L., Jandeska, W.F., Sanderow, H.I. (eds) *Advances in Powder Metallurgy and Particulate Materials*, MPIF, Princeton (2002) 53-63.

- [9] Y. C. Peng, H. J. Jin, J. H. Liu, G. L. Li, Effect of boron on the microstructure and mechanical properties of carbidic austempered ductile iron, *Mater. Sci. Eng. A* 529 (2011) 321-325.
- [10] H. O. Gulsoy, M. K. Bilici, Y. Bozkurt, S. Salman, Enhancing the wear properties of iron based powder metallurgy alloys by boron additions, *Mater. Des.* 28 (2007) 2255-2259.
- [11] J. Lentz, A. Röttger, W. Theisen, Solidification and phase formation of alloys in the hypoeutectic region of the Fe-C-B system, *Acta Mater.* 99 (2015) 119-129.
- [12] C. Yang, F. Liu, G. Yang, Y. Chen, N. Liu, Y. Zhou, Microstructure and phase selection in bulk undercooled Fe-B eutectic alloys, *J. Alloys. Compd.* 441 (2007) 101-106.
- [13] L. Lacaze, Pearlite growth in cast irons: a review of literature data, *Int. J. Cast. Metal. Res.* 29 (2011) 405-418.
- [14] R. M. German, K. A. D'angelo, Enhanced sintering treatments for ferrous powders, *Int. Metal. Rev.* 29 (1984) 249-272.
- [15] Z. Xiu, A. Salwen, X. Qin, F. He, X. Sun, Sintering behaviour of iron-molybdenum steels with the addition of Fe-B-C master alloy powders, *Powder Metall.* 46 (2003) 171-174.
- [16] M. -W. Wu, Y. -C. Fan, H. -Y. Huang, W. -Z. Cai, Liquid phase sintering of boron-containing powder metallurgy steel with chromium and carbon, *Metall. Mater. Trans. A* 46 (2015) 5285-5295.

- [17] S. Egashira, T. Sekiya, T. Ueno, M. Fujii, Effect of boron addition on mechanical properties of Fe-Ni-Mo-B-C sintered alloys, *Jpn. Soc. Mech. Eng.* 6 (2019) 1-11.
- [18] B. H. Rabin, R. M. German, Microstructure effects on tensile properties of tungsten-nickel-iron composites, *Metall. Trans. A* 19 (1988) 1523-1532.
- [19] C. Baron, H. Springer, On the effect of Ni additions to Fe-Cr-B high modulus steels, *Mater. Des.* 147 (2019) 107624.
- [20] A. Röttger, J. Lentz, W. Theisen, Boron-alloyed Fe-Cr-C-B tool steels - Thermodynamic calculations and experimental validation, *Mater. Des.* 88 (2015) 420-429.
- [21] M. Sharma, I. Ortlepp, W. Bleck, Boron in Heat-Treatable Steels: A Review, *Steel Res. Int.* 90 (2019) 1900133.
- [22] P. Sang, H. Fu, Y. Qu, C. Wang, Y. Lei, Effect of boron concentration on solidification structure and hardness of Fe-B-C wear-resistant alloy, *Werkstofftech.* 46 (2015) 962-969.
- [23] X. Ren, H. Fu, J. Xing, Y. Yang, S. Tang, Effect of boron concentration on microstructures and properties of Fe-B-C alloy steel, *J. Mater. Res.* 32 (2017) 3078-3088.
- [24] F. Li, Z. Li, Study on improvement of hard phase morphology and properties of hypoeutectic Fe-C-B alloy, *J. Alloys. Compd.* 587 (2014) 267-272.
- [25] Z. Liu, X. Chen, Y. Li, K. Hu, High boron iron-based alloy and its modification,

- J. Iron. Steel. Res. Int. 16 (2009) 37-42.
- [26] H. Fu, Q. Xiao, J. Kuang, J. Xing, Effect of rare earth and titanium additions on the microstructures and properties of low carbon Fe–B cast steel, Mater. Sci. Eng. A 466 (2007) 160-165.
- [27] X. Wei, Z. Chen, J. Zhong, L. Wang, W. Yang, Y. Wang, Effect of alloying elements on mechanical, electronic and magnetic properties of Fe<sub>2</sub>B by first-principles investigations, Comput. Mater. Sci. 147 (2018) 322-330.
- [28] H. I. Bakan, D. Heaney, R. M. German, Effect of nickel boride and boron additions on sintering characteristics of injection moulded 316L powder using water soluble binder system, Powder Metall. 44 (2001) 235-242.
- [29] S. S. Rathore, M. M. Salve, V. V. Dabhade, Effect of molybdenum addition on the mechanical properties of sinter-forged Fe–Cu–C alloys, J. Alloy. Compd. 649 (2015) 988-995.
- [30] F. Han, B. Hwang, D. Suh, Z. Wang, D. L. Lee, S. Kim, Effect of molybdenum and chromium on hardenability of low-carbon boron-added steels, Met. Mater. Int. 14 (2008) 667-672.
- [31] X. Chen, Q. Zhai, H. Dong, B. Dai, H. Mohrbacher, Molybdenum alloying in cast iron and steel, Adv. Manuf. 8 (2020) 3-14.
- [32] Z. Xiu, A. Salwen, X. Qin, F. He, X. Sun, Sintering behaviour of iron-molybdenum steels with the addition of Fe-B-C master alloy powders, Powder Metall. 46 (2003) 171-174.

- [33] M. Sarasola, T. Gómez-Acebo, F. Castro, Microstructural development during liquid phase sintering of Fe and Fe-Mo alloys containing elemental boron additions, *Powder Metall.* 48 (2005) 59-67.
- [34] M. Sarasola, C. Tojal, F. Castro, Study of boron behaviour during sintering of Fe/Mo/B/C alloys to near full density, *Euro PM2004 Conference Proceedings*, Vienne (Austria) 3 (2004) 319-326.
- [35] M. Sarasola, T. Gómez-Acebo, F. Castro, Liquid generation during sintering of Fe-3.5%Mo powder compacts with elemental boron additions, *Acta Mater.* 52 (2004) 4615-4622.
- [36] M. -W. Wu, W. -Z. Cai, Z. Lin, S. Chang, Liquid phase sintering mechanism and densification behavior of boron-alloyed Fe-Ni-Mo-C-B powder metallurgy steel, *Mater. Des.* 133 (2017) 536-548.
- [37] M. -W. Wu, W. -Z. Cai, Phase identification in boron-containing powder metallurgy steel using EBSD in combination with EPMA, *Mater. Charact.* 113 (2016) 90-97.
- [38] Z. M. Xiu, L. X. Ding, Z. J. Zhao, J. You, Z. Zhang, F. M. He, X. D. Sun, Fe-Mo-B-C sintered steels produced by addition of master alloy powders, *Acta Metall. Sin-Engl.* 12 (1999) 1198-1201.
- [39] E. Dudrova, M. Selecka, R. Bures, M. Kabatova, Effect of boron addition on microstructure and properties of sintered Fe-1.5Mo powder microstructure materials, *ISIJ Int.* 37 (1997) 59-64.
- [40] N. Tosangthum, P. Kunnam, M. Morakotjinda, W. Koetniyom, R. Krataitong,

- P. Wila, R. Tongsri, Effect of boron addition and sintering atmosphere on precipitation in sintered Fe-Mo-C steels, *Key Eng. Mater.* 798 (2019) 9-16.
- [41] J. O. Andersson, T. Helander, L. Hoglund, P. Shi, B. Sundman, Thermo-Calc & Dictra, computational tools for materials science, *CALPHAD* 26 (2002) 273-312
- [42] V. B. Rajkumar, K.C. Hari Kumar, Thermodynamic modeling of the Fe-Mo system coupled with experiments and ab initio calculations, *J. Alloys. Compd.* 611 (2014) 303-312.
- [43] M. Sharma, I. Ortlepp, W. Bleck, Boron in Heat-Treatable Steels: A Review, *Steel Res. Int.* 90 (2019) 1900133.
- [44] T. Zhang, H. Yin, C. Zhang, R. Zhang, X. Jiang, Q. Zheng, X. Qu, First-principles study on the mechanical properties and electronic structure of V doped WCoB and W<sub>2</sub>CoB<sub>2</sub> ternary borides, *Materials* 12 (2019) 967-983.
- [45] A. K. Iyer, Y. Zhang, J. P. Scheifers, B. P. T. Fokwa, Structural variations, relationships and properties of M<sub>2</sub>B metal borides, *J. Solid State Chem.* 270 (2019) 618-635.
- [46] P. Sang, H. Fu, Y. Qu, C. Wang, Y. Lei, Effect of boron concentration on solidification structure and hardness of Fe-B-C wear-resistant alloy, *Werkstofftech.* 46 (2015) 962-969.
- [47] R. Wan, F. Sun, L. Zhang, A. Shan, Effects of Mo on high-temperature strength of fire-resistant steel, *Mater. Des.* 35 (2012) 335-341.

- [48] Y. Yi, Q. Li, J. Xing, H. Fu, D. Yi, Y. Liu, B. Zheng, Effects of cooling rate on microstructure, mechanical properties, and residual stress of Fe-2.1B (wt%) alloy, *Mater. Sci. Eng. A* 754 (2019) 129-139.
- [49] R. Rodriguez, I. Gutierrez, Correlation between nanoindentation and tensile properties influence of the indentation size effect, *Mater. Sci. Eng. A* 361 (2003) 377-384.
- [50] X. Ren, H. Fu, J. Xing, Y. Yang, S. Tang, Effect of boron concentration on microstructures and properties of Fe-B-C alloy steel, *J. Mater. Res.* 32 (2017) 3078-3088.
- [51] H. Hu, G. Xu, L. Wang, Z. Xue, Y. Zhang, G. Liu, The effects of Nb and Mo addition on transformation and properties in low carbon bainitic steels, *Mater. Des.* 84 (2015) 95-99.
- [52] J. Lentz, A. Röttger, W. Theisen, Hardness and modulus of Fe<sub>2</sub>B, Fe<sub>3</sub>(C,B), and Fe<sub>23</sub>(C,B)<sub>6</sub> borides and carboborides in the Fe-C-B system, *Mater. Charact.* 135 (2018) 192-202.
- [53] N. Myers, P. Suri, R. M. German, High density P/M steel, *Advances in Powder Metallurgy and Particulate Materials*, Princeton (2000) 6.63-6.68.
- [54] J. Karwan-Baczewska, The properties of Fe-Ni-Mo-Cu-B materials produced via liquid phase sintering, *Arch. Metall. Mater.* 56 (2011) 789-796.
- [55] W. Koetnuyom, P. Chantawet, N. Tosangthum, M. Morakotjinda, T. Yotkaew, P. Wila, R. Tongri, Effect of carbon addition on microstructure and properties of boron-containing steel sintered under different atmospheres, *J. Met. Mater.*

Miner. 29 (2019) 22-30.

- [56] A. Röttger, S. Weber, W. Theisen, Supersolidus liquid-phase sintering of ultrahigh-boron high-carbon steels for wear-protection applications, Mater. Sci. Eng. A 532 (2012) 511-521.
- [57] Y. Liu, B. Li, J. Li, L. He, S. Gao, T. G. Nieh, Effect of titanium on the ductilization of Fe–B alloys with high boron content, Mater. Lett. 64 (2010) 1299-1301

# **Chapter 4. Densification mechanism and microstructure development of Fe-Ni alloys consolidated by field assisted sintering**

## **4.1. Introduction**

Ferrous powder metallurgy (P/M) has significantly advanced due to net-shape capability, high productivity, and low cost, and has been widely applied in automobile, home appliances, and electronic devices [1]. Unfortunately, the iron (Fe)-based alloys fabricated by conventional sintering (CS) is limited due to porosity ranging from 5 to 15 vol. % [2], and prolong sintering leads to the abnormal grain growth [3,4], which is detrimental to the mechanical properties of Fe- based alloys. To solve these problems, hot pressing (HP) [5,6], hot isostatic pressing (HIP) [7,8], and field assisted (activated) sintering technique (FAS or FAST) [9-14] have been adopted. Among them, FAS technique (or spark plasma sintering (SPS)) is an attractive method where a pulsed direct electric current passes through the powder with a mechanical pressure, which allows nearly full densification with a limited grain growth at short sintering time. However, the densification mechanism of FAS is still controversial due to the inherent difficulty in separating the intrinsic FAS effects from the thermal effects. Previously, researchers thought that a high electric pulsed current generated plasma, leading to an enhancement of thermal diffusion of

the sintered specimen, but there has been no clear evidence demonstrating the existence of spark plasma [14,15]. Several attempts have been explored to demonstrate the densification mechanism of FAS by comparative study [16,17], DFT calculation [18,19], and creep deformation model [20-22], but these studies were limited to provide direct evidences of material diffusion in a single phase material. On the other hand, the enhanced diffusion has been suggested as the densification mechanism in composite materials or diffusion couples by FAS [23-27]. In the diffusion couples such as Fe-Al and W-Ti, the interdiffusion coefficient during FAS was observed to be much higher than that of the conventional sintering. These results suggested that the diffusion-related densification under FAS can be investigated by adding the second element or fabricating the diffusion couple.

Among various alloy elements in Fe-based alloys, nickel (Ni) has received a great attention due to its high strength, toughness, low oxygen affinity, and solid solution strengthening [28-30]. Especially, Ni addition to the Fe-based alloys was found to enhance the densification and suppress the abnormal grain growth during CS, which resulted in significant increase of the mechanical properties [31-33]. Several studies have reported that FAS allows to fabricate fully dense Fe-Ni alloys with suppressed grain growth, however, the enhanced diffusion during FAS was not clearly demonstrated, possibly due to phase transformation and solid solution behavior at high concentration of Ni addition (>30 wt%) [34-36]. In addition, the microstructural development and mechanical properties (bulk hardness) of Fe-Ni alloys fabricated by FAS with a low Ni content (<5 wt%) has not been fully explored.

In this study, Fe-xNi alloys ( $x=0\sim 5.0$  in wt%) were consolidated by CS, HP and FAS methods, and their densification, microstructure, elemental distribution, and

mechanical properties were comparatively investigated by SEM, TEM, EDS and diffusion couple experiment, focusing on the field or current effects of FAS method. The Ni addition was employed to suppress the grain growth and enhance the densification, and FAS method was utilized to produce the Fe-Ni alloys with higher apparent density and smaller grain size. Consequently, the Fe-Ni alloys fabricated by FAS achieved nearly full densification without noticeable grain growth. Indeed, the electric current along with mechanical pressure in FAS facilitated the grain boundary diffusion of Ni, and enhanced the densification with suppressed grain growth, which resulted in a significant improvement of the bulk hardness compared to those sintered by CS and HP.

## **4.2. Experimental**

The Fe-Ni alloys were prepared using commercially available Fe powder (<150  $\mu\text{m}$ , ASC100.29, Hoganas) and Ni powder (<1  $\mu\text{m}$ , Sigma Aldrich). The content of Ni was varied from 0 to 5 wt% and the samples are designated as Fe-xNi (x% of the total powder mixture mass). The starting powders were hand-mixed and subsequently mixed by V-mixer. For FAS, 1.5 g of the mixed powder was placed into 10 mm diameter graphite die and the boron nitride powder was inserted between mixed powder and boron nitride sprayed graphite punch to reduce the carbon contamination. It was reported that the boron nitride spacer between graphite punch and sample forced the electrical current to flow through the graphite or graphite sheet, which resulted in inhomogeneous microstructure in some cases [37-39]. However,

the boron nitride spacer in this study was very thin and Fe powder was highly conductive and thus, the microstructure was uniform and homogeneous throughout the specimens. Based on preliminary experiments, where FAS was performed depending on temperature (Fig. 4.1), sintering was carried out at 1000 °C for 10 min. During FAS, an electric current of ~1000 A was applied with a pressure of 60 MPa at a heating/cooling rate of 100 °C/min under a vacuum condition, and the pulse frequency was fixed at 3.2 kHz. For comparison, the Fe-xNi alloys were prepared by conventional sintering (CS) and hot pressing (HP) methods. For CS, the mixed powders were compacted into Ø10 mm pellets with a compacting pressure of 600 MPa and sintered at 1150 °C for 120 min at a heating rate of 10 °C/min. HP was performed at 1000 °C for 10 min with a pressure of 60 MPa at a heating/cooling rate of 100 °C/min, which was similar to FAS condition. After sintering, the apparent density (sintered density) of specimens was determined by Archimedes method in distilled water. The samples were grinded and metallographically polished into mirror surface, and the microstructure was observed by optical microscopy (OM, Nikon L-150) and scanning electron microscope (FE-SEM, SU-70) equipped with energy dispersive X-ray spectroscopy (EDS). The grain boundaries of sintered specimen were examined by transmission electron microscopy (TEM, JEM-2100F, JEOL Ltd.). For TEM, the specimen was prepared by focused ion beam (FIB, Helios Nano Lab450, FEI) technique. To investigate the effect of FAS on the grain boundary diffusion, Fe-Ni diffusion couples were prepared by placing two green compacts in contact and sintering by CS (1150 °C for 120 min), HP (1000 °C for 10 min) and FAS (1000 °C for 10 min) and the cross section was investigated by SEM and EDS. The mechanical properties (HRA and HRC) were measured by Rockwell hardness

measurement (Mitutoyo, Japan) on the polished surface.

### 4.3. Results and discussion

The apparent density of the pellets prepared by CS and FAS is shown in Fig. 4.2. The green density of pure Fe was  $6.95 \text{ g/cm}^3$  (88 % of the theoretical density) and the green density of Fe-xNi alloys gradually decreased with increasing the Ni content possibly due to the limited plastic deformation (Fig. 4.3(a)). After the conventional sintering at  $1150 \text{ }^\circ\text{C}$  for 120 min, the apparent density of pure Fe was similar to the green density and thus, the densification was hardly observed. However, the sintered density rapidly increased even with a small Ni addition and reached  $7.68 \text{ g/cm}^3$  (~96.9% relative density) at 5 wt% Ni addition indicating that Ni addition significantly improved the densification of Fe-xNi alloys consistent with the previous work [31-36]. The conventionally sintered pure Fe specimen had a porous microstructure consistent with the relative density of 88.9 % and a significant grain growth was observed resulting in the grain size of  $\sim 100 \text{ }\mu\text{m}$  (Fig. 4.4(a)). The starting Fe powder was a water-atomized agglomerated powder composed of spherical primary particles of  $<10 \text{ }\mu\text{m}$  (Fig. 4.3(b)), and Ni powder was composed of spherical particles with diameters of  $\sim 1 \text{ }\mu\text{m}$  or below (Fig. 4.3(c)). With Ni addition, the residual pores gradually disappeared from the grain boundaries and the grain growth was rather suppressed (Fig. 4.5), which resulted in the grain size of  $\sim 30 \text{ }\mu\text{m}$  at 5 wt% Ni addition (Fig. 4.6(a)). The EDS mapping indicated that Ni was homogeneously distributed throughout the specimen. The solubility limit of Ni in  $\alpha$ -

Fe is ~4 wt% at room temperature [40], but it appears that most of Ni was solid-soluted into Fe without a noticeable segregation. To further examine the effects of Ni addition on the sintering behavior, the microstructure evolution was investigated by sintering the Fe-5Ni pellets at 1150 °C for different times and subsequently water quenching. As expected, the apparent density of Fe-5Ni alloys gradually increased with sintering time (Fig. 4.7) and the residual pores also gradually decreased (Fig. 4.8). The EDS mapping images indicated that Ni was rather locally present at an early stage of sintering, but became homogeneous after the prolonged sintering. At early stage of sintering, the Fe-5Ni alloys exhibited the dual microstructure (large grain size in Ni-poor region and fine grain size in Ni-rich region) implying that Ni inhibited the grain growth of Fe. After prolong sintering, Ni became homogeneously distributed and the grain size also became uniform.

In FAS, Fe-Ni powder is highly conductive, and thus current can flow from the top to the bottom of the lateral surface even if boron nitride powder is present. The results indicated that the densification was remarkably improved in all the compositions after FAS (Fig. 4.2). Then, the densification was remarkably improved in all the compositions (Fig. 4.2). Similar to CS, the sintered density rapidly increased at low Ni content and it was gradually saturated and reached 7.91 g/cm<sup>3</sup> (99.8% relative density) at 5 wt% Ni addition (designated as FAS-1000). The enhanced densification by FAS has been attributed to self-heat generation by the microscopic discharge between the particles, activation of the particle surface, and high mass and heat transfer during the sintering process [9-14]. FAS removed most of the large pores observed in CS and resulted in the dense microstructure. Compared to CS, the grain growth was significantly inhibited and thus, the sintered pure Fe

specimen showed the average grain size of  $\sim 40 \mu\text{m}$  (Fig. 4.4(b)). With the addition of Ni, the grain growth was further inhibited and the smaller grains of  $1\sim 5 \mu\text{m}$  size locally appeared and the portion of smaller grains increased with increasing Ni content (Fig. 4.9). At 5 wt% Ni addition, the alloy exhibited the dual microstructure composed of larger-sized grains in Ni-poor region and smaller-sized grains in Ni-rich region (Fig. 4.6(b) and Fig. 4.10).

To compare the densification and microstructure, the Fe-5Ni alloys were also fabricated by CS (designated as CS-1000) and HP (designated as HP-1000) methods, which were sintered at  $1000 \text{ }^\circ\text{C}$  for 10 min with the heating/cooling rate of  $100 \text{ }^\circ\text{C}/\text{min}$ . As shown in Fig. 4.11, no noticeable densification was observed in the CS-1000 specimen ( $7.24 \text{ g}/\text{cm}^3$ , 91.3 % relative density), which exhibited the porous microstructure (Fig. 4.12(a)) similar to that of Fe-5Ni alloy sintered at  $1150 \text{ }^\circ\text{C}$  for 0 min by CS (Fig. 4.8(a)). The sintered density of HP-1000 was  $7.73 \text{ g}/\text{cm}^3$  (97.4% relative density), which was lower than that of FAS-1000 (Fig. 4.11). It indicated that the electric current along with mechanical pressure played an important role for the densification. Similar to the FAS-1000 (Fig. 4.6(b)), the HP-1000 specimen showed the dual microstructure (Fig. 4.12(b)), but the grains in Ni-poor region were much larger and the Ni distribution was much localized, implying that the electric current in FAS promoted the Ni diffusion possibly along the grain boundaries and enhanced the densification. In addition, the Ni-rich region with smaller grains was mainly observed in the specimens with a short sintering time. The effect of mechanical pressure on densification of Fe-5Ni alloys was further supported by FAS. As the pressure increased from  $38\sim 69 \text{ MPa}$ , the ratio of grain growth slightly

decreased (Fig. 4.13), and the area fraction of Ni-rich region gradually increased and reached 19.5 % (Fig. 4.14). As a result, the apparent density and bulk-hardness were sharply increased and finally saturated to the full densification (Fig. 4.14). It was because that more contacts between particles induced to be transformed into Ni-rich phases with increasing the pressure. This results indicated that mechanical pressure during sintering was effective to eliminate the pores, and increased the particle contacts to change the constituent phases.

To examine the relationship between Ni distribution and grain size, the FAS-1000 alloy was post annealed at 1150 °C for 120 min (designated as FAS-1000P), and its microstructure was observed by SEM with an EDS mapping (Fig. 4.12(c)). After post-annealing, the apparent density slightly decreased from 7.91 to 7.86 g/cm<sup>3</sup> (Fig. 4.15), but the grain size became uniform (~30 μm) and the Ni distribution also became homogeneous. It is speculated that Ni diffusion occurred from Ni-rich region to Ni-poor region and grain growth concurrently occurred in Ni-rich region resulting in the uniform microstructure with a homogeneous Ni distribution after prolonged sintering time.

To further investigate the Ni-rich region of FAS-1000 alloy, the cross sectional specimen was prepared by focused ion beam (FIB) technique and observed by TEM. The low magnification high angle annular dark field (HAADF)-scanning TEM (STEM) images showed that the average grain size in Ni-rich region was ~3 μm (Fig. 4.16(a)) and the selected area electron diffraction (SAED) patterns indicated that all the grains were α-Fe with a BCC structure (Fig. 4.16(b)-(d)) [41,42]. No intermetallic compound formation was confirmed. The EDS mapping and line scan

results indicated that most of Ni was present at the grain boundaries (Fig. 4.16(a) and (e)). This observation indicated that Ni was rapidly diffused along the grain boundaries during FAS, which can be attributed to the field or current effects in FAS. Similar results have been reported in other systems, which can be attributed to the synergistic effect of Joule heating and electromigration [9-13,16-18].

The grain boundary diffusion of Ni was further investigated by comparing the microstructure of Fe-Ni diffusion couples sintered by CS (1150 °C for 120 min), HP (1000 °C for 10 min) and FAS (1000 °C for 10 min) (Fig. 4.17). The SEM micrograph and EDS elemental mapping image of the diffusion couple sintered by CS and HP showed that Ni was uniformly diffused across the Fe-Ni interface (Fig. 4.17(a) and Fig. 4.17(b)). On the other hand, Ni was rapidly diffused along the grain boundaries in the diffusion couple sintered by FAS (Fig. 4.17(c)). These observations indicated that the electric current along with mechanical pressure in FAS promoted the Ni diffusion along the grain boundaries, which resulted in the enhanced densification with suppressed grain growth. Previous studies also supported our findings that FAS enhanced the mass transportation [24,25]. In Fe-Al diffusion couple, the interdiffusion coefficient of Fe-Al diffusion couple under pulsed current was about 46 times higher than that without a current [24]. In W-Ti system, the interdiffusion coefficient during spark plasma sintering was higher than that of the traditional sintering [25]. Therefore, the enhanced diffusion can be explained by combined surface diffusion and grain boundary diffusion under FAS condition.

The Rockwell hardness of Fe-xNi alloys sintered by CS, FAS, and HP is shown in Fig. 4.18 and Fig. 4.19 as a function of Ni content. The variation of hardness with

Ni content was very similar to that of apparent density with Ni content (Fig. 1 and Fig. 4.15), that is, the bulk hardness gradually increased with increasing the Ni content and the hardness of the specimens sintered by FAS was higher than those by CS and HP. Thus, the fully densified Fe-5Ni sintered by FAS exhibited the highest bulk hardness of HRA 53 (HRC 13.3) (Fig. 4.19). These values were in good agreement with previous studies (converted value) of ferrite alloys [43,44]. The increased hardness in this study can be attributed to the higher apparent density, reduced grain size [45]. Meanwhile, the apparent density of Fe-5Ni alloys sintered by CS and HP was similar, but the bulk hardness of Fe-5Ni alloys sintered by HP was high than that by CS, which can be attributed to the smaller grain size in Ni-rich region of Fe-5Ni alloys sintered by HP. In addition, it is expected that the other mechanical properties such as tensile strength can be improved by the addition of Ni, possibly due to the increased sintered density and solid solution strengthening [46].

#### **4.4. Conclusions**

In this work, the Fe-Ni alloys were fabricated by CS, FAS, and HP methods and their densification, microstructure, and elemental distribution were compared to elucidate the field (or current) effect on the densification in FAS technology. The Ni addition and FAS method enhanced the densification and inhibited the grain growth of Fe-Ni alloys. Thus, a nearly fully densified Fe-Ni alloy was obtained by employing the FAS method with 5 wt% Ni addition. The Ni distribution determined by EDS indicated that Ni was locally present at the early stage of sintering in CS and

became homogeneous throughout the specimen with increasing the sintering time. However, Ni was mainly located along the grain boundaries in the fully densified FAS specimen, which resulted in a dual microstructure composed of larger-sized grains in Ni-poor region and smaller-sized grains in Ni-rich region. The Fe-Ni diffusion couple experiment demonstrated that Ni was uniformly diffused across the interface in the diffusion couple sintered by CS, but Ni was rapidly diffused along the grain boundaries in the diffusion couple sintered by FAS. Consequently, the electric current along with mechanical pressure in FAS enhanced the Ni diffusion along the grain boundaries, facilitated the densification, and inhibited the grain growth, which resulted in the improved mechanical properties (bulk hardness).

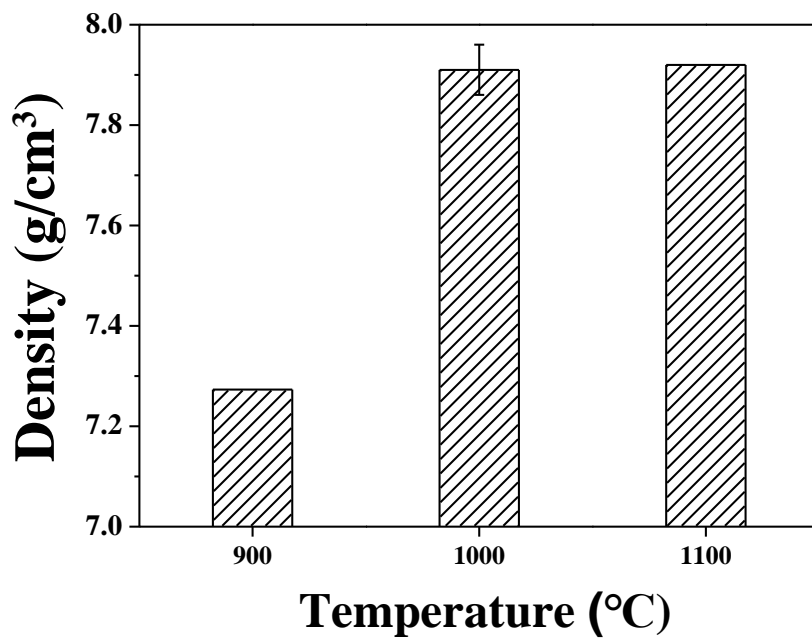


**Figure. 4.1.** Sintered density of Fe-5Ni alloys prepared by FAS method depending on the sintering temperature.

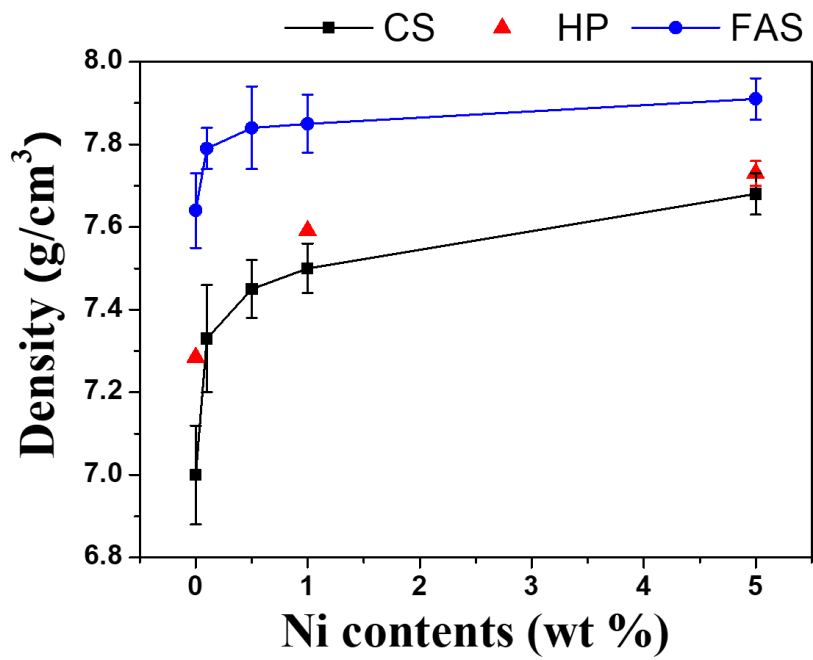


**Figure 4.2.** Apparent density of Fe-xNi alloys sintered by CS, HP and FAS as a function of Ni contents ( $x = 0\sim 5$  in wt%).

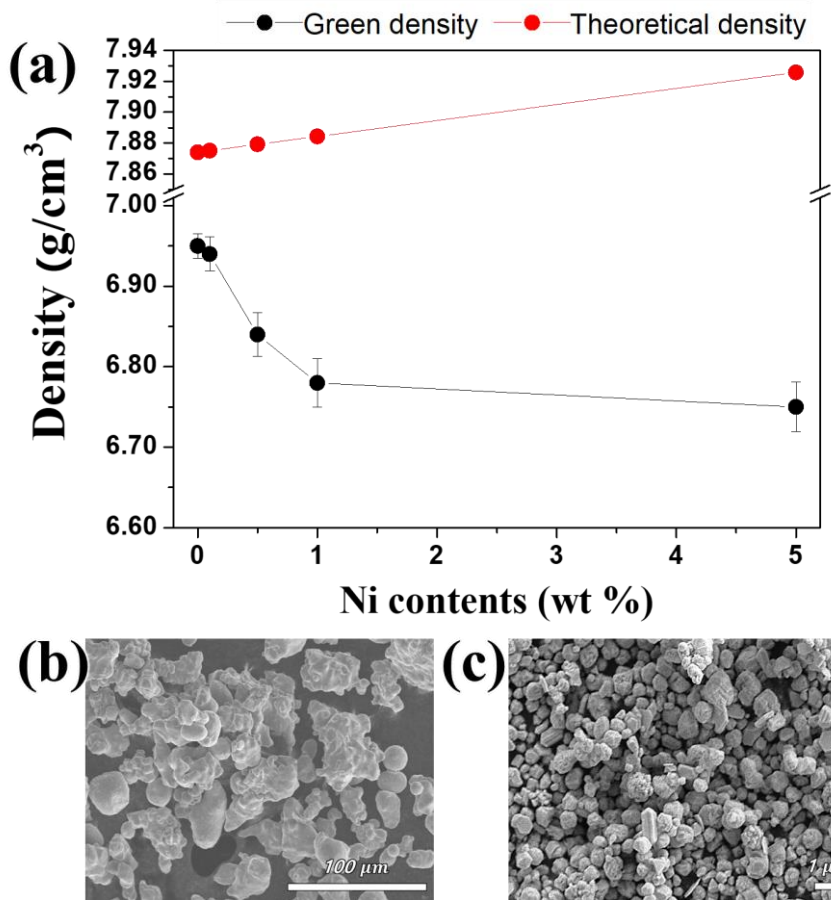


**Figure 4.3.** (a) Green and theoretical densities of Fe-Ni alloys as a function of Ni content, and FE-SEM images of (b) Fe and (c) Ni starting powder

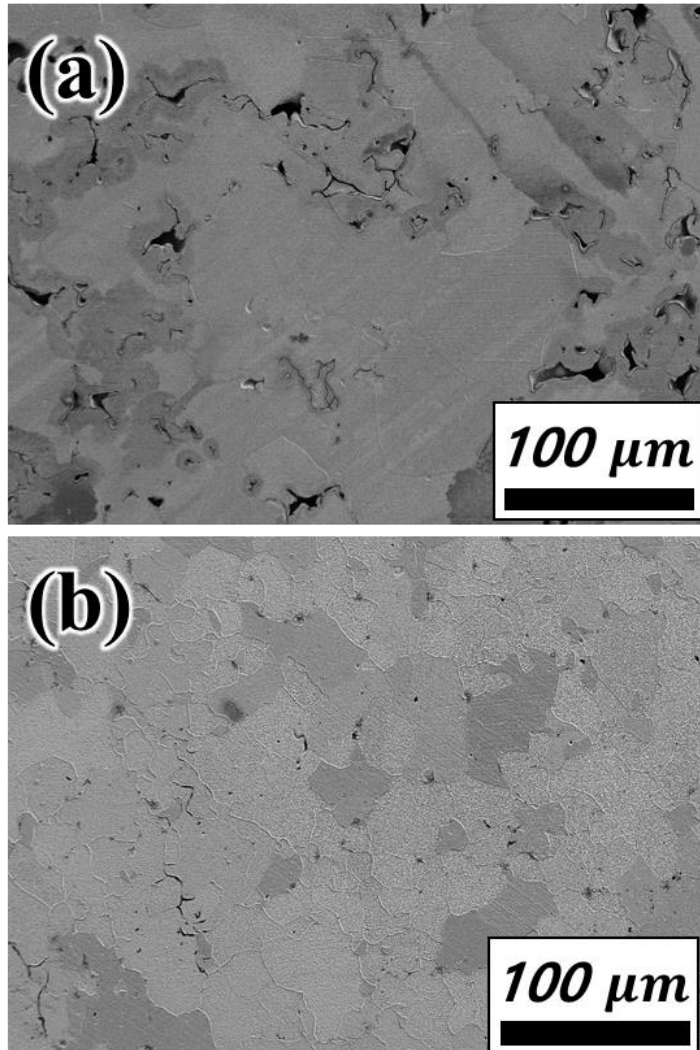


**Figure 4.4.** FE-SEM micrographs of pure Fe sintered by (a) CS and (b) FAS.

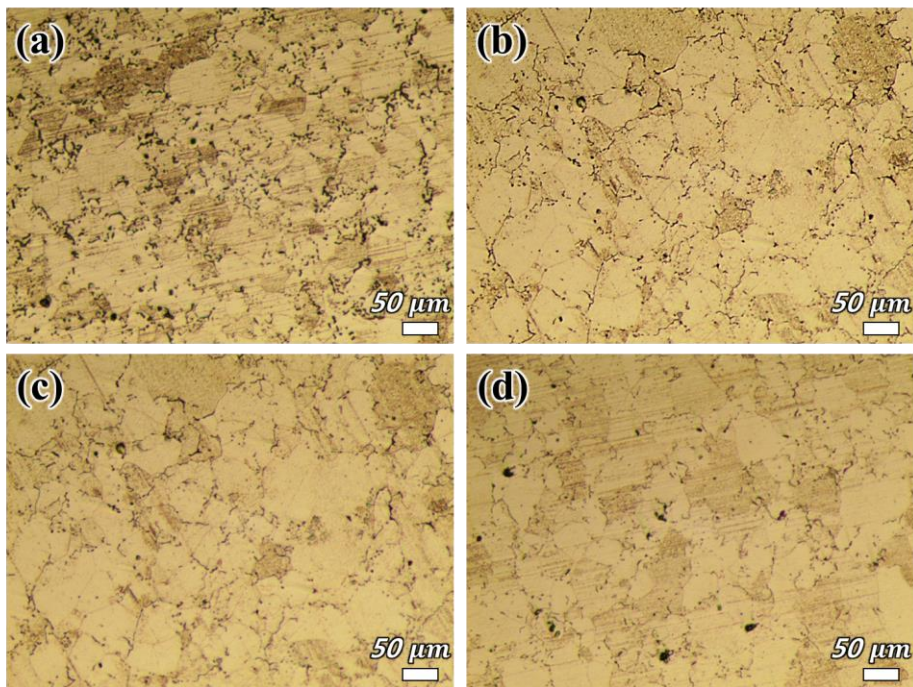


**Figure 4.5.** Optical micrographs of conventionally sintered Fe-xNi alloys. ((a)  $x = 0.1$ , (b)  $x = 0.5$ , (c)  $x = 1$  and (d)  $x = 5$ ).

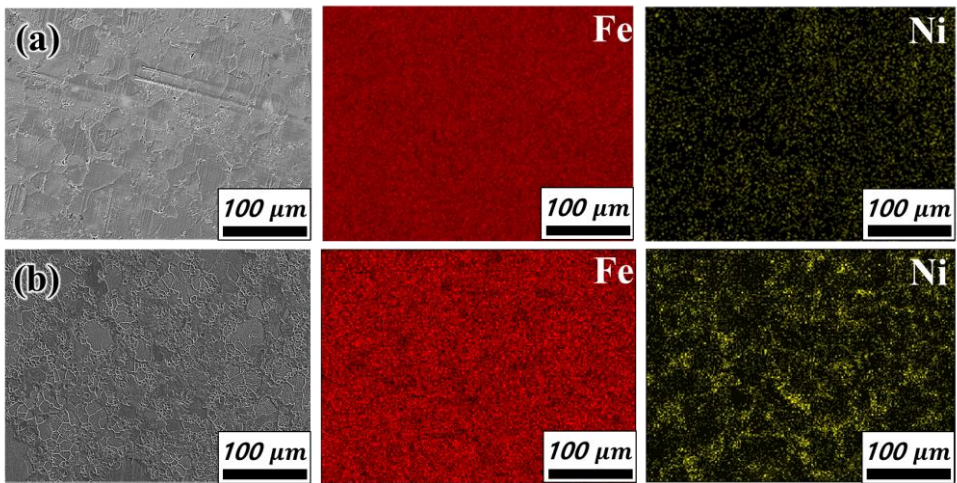


**Figure 4.6.** FE-SEM micrographs and EDS mapping images of Fe-5Ni alloys sintered by (a) CS and (b) FAS.

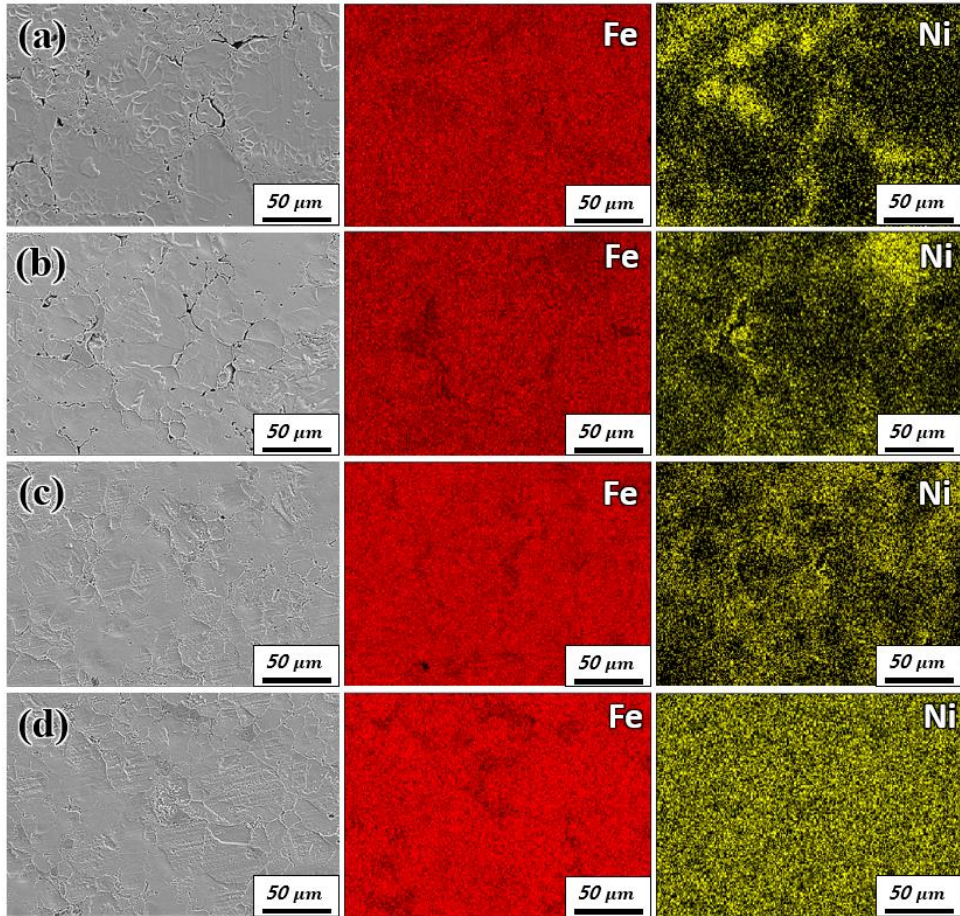


**Figure 4.7.** SEM micrographs and EDS mapping images of Fe-5Ni alloys, which were sintered at 1150 °C for (a) 0 min, (b) 30 min, (c) 60 min, and (d) 120 min and water-quenched.

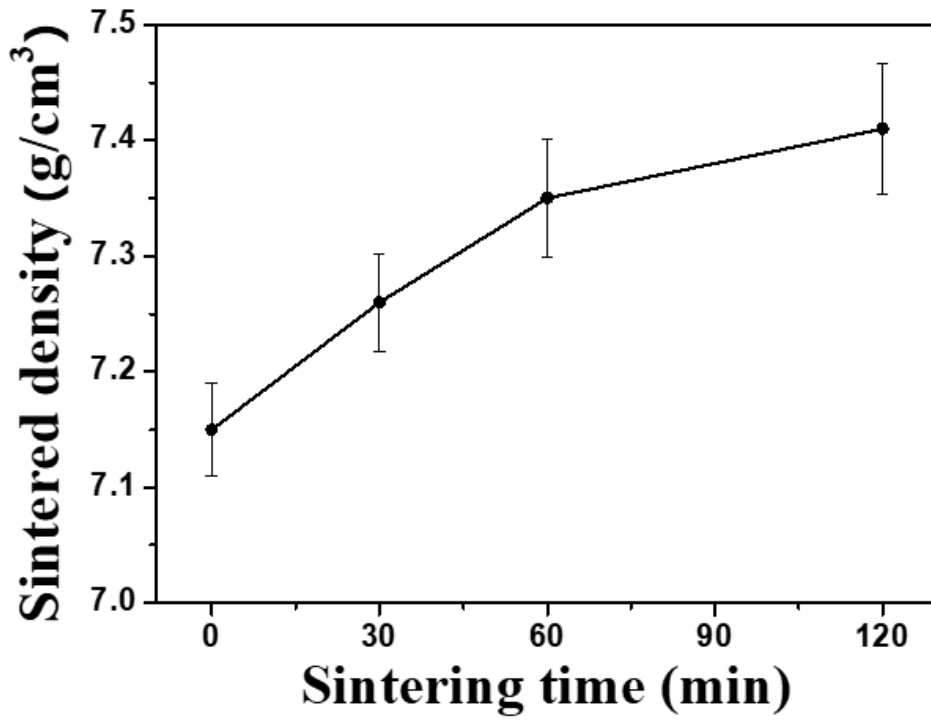


**Figure 4.8.** Sintered densities of Fe-5Ni alloys which were sintered at 1150 °C for 0~120 min and water-quenched.

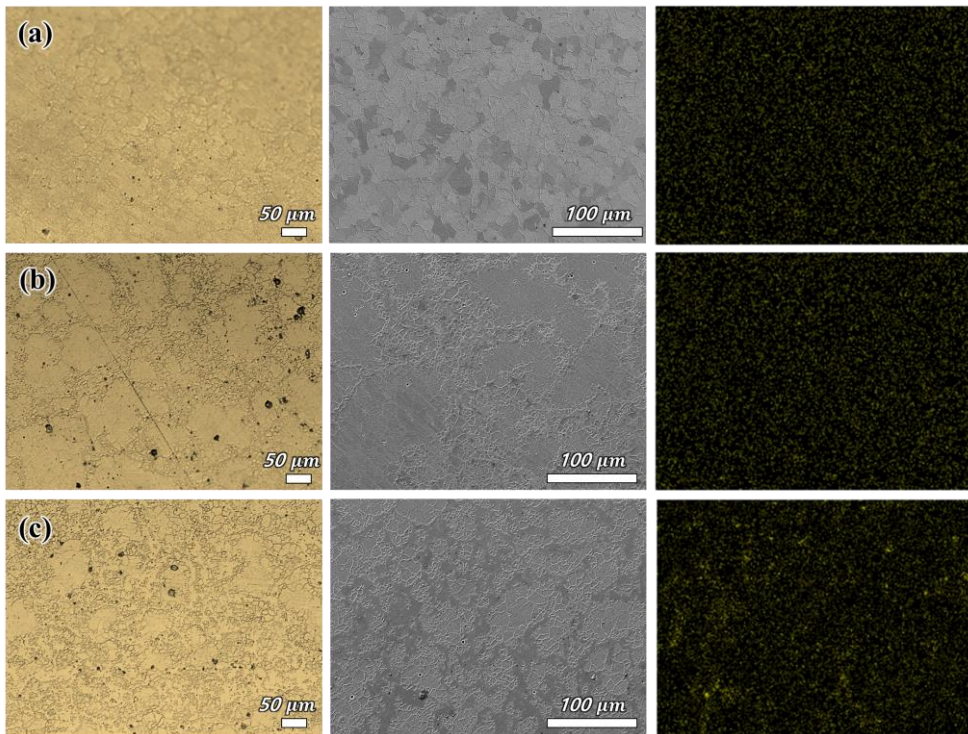


**Figure 4.9.** OM, FE-SEM and EDS mapping images of Fe-xNi alloys. (a)  $x = 0.1$ ,  
(b)  $x = 0.5$  and (c)  $x = 1$  consolidated by FAS.

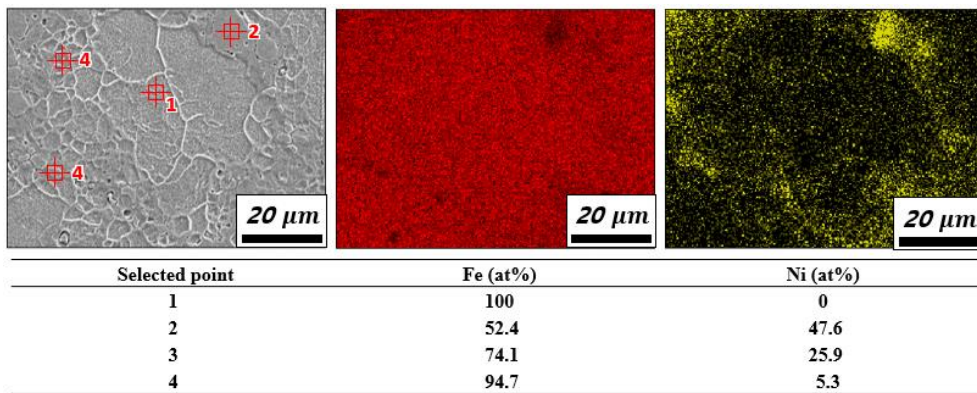


**Figure 4.10.** SEM micrographs and EDS mapping images of Fe-5Ni alloy fabricated by FAS, and chemical compositions (at%) of selected points.

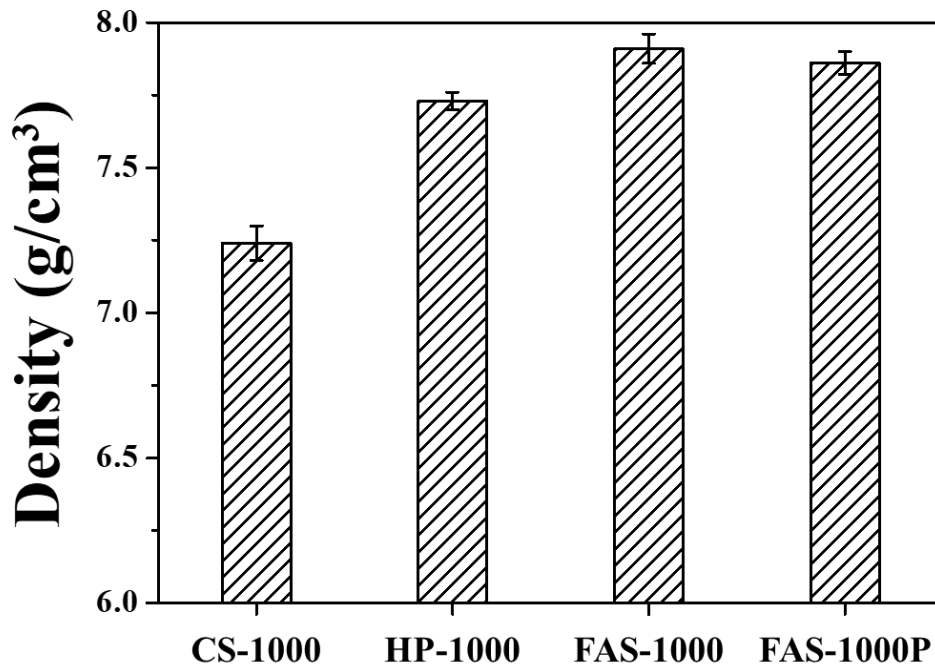


**Figure 4.11.** (a) Apparent density of CS-1000, HP-1000, FAS-1000, and FAS-1000P alloys

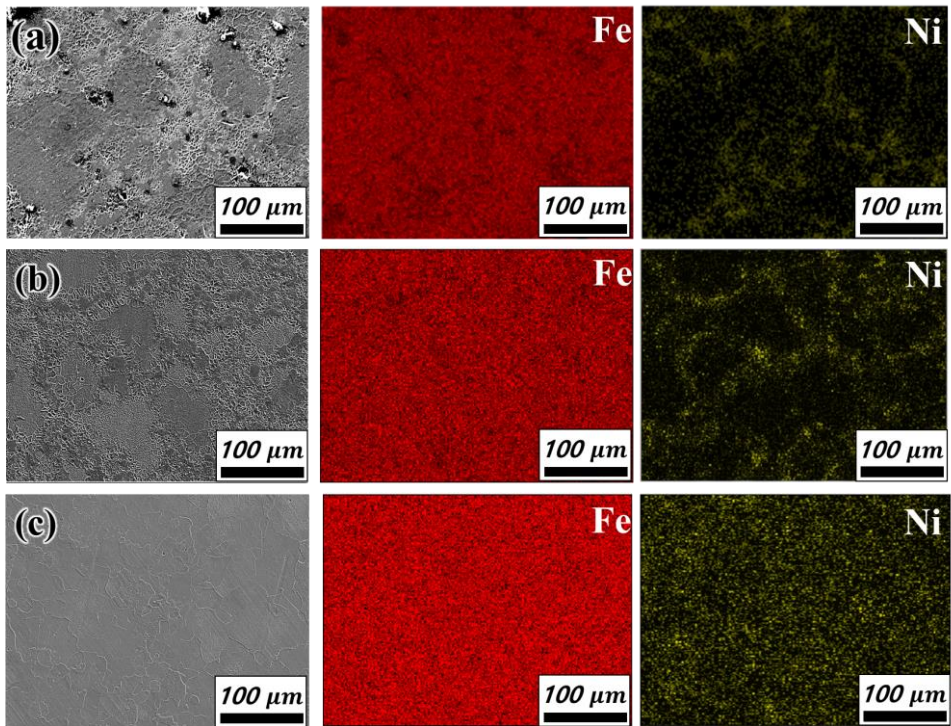


**Figure 4.12.** FE-SEM micrographs and EDS mapping images of (a) CS-1000, (b) HP-1000, and (c) FAS-1000P alloys.

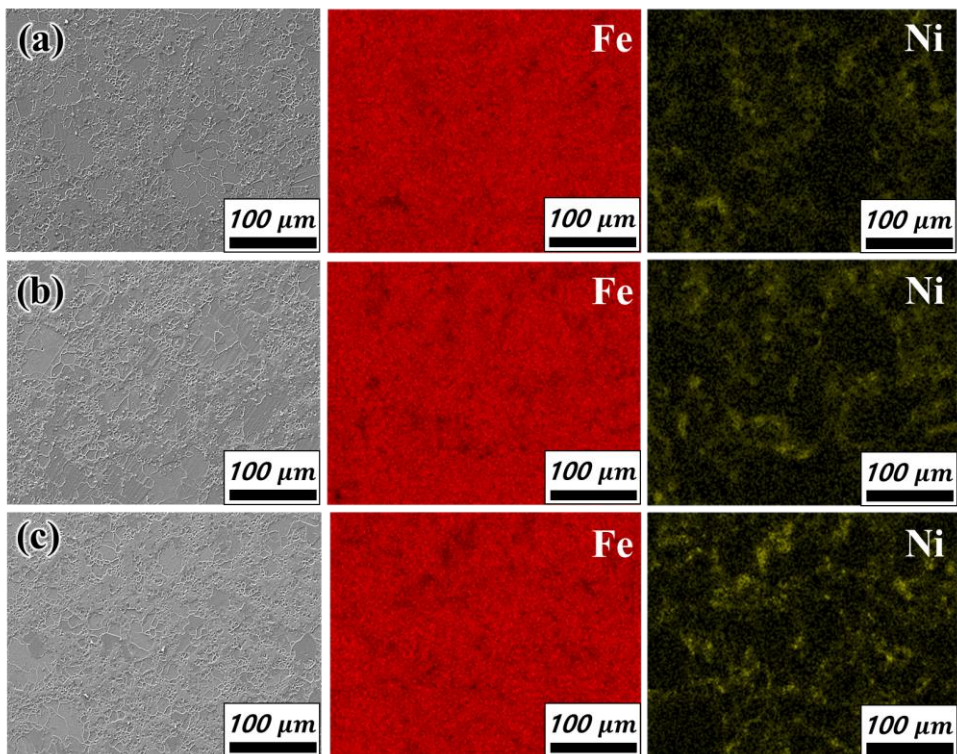


**Figure 4.13.** FE-SEM images of Fe-5Ni alloys as a function of mechanical pressure: (a) 37.7 MPa, (b) 45 MPa and (c) 68.8 MPa.

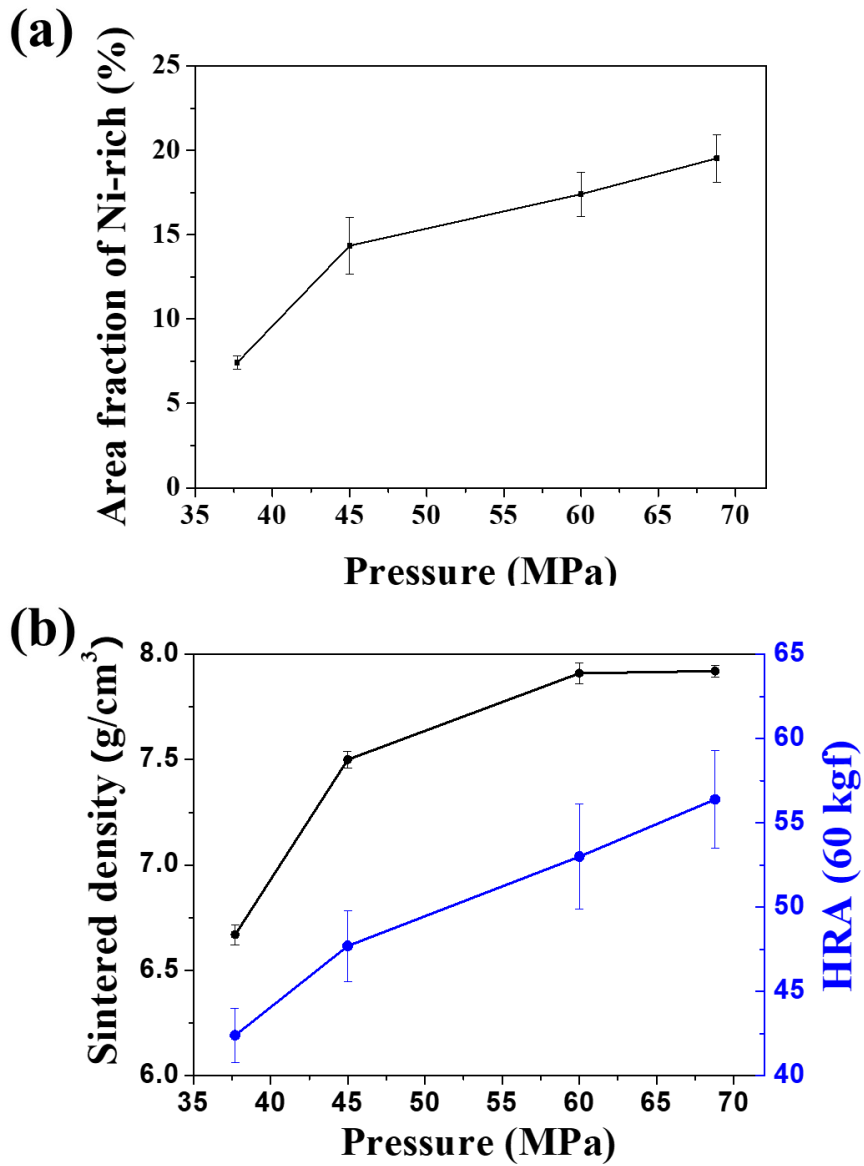


**Figure 4.14.** (a) The area fraction of Ni-rich phases in Fe-5Ni alloys as a function of mechanical pressure, and thier (b) apparent densities and bulk hardness.

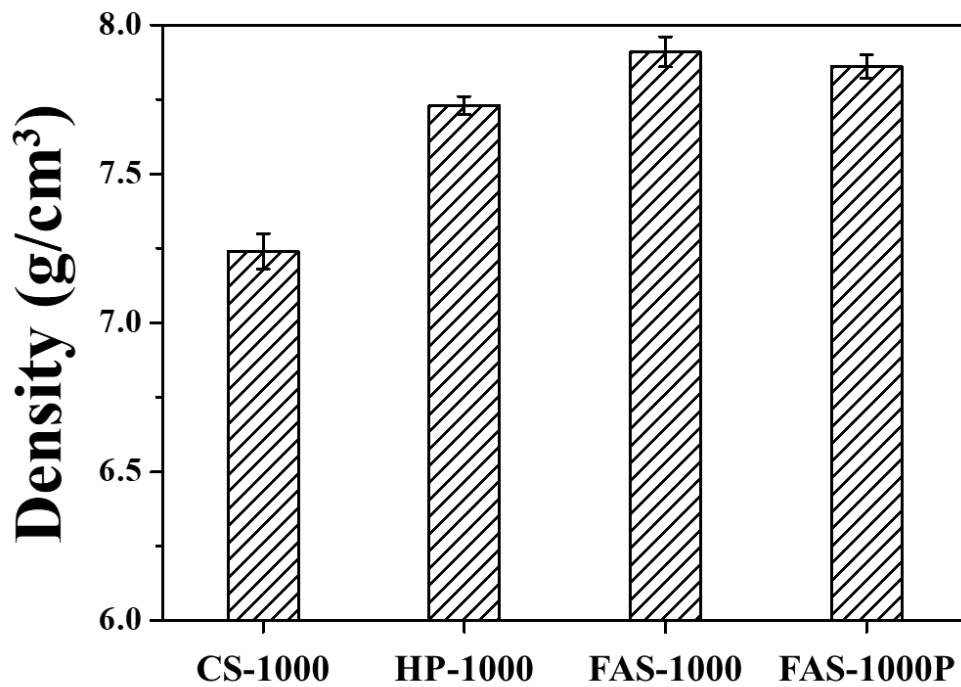


**Figure 4.15.** Apparent density of CS-1000, HP-1000, FAS-1000, and FAS-1000P alloys

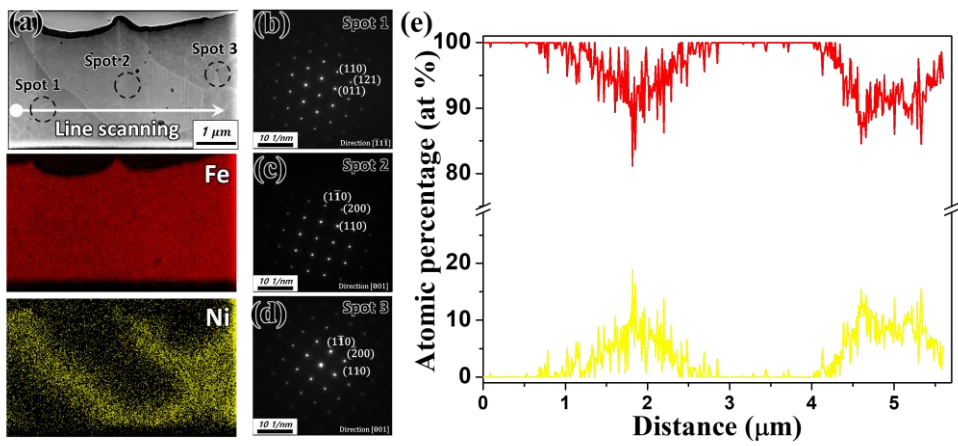


**Figure 4.16.** (a) Low magnification HAADF-STEM and EDS mapping images of fine grains (Ni-rich region), and selected area diffraction patterns (SADPs) of (b) spot 1, (c) spot 2, and (d) spot 3, and (e) EDS line scanning profile across the specimen as marked by the line.

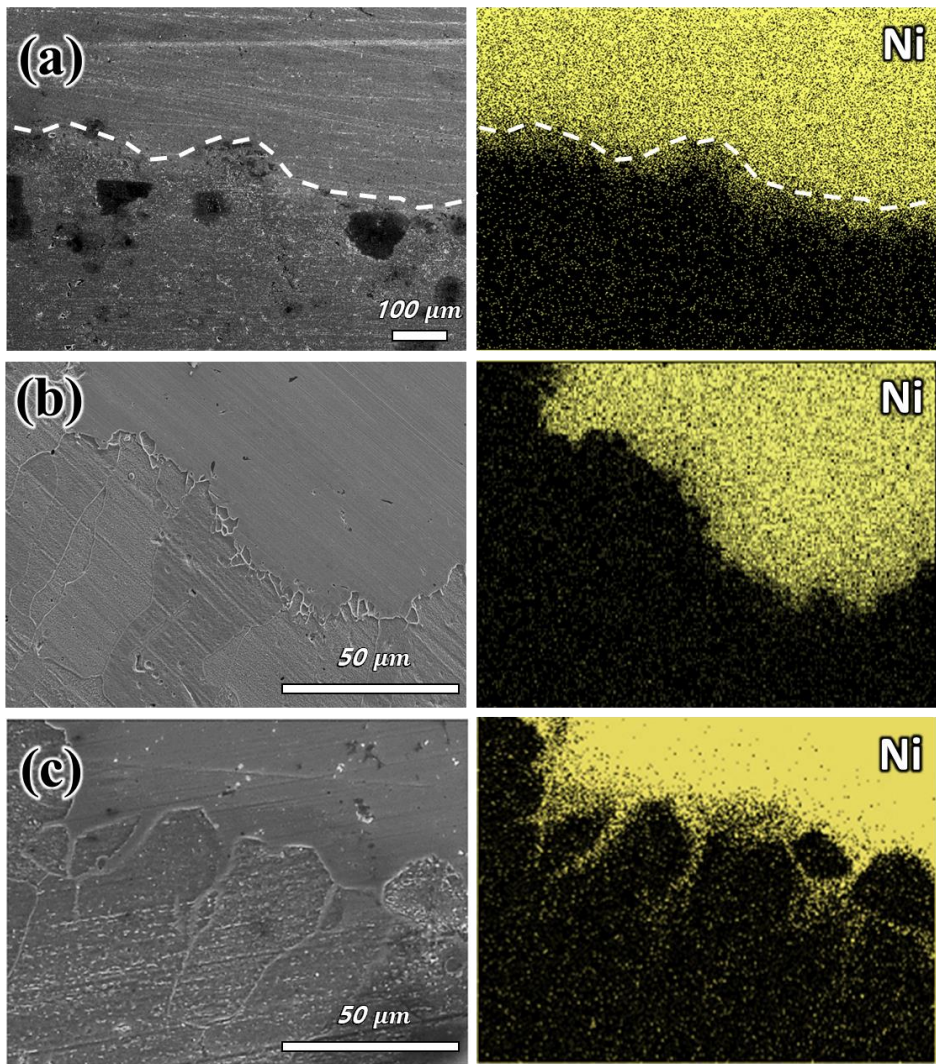


**Figure 4.17.** The cross-sectional images of simple Fe-Ni diffusion couples prepared by (a) CS (1150 °C for 120 min), (b) HP (1000 °C for 10 min) and (c) FAS (1000 °C for 10 min) with their elemental mapping of Ni K.

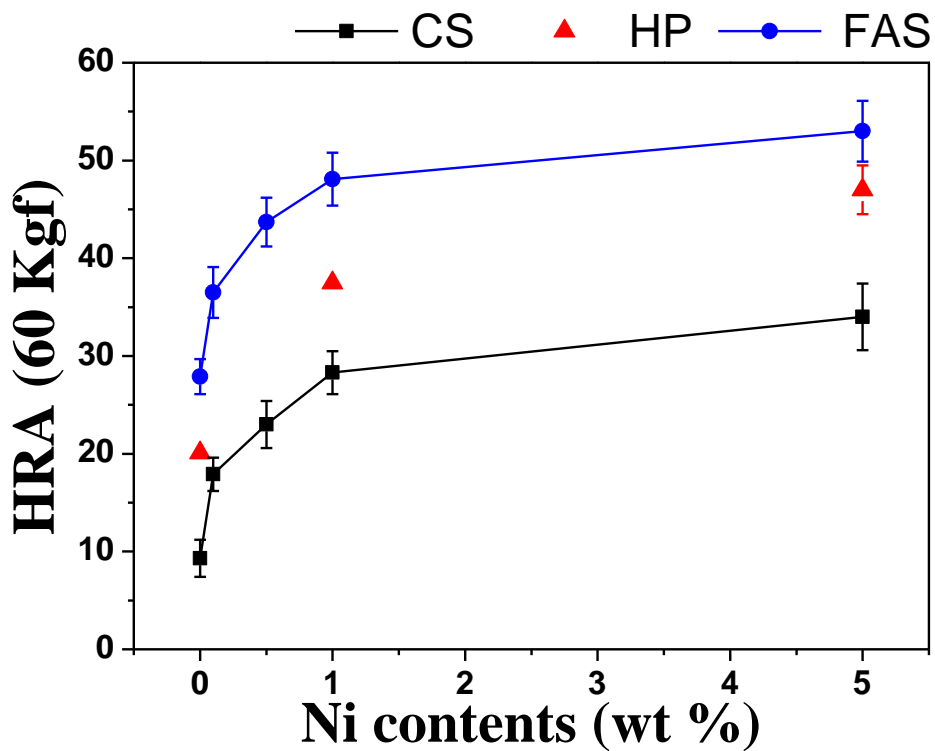


**Figure 4.18.** Rockwall A hardness of Fe-xNi alloys sintered by CS, HP and FAS as a function of Ni contents ( $x = 0\sim 5$  in wt%).

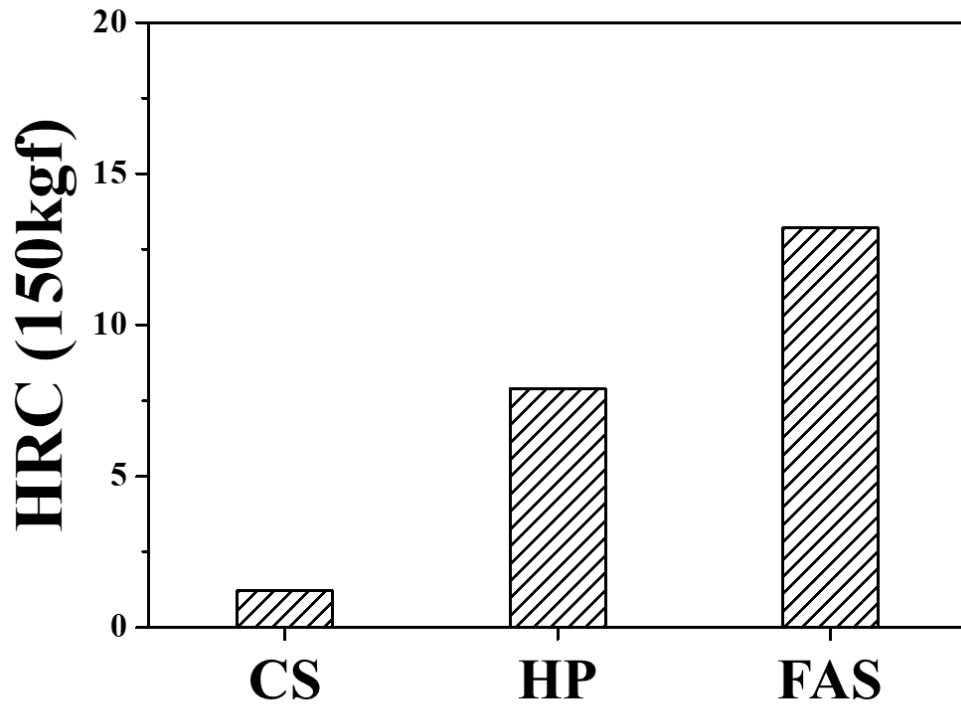


**Figure 4.19.** Rockwall A hardness of Fe-xNi alloys sintered by CS, HP and FAS as a function of Ni contents ( $x = 0\sim 5$  in wt%).

## Reference

- [1] K.S. Narasimhan, Sintering of powder mixtures and the growth of ferrous powder metallurgy, *Mater. Chem. Phys.* 67 (2001) 56-65.
- [2] A. Hadrboletz, B. Weiss, Fatigue behaviour of iron based sintered material: a review, *Int. Mater. Rev.* 42 (1997) 1-44.
- [3] B. Zhang, N. Fenineche, L. Zhu, H. Liao, C. Coddet, Studies of magnetic properties of permalloy (Fe-30%Ni) prepared by SLM technology, *J. Magn. Magn. Mater.* 324 (2012) 495-500.
- [4] J.-S. Lee, B.-H. Cha, Y. -S. Kang, Processing of net-shaped nanocrystalline Fe-Ni material, *Adv. Eng. Mater.* 7.6 (2005) 467-473.
- [5] Y. Xie, H. Cheng, Q. Tang, W. Chen, W. Chen, P. Dai, Effects of N addition on microstructure and mechanical properties of CoCrFeNiMn high entropy alloy produced by mechanical alloying and vacuum hot pressing sintering, *Intermetallics* 93 (2018) 228-234.
- [6] P. Guyot, G. Antou, N. Pradeilles, A. Weibel, M. Vandenhende, G. Chevallier, A. Peigney, C. Estournès, A. Maître, Hot pressing and spark plasma sintering of alumina: Discussion about an analytical modelling used for sintering mechanism determination, *Scr. Mater.* 84-85 (2014) 35-38.
- [7] H.V. Atkinson, S. Davies, Fundamental aspects of hot isostatic pressing: An overview, *Metall. Mater. Trans. A* 31 (2000) 2981-3000.
- [8] M.H. Bocanegra-Bernal, Hot Isostatic Pressing (HIP) technology and its

- applications to metals and ceramics, *J. Mater. Sci.* 39 (2004) 6399-6420.
- [9] E.A. Olevsky, W.L. Bradbury, C.D. Haines, D.G. Martin, D. Kapoor, Fundamental aspects of spark plasma sintering: I. Experimental Analysis of Scalability, *J. Am. Ceram. Soc.* 95 (2012) 2406-2413.
- [10] O. Guillon, J. Gonzalez-Julian, B. Dargatz, T. Kessel, G. Schierning, J. Räthel, M. Herrmann, Field-assisted sintering technology/Spark plasma sintering: mechanisms, materials, and technology developments, *Adv. Eng. Mater.* 16 (2014) 830-849.
- [11] S.R. Oke, O.O. Ige, O.E. Falodun, A.M. Okoro, M.R. Mphahlele, P.A. Olubambi, Powder metallurgy of stainless steels and composites: a review of mechanical alloying and spark plasma sintering, *Int. J. Adv. Manuf. Tech.* 102 (2019) 3271-3290.
- [12] N. Saheb, Z. Iqbal, A. Khalil, A. S. Hakeem, N.A. Aqeeli, T. Laoui, A.-Q.R. Kirchner, Spark plasma sintering of metals and metal matrix nanocomposites: A review, *J. Nanomater.* 2012 (2012) 1-13.
- [13] Z.A. Munir, U. Anselmi-Tamburini, M. Ohyanahi, The effect of electric field and pressure on the synthesis and consolidation of materials: A review of the spark plasma sintering method, *J. Mater. Sci.* 41 (2006) 763-777.
- [14] Z.-H. Zhang, Z.-F. Liu, J.-F. Lu, X.-B. Shen, F.-C. Wang, Y.-D. Wang, The sintering mechanism in spark plasma sintering – Proof of the occurrence of spark discharge, *Scr. Mater.* 81 (2014) 56-59.
- [15] D.M. Hulbert, A. Anders, D.V. Dudina, J. Anderson, D. Jiang, C. Unuvar, U.

- Anselmi-Tamburini, E.J. Lavernia, A.K. Mukherjee, The absence of plasma in “spark plasma sintering”, *J. Appl. Phys.* 104 (2008) 033305.
- [16] M. Demuyne, J.-P. Erauw, O.V.D. Biest, F. Delannay, F. Cambier, Densification of alumina by SPS and HP: A comparative study, *J. Euro. Ceram. Soc.* 32 (2012) 1957-64.
- [17] G. Lee, J. Mckittrick, E. Ivanov, E.A. Olevsky, Densification mechanism and mechanical properties of tungsten powder consolidated by spark plasma sintering, *Int. J. Refract. Metals. Hard Mater.* 61 (2016) 22-29.
- [18] M.-J. Kim, S. Yoon, S. Park, H.-J. Jeong, J.-W. Park, K. Kim, J. Jo, T. Heo, S.-T. Hong, S.H. Cho, Y.-K. Kwon, I.-S. Choi, M. Kim, H.N. Han, Elucidating the origin of electroplasticity in metallic materials, *Appl. Mater. Today* 21 (2020) 100874.
- [19] A.S. Sharma, S. Yadav, K. Biswas, B. Basu, High-entropy alloys and metallic nanocomposites: Processing challenges, microstructure development and property enhancement, *Mater. Sci. Eng. R Rep.* 131 (2018) 1-42.
- [20] G. Bernard-Granger, C. Guizard, Spark plasma sintering of a commercially available granulated zirconia powder: I. Sintering path and hypotheses about the mechanism(s) controlling densification, *Acta Mater.* 55 (2007) 3493-3504.
- [21] J. Trapp, A. Semenov, M. Nothe, T. Wallmersperger, B. Kieback, Fundamental principles of spark plasma sintering of metals: part III – densification by plasticity and creep deformation, *Powder Metall.* 63 (2020) 329-337.
- [22] W. Li, F. Zeng, L. Li, Z. Wang, H. Liu, Y. Peng, Y. Gu, Spark plasma sintering

- of Ti–1Al–8V–5Fe alloy: densification mechanism and grain growth, *Appl. Phys. A* 126 (2020) 709
- [23] K. Vasanthakumar, S.R. Bakshi, Effect of C/Ti ratio on densification, microstructure and mechanical properties of TiC<sub>x</sub> prepared by reactive spark plasma sintering, *Ceram. Int.* 44 (2018) 484-494.
- [24] R. Li, T. Yuan, X. Liu, K. Zhou, Enhanced atomic diffusion of Fe–Al diffusion couple during spark plasma sintering, *Scr. Mater.* 110 (2016) 105-108.
- [25] S. Deng, T. Yuan, R. Li, M. Zhang, S. Xie, M. Wang, L. Li, J. Yaun, Q. Weng, Influence of electric current on interdiffusion kinetics of W-Ti system during spark plasma sintering, *Int. J. Refract. Metals. Hard. Mater.* 75 (2018) 184-190.
- [26] W. Shen, L. Yu, H. Liu, Y. He, Z. Zhou, Q. Zhang, Diffusion welding of powder metallurgy high speed steel by spark plasma sintering, *J. Mater. Process. Tech.* 275 (2020) 116383.
- [27] B. Cheng, R. Bao, J. Ti, C. Li, J. Tao, Y. Liu, S. Tan, X. You, Interface optimization of CNT/Cu composite by forming TiC nanoprecipitation and low interface energy structure via spark plasma sintering, *J. Alloys. Compd.* 722 (2017) 852-858.
- [28] F. Czerwinski, Diffusion annealing of Fe–Ni alloy coatings on steel substrates, *J. Mater. Sci.* 33 (1998) 3831-3837.
- [29] L. Zhang, D. Sun, H. Yu, H. Li, Characteristics of Fe-based alloy coating produced by plasma cladding process, *J. Mater. Sci. Eng. A*32 (2007) 319-324.

- [30] R.A. DePaul, A.L. Kitchin, The role of nickel, copper, and columbium (Niobium) in strengthening a low-carbon ferritic steel, *Metall. Mater. Trans. B1* (1970) 389-393.
- [31] B. Zhang, N.-E. Fenineche, H. Liao, C. Coddet, Magnetic properties of in-situ synthesized FeNi<sub>3</sub> by selective laser melting Fe-80%Ni powders, *J. Magn. Magn. Mater.* 336 (2013) 49-54.
- [32] T.-Y. Chan, S.-T Lin, Sintering of elemental carbonyl iron and carbonyl nickel powder mixtures, *J. Mater. Sci.* 32 (1997) 1963-1967.
- [33] H. Zhang, R.M. German, Homogeneity and properties of injection moulded Fe-Ni alloys, *Met. Powder Rep.* 56 (2001) 18-22.
- [34] M.B. Shongwe, S. Diouf, M.O. Durowoju, P.A. Olubambi, Effect of sintering temperature on the microstructure and mechanical properties of Fe-30%Ni alloys produced by spark plasma sintering, *J. Alloys. Compd.* 649 (2015) 824-832.
- [35] M.B. Shongwe, M.M. Ramakokovhu, S. Diouf, M.O. Durowoju, B.A. Obadele, R. Sule, M.L. Lethabane, P. A. Olubambi, Effect of starting powder particle size and heating rate on spark plasma sintering of Fe-Ni alloys, *J. Alloys. Compd.* 678 (2016) 241-248.
- [36] I.M.C. Bopape, M.B. Shongwe, E.N. Ogunmuyiwa, A.L. Rominiyi, S.O. Jeje, Influence of heat treatment on microstructure and mechanical properties of Ni-Fe-Co ternary alloy prepared via spark plasma sintering, *Conference of the South African Advanced Materials Initiative (CoSAAMI2019)* (2019).

- [37] C. Gorynski, U. Anselmi-Tamburini, M. Winterer, Controlling current flow in sintering: A facile method coupling flash with spark plasma sintering, *Rev. Sci. Instrum* 91 (2020) 015112.
- [38] U. Anselmi-Tamburini, S. Gennari, J.E. Garay, Z.A. Munir, Fundamental investigations on the spark plasma sintering/synthesis process: II. Modeling of current and temperature distributions, *Mater. Sci. Eng. A* 394 (2005) 139-148.
- [39] S.-X. Song, Z. Wang, G.-P. Shi, Heating mechanism of spark plasma sintering, *Ceram. Int.* 39 (2013) 1393-1396.
- [40] K.B. Reuter, D.B. Williams, J.I. Goldstein, Determination of the Fe-Ni phase diagram below 400 °C, *Metall. Mater. Trans. A* 20 (1989) 719-725.
- [41] J. Zhang, X. Hu, K. Chou, In-situ environmental transmission electron microscopy investigation of the phase transformation austenite → ferrite in duplex stainless steel, *Mater. Lett.* 264 (2020) 127259.
- [42] Y. Yang, L. Liu, Y. Zhang, C. Song, Q. Zhai, Structure and Phase Transition of Fe-Mn Alloy Powders Prepared by Gas Atomization, *Mater. Res.* 18 (2015) 10-19.
- [43] J.C. Rawers, R.C. Doan, Mechanical processing of iron powders in reactive and nonreactive gas atmospheres, *Metall. Mater. Trans. A* 25 (1994) 381-388.
- [44] E.C. Buc, S.K. Putatunda, R.Naik, soft magnetic properties of Fe-5 wt% Al alloy, *Mater. Manuf. Process.* 23 (2008) 289-294.
- [45] H. Kotan, K.A. Darling, M. Saber, Thermal stability and mechanical properties

of nanocrystalline Fe–Ni–Zr alloys prepared by mechanical alloying, *J. Mater. Sci.* 48 (2013) 8402-8411.

- [46] B. Wu, Z. Qiu, Z. Pan, K. Carpenter, T. Wang, D. Ding, S.V. Duin, H. Li, Enhanced interface strength in steel-nickel bimetallic component fabricated using wire arc additive manufacturing with interweaving deposition strategy, *J. Mater. Sci. Tech.* 52 (2020) 226-234.

## Abstract in Korean

### 초 록

# 액상 소결 및 통전 활성화 소결 방법으로 제작한 철 계 합금의 미세 구조 개선과 기계적 특성 평가

유진수

서울대학교 공과대학

재료공학부

분말야금기술은 원재료 금속 분말을 사용하여 소결 부품의 최종 형상에 가깝게 제조하여 높은 생산성 및 재료 손실이 최소화하는 장점이 있는 공정 기술이다. 또한, 자동차 소재, 가전제품, 전자제품 등의 범용 기계 소재에 이르기 까지 적용 재료의 범위도 광범위하다. 하지만 철 계 합금은 소결 후 5~15 %의 기공이 존재하여 소결 부품으로의 적용이 제한이 된다. 소결체의 고밀도화를 위해서 액상소결법, 핫프레싱, 통전활성소결과 같은 소결 기술들이 현재 많이 연구가 진행되어왔다. 하지만 철 계 합금은 각각의 소결 방법에서 비롯되는 고유한 미세 구조로 인해 기계적 특성의 향상이 제한적이다. 또한 열처리 도중

미세구조와 소결 거동에 대한 이론적인 연구가 철저히 분석되지 않았다. 이 연구에서는 소결 방법, 소결 조건, 조성, 열 처리 등을 통한 미세구조를 개선이 기계적 특성에 끼치는 영향에 대한 주제로 총 세 가지에 대해 논하고자 한다.

첫 번째 주제로 니켈 (Ni)이 Fe-B-C 합금 시스템에 도입되어 공용반응 온도를 낮춰 붕소 함유 합금의 치밀화를 향상시키고자 하였다. 하지만, 다량의 액상이 입 계에서 공용경질상 (M<sub>23</sub>B<sub>6</sub>, M<sub>3</sub>B, M<sub>2</sub>B)의 연속 네트워크를 생성하기 때문에 액상소결에서는 연신 특성의 향상이 매우 제한적이다. 이를 극복 하기 위해, 합금의 조성을 제어하여 응고상의 부피 분율을 최적화하고 펄라이트 매트릭스로 응고 된  $\alpha$ -Fe 입자의 조 대화를 사후 열처리에 의해 공용상의 연속 네트워크를 줄이고 입자 연속성을 증가시키고자 하였다. 최종적으로 미세 구조 개선 결과, 후열처리 된 Fe-1Ni-0.4B-0.8C 합금은 5.2 %의 높은 연신을 값을 나타냈다.

두 번째 주제로 두 개의 Fe-Mo-B 및 Fe-B-C 공정 상 형성을 통해 입 계 미세 구조를 수정하기 위해 Fe-B-C 합금 시스템에 몰리브덴 (Mo)이 도입되었다. 이를 위해 Fe-xMo-0.4B-0.8C (x=1.0~5.0 in wt %) 합금을 LPS로 제조하고 미세 구조 및 기계적 특성을 조사하였다. Mo 첨가로 매트릭스는 펄라이트 및 재 침전된 페라이트에서 펄라이트 (또는 베이나이트)로 변경되고, 입계는 연속 네트워크에서 MoFe(C,B)과 (Fe,Mo)<sub>3</sub>(C,B) 로 구성된 라멜라 구조로

변경되었다. 합금 내 미세 구조의 개선을 통해 합금의 경도, 인장 강도, 파단 연신율과 같은 기계적 특성이 크게 향상되었으며, 특히 Fe-5Mo-0.4B-0.8C 합금은 674 MPa의 높은 인장 강도와 4.92 %의 높은 연신율을 나타냈다.

세 번째 주제로 일반적인 소결법, 핫프레싱, 통전활성소결로 Fe-Ni 합금 ( $x=0.0\sim 5.0$  in wt %)을 제작하여 특히, 통전 활성 소결법의 전류의 효과에 집중하여 시편의 치밀화, 미세구조, 원소 분포도, 기계적 특성 등을 비교 조사 하였다. 니켈의 첨가는 일반적인 소결법과 통전활성법 모두에서 치밀화를 향상시키고 입자 성장을 억제하였으며, 특히 통전활성법으로 작은 결정 크기를 가지는 고밀도 Fe-Ni 합금을 제작하는데 성공하였다. 결과적으로 통전활성법으로 제작한 Fe-Ni 합금은 다른 소결 법으로 제작한 합금에 비해서 벌크 경도에서 큰 향상을 보였다. 원소 분포도 분석을 통해 니켈은 시편의 결정립계에 다수 분포하는 것을 관찰하였으며, 확산 실험을 통해 통전활성소결이 결정립계 확산을 향상함을 뒷받침 하였다. 위 결과로부터 통전활성소결 법의 압력과 가해주는 전류는 결정립계에서 Ni의 확산을 용이하게 하여 결과적으로 시편의 치밀화를 향상시키고 입 계 성장을 성공적으로 억제하였다.

**핵심어** : Liquid phase sintering, Field assisted sintering, Microstructure, Grain boundary, Modification, Mechanical properties

**학 번** : 2014-31057

## 감사의 글

막연한 꿈과 설렘을 안고 서울대학교 대학원에 들어와 석사를 졸업하고 이제 박사과정 졸업을 앞둔 시점에 와서 지난 날을 생각해보니 부족한 저에게 힘이 되어주고 많은 도움을 주신 분들께 감사의 말씀을 전하고 싶습니다.

가장 먼저 오랜 대학원 생활 동안 저를 지도해 주셨던 홍성현 교수님께 감사의 인사를 드리고 싶습니다. 학위과정 동안 부족하지만 아낌없이 조언을 해주시고, 사소한 결과에도 과정을 강조하셨던 교수님의 말씀은 제게 있어 큰 가르침이 되었습니다. 대학원 기간 동안 참교육자로서 생각하는 법과 통찰력을 길러주신 교수님께 다시 한번 감사의 말씀을 드립니다. 또한 바쁘신 와중에도 졸업논문심사뿐만 아니라 세세한 연구내용까지 조언 해주셨던 한홍남 교수님, 황농문 교수님, 그리고 먼 길 마다하지 않으시고 지도를 해주셨던 이혁모 교수님과 장재일 교수님께도 감사의 말씀을 드립니다. 그리고 학위과정동안 같이 생활하며 서로에게 좋은 조력자가 되어주기도 하고 친구도 되어 주었던 연구실 선, 후배님에게도 감사의 마음을 전하고 싶습니다.

마지막으로 제가 학업에 전념할 수 있게 물심양면으로 지원해주시고 지켜봐 주신 아버지와 어머님께 감사하다고 전하고 싶습니다. 지금까지 제가 올바르게 성장할 수 있도록 버팀목이 되어 주셔서 감사합니다. 앞으로 부모님께서 베풀어 주신 은혜 항상 생각하며 갚으며 살아가겠습니다.

니다. 그리고, 어렸을 때부터 응원을 해줬던 큰누나, 작은누나와 매번 조언을 아끼지 않으셨던 매형들에게도 감사의 말씀을 전합니다. 또한, 믿음을 주셨던 장모님, 장인 어른께도 감사드립니다. 그 누구보다도 10년이라는 긴 세월 동안 연애했으며 이제는 내 인생의 전부가 된 아내 희선. 항상 믿음으로 응원해주고 나를 완벽하게 만들어주는 당신에게 앞으로도 항상 사랑한다고 말해주고 싶습니다.

비록 한 분 한 분 지면을 통해 전하진 못했지만 그 동안 도와주신 모든 분들께 다시 한번 감사의 말씀을 전하며 대학원이라는 과정에서 벗어나 사회 생활에서도 더욱 발전하는 모습을 보여드릴 수 있도록 노력하겠습니다. 감사합니다.